Impact of Interfacial Molecular Conformation and Aggregation State on the Energetic Landscape and Performance in Organic Photovoltaics

Dissertation by

Guy Olivier Ngongang Ndjawa

In Partial Fulfillment of the Requirements

For the Degree of

Doctor of Philosophy

King Abdullah University of Science and Technology

Thuwal, Kingdom of Saudi Arabia

The dissertation of Guy Olivier Ngongang Ndjawa is approved by the examination committee.

Committee Chairperson: Professor Aram Amassian

Committee Members: Professor Frédéric Laquai,

Committee Members: Professor Omar F. Mohammed Abdelsaboor,

Committee Members: Professor Alberto Salleo

ABSTRACT

Impact of Interfacial Molecular Conformation and Aggregation State on the Energetic Landscape and Performance in Organic Photovoltaics

Guy Olivier Ngongang Ndjawa

In organic photovoltaics (OPVs) the key processes relevant to device operation such as exciton dissociation and free carriers recombination occur at the donor-acceptor (D-A) interface. OPV devices require the bulk heterojunction (BHJ) architecture to function efficiently. In these BHJs, D-A interfaces are arranged in three dimensions, which makes molecular arrangements at these interfaces ill defined and hard to characterize. In addition, molecular materials used in OPVs are inherently disordered and may exhibit variable degrees of structural order in the same BHJ. Yet, D-A molecular arrangements and structure are crucial because they shape the energy landscape and photovoltaic (PV) performance in OPVs. Studies that use well-defined model systems to look in details at the interfacial molecular structure in OPVs and link it to interfacial energy landscape and device operation are critically lacking. We have used in situ photoelectron spectroscopy and ex situ x-ray scattering to study D-A interfaces in tailored bilayers and BHJs based on small molecule donors. We show preferential miscibility at the D-A interface depending on molecular conformation in zinc phthalocyanine (ZnPc)/ C_{60} bilayers and we derive implications for exciton dissociation. Using sexithiophene (6T), a crystalline donor, we show that the energy landscape at the D-A interface varies markedly depending on the molecular composition of the BHJ. Both the ionization energies of sexithiophene and C_{60} shift by over $\sim$0.4 eV while the energy of the charge transfer state shifts by $\sim$0.5 eV depending on composition. Such shifts create a downward energy landscape that helps interfacial

excitons to overcome their binding energies. Finally, we demonstrate that when both disordered and ordered phases of D coexist at the interface, low-lying energy states form in ordered phases and significantly limit the Voc in devices. Overall our work underlines the importance of the aggregation and conformation states of molecular materials at and near the D-A interface in determining the operation and performance of OPV devices. This work shows that the role of D-A interfaces in complex BHJ devices can be unraveled through careful experimental design and by in depth characterization of planar heterojunction bilayer devices recreating model interfaces.

ACKNOWLEDGEMENTS

I would like to express my deep gratitude to Professor Aram Amassian, my research supervisor, for the thoughtful mentorship over several years. I acknowledge his guidance, encouragements and the trust he has put on my person in accepting me in his research team. I am ever grateful for the scientific training, which has turned me from a student into a researcher and most importantly his influence in shaping my ability to express myself more clearly in written English. I acknowledge Professor Ken Graham, who has guided my very first steps in research and who continues to guide me till date. His ability to teach with patience, tolerance for mistakes and continual encouragements has shaped me beyond research life. He is to me a true model and a person without whom my path into research will have certainly been very different. I would like to acknowledge my committee members for their time, their willingness to assess this work and most importantly to make the decision that will forever affect my future professional life. I wish to thank Professor McGehee, Professor Salleo and Professor Mark Thompson who have hosted me in their research groups and gave me unique opportunities to take advantage of their unique research facilities and to build valuable professional ties with their group members. I also wish to thank Professor Jean-Luc Brédas for his enlightening class on Organic Electronics and his counsels regarding future career. I thank my lab mates, especially Ahmed Mansour, for sharing this journey with me. They are the ones who knew my successes and failures first and who always responded with cheers or sympathy. Special thanks to Dr. Kui Zhao for the close research collaboration. I would also like to extend my thanks, to the KAUST Solar Center research staff with whom I have interacted with and the non-research staff who have assisted me at various occasions by offering critical help. Finally, I wish to thank my parents and my siblings for their support and encouragement throughout my studies.

TABLE OF CONTENTS

Glossary

bulk heterojunction	An organic solar cell in which the active layer consists of donor and acceptor materials intermixed at the nanoscale.
bilayer organic solar cell	Organic solar cell in which the active layer is composed of two thin layers whose interface form a two-dimensional heterojunction (Planar heterojunction).
charge recombination	Process in which under photoexcitation electronic charge moves in a way that reduces the difference in local charges between donor and acceptor sites.[1]
charge separation	Process in which under photoexcitation electronic charge moves in a way that increases the difference in local charges between donor and acceptor sites.[1]
charge-transfer (CT) complex	Ground-state complex that exhibits charge-transfer absorption.[1]
CT state	A state related to the ground state by a charge transfer transition.[1]
charge-transfer transition	Electronic transition in which a large fraction of an electronic charge is transferred from one region of a molecular entity (the electron donor) to another (the electron acceptor).[1]
D-A interface	D-A interface: Contact between two organic semiconductors (a donor(D) and an acceptor(A)) that differ in chemical composition and have different electron affinities. In organic solar cells this interface is capable of dissociating excitons.

delocalization	Spread of the the electron or hole wavefunction over many molecules as a consequence of the coherence in the arrangement of the molecules. Delocalization tends to stabilize holes and electrons.
electron affinity	Energy gained when an electron is added to a neutral molecule.
energy of the charge transfer state (E_{CT})	Energy required to make the charge transfer transition.[1]
energy landscape	Energy levels corresponding to all possible spatial conformations of a systems of interacting molecules.
excitons	Electrically neutral photoexcited species formed by an electrostatically bound electron-hole pair in semiconductors.
HOMO	Theoretical concept representing the wavefunction corresponding to the highest occupied molecular orbital of an isolated molecule.
intermolecular interactions	Weak electrostatic forces between neighboring molecules.
Ionization potential	Energy required to remove an electron from a neutral molecule.
LUMO	Theoretical concept representing the wavefunction corresponding to the lowest unoccupied molecular orbital of an isolated molecule.
molecular orientation	Relative position of the donor and the acceptor at the heterojunction or of each these moieties with respect to the substrate.
Organic Photovoltaic (OPV)	Solar cells based on semiconducting organic polymers or oligomers or on small organic molecules.

polarization energy	Energy gain through electrostatic interactions with the surroundings in the solid state and which stabilizes a charge in the solid in comparison to the gas phase. The polarization energy can be viewed as a measure of the ability of the solid state environment to stabilize charges.
photoinduced electron transfer	Electron transfer of a thermal electron transfer subsequent to photoexcitation of one of the reactants.[1]
Voc	Maximum voltage available from a solar cell measured at zero current.

LIST OF FIGURES

LIST OF TABLES

Chapter 1

Introduction

Photovoltaic (PV) conversion of solar energy is a viable and compelling route to overcoming the challenge of an ever-increasing world energy demand and the pressing need to curb the use of fossil fuels.[2] Conversion of solar energy using organic photovoltaics (OPVs) is of particular interest because OPVs offer in addition to clean energy production, a range of benefits related to scalability, cost, and extent of application which goes beyond conventional rooftop integration.[3–6] To convert solar energy into electricity, OPVs utilize carbon-based, π-conjugated, synthetic organic molecules. Films of these organic semiconductor materials are flexible, can be stretchable and can be processed at low temperature from ink-based routes or by vacuum deposition. It is this ease of processing combined with the potentially low energy payback time that confer an advantage to OPVs.[7, 8] The fundamental need for high efficiencies and the competition with other solar technologies[9] fuels the need for even more efficient and affordable solar cells. To date, substantial progress has been made towards that goal, resulting in OPV devices with efficiencies greater than 13%.[10–15] These gains were secured as a result of better understanding of device physics,[16–22] improved materials design,[10, 23–25] new processing techniques,[10, 24, 26] and by the development of novel device architectures that are more tolerant to variable processing approaches.[12, 26, 27]

OPV devices rely on the complementary action of at least two organic semiconductors to harvest sunlight into electricity.[28, 29] The need for more than one material for an OPV device to function effectively is to be contrasted with the situation in inorganic

semiconductors for which there is no fundamental requirement for the use of more than one material for light harvesting.[9] The reason for this distinction comes from the intrinsic difference in the nature of photoexcited states that are generated upon light absorption in organic and inorganic semiconductors.[18] In these materials, photoexcited states are neutral and bound species called excitons (or Frenkel excitons), meaning that the hole and the electron generated upon light absorption do not readily separate, but instead are held together through Coulomb interactions with a binding energy in the range of 0.3 - 1 eV.[30] In inorganic semiconductors, such as silicon or gallium arsenide to name just two, photoexcited species are effectively unbound species (Wannier excitons), with a minute binding energy of ∼15 meV,[31] meaning that the hole and the electron barely interact because of the effective screening by the medium. This crucial difference in the way organic and inorganic semiconductors accommodate excited state species is readily explained by the low relative dielectric constant of organic semiconductors, typically in the range of 2-4[32] for organics compared to ∼11.7 for silicon.[33]

The optoelectronic properties of organic semiconductors, namely π-conjugated systems, follow from the delocalized nature of the π-electron system. This also has a consequence that the photoexcited states are strongly coupled to the geometry of the organic molecule (strong electron-phonon coupling[34]) and further contribute to maintaining the electron and the hole as single species.

If the electron and the hole remain bound as excitons, then no current can be generated by the solar cell. The strategy to overcome the high exciton binding energy and dissociate excitons into free electrons and free holes is to utilize a second semiconductor (the acceptor or A) whose energy levels are offset with respect to that of the material in which excitons are generated dominantly (the donor or D) such that there is a driving force for the electron to undergo charge transfer from D to A.[35–37] The same process is also possible with excitons generated in the acceptor, whereby

the energy level offset promotes hole charge transfer from A to D. The heterojunction formed between D and A materials plays a crucial role in mediating the photovoltaic response of solar cells as it is at the nexus of charge separation and recombination. Although the heterojunction conceptually serves the purpose of converting excitons into free carriers, the relatively short lifetime of excitons means they cannot diffuse over a long distance.[38] Thus the D-A interface needs to reside within the range of the exciton diffusion length to avoid wasting a significant fraction of the excitons generated through light absorption. To overcome the competing limitations posed by the low exciton diffusion length and the need for the absorber layer thickness to be far greater than the exciton diffusion length, the bulk heterojunction (BHJ) concept was adopted. In a BHJ, the D and A components are blended and form an interpenetrating network in which D and A phases are separated into domains with dimensions on the order of 10 nm.[39, 40]

The energetics of the D and A materials at the interface govern the separation and recombination mechanisms in organic solar cells.[41, 42] Although the electronic properties of isolated D and A molecules can constitute the basis for a rough prediction of the D-A interfacial electronic structure, they remain crude approximations and can often be erroneous and meaningless when the D and A molecules are in the solid state. In addition, as molecules within the D and A regions come into contact at the so-called "D-A" interface, new energy states, known as charge transfer (CT) states, are formed. The CT state associated with a simple bimolecular D-A complex is characterized by electronic transitions in which a large fraction of an electronic charge is transferred from the D to A.[43, 44] The charge transfer state energy (E_{CT}), or the energy required to make the charge transfer transition, has been found to determine the maximum achievable open circuit voltage (Voc) of organic solar cells,[45, 46] meaning that CT states in addition to influencing charge generation also influence the power output of these devices via its Voc.

The CT state energy is closely related to the ionization potential of D and the electron affinity of A, both materials characteristics which are heavily dependent on their aggregation state and local conjugation effects.[18, 47] The energetics of D and A materials are also affected by their degree of order, which can vary within the same material, making them quite heterogeneous and complex especially in the context of a three-dimensional BHJ.[48, 49] These factors inevitably translate into a D-A interface with varying degrees of order and molecular conformation which is likely to lead to a distribution of energy states. The presence of many interfacial states makes interfacial energetics hard to characterize. Moreover, the interfacial states that have the lowest energy will drive the chemical potential of the overall ensemble of states and Voc down.[20, 21] To make matters even more complex, D and A molecules interact strongly and can spontaneously intermix,[50–52] meaning that the interfacial molecular arrangement so crucial to solar cell operation may not be a simple extension of the bulk structures of D and A domains.

Although material's structure crucially determines PV performance, studies that use well-defined model systems to look in details at the interfacial molecular structure in OPVs and link it to interfacial energy landscape and device operation are lacking. Current studies look at the BHJs as an ensemble, because they are difficult to untangle. A number of highly efficiency OPVs are based on polymers which are hard to characterize in detail. For instance, a number of investigations using spectroscopy analysis to probe energy levels in polymers face difficulties to precisely correlate spectral features to well-defined aspects of the polymers' microstructure. As a result, the precise impact of the local variations in material's structure in the BHJ is often overlooked although these variations are expected to affect device operation significantly. Similarly a number of studies attempt to address the role of molecular conformation and structural order at the D-A interface in OPVs, but they often rely on simplifying assumptions on the interfacial molecular structure extending from that of the bulk

and a uniform energy landscape at the interface.

In this thesis we will develop an approach which accounts for the complex microstructure in OPVs, including molecular conformation, aggregation, interfacial mixing, and coexistence of ordered and disordered phases, with the aim to establish the link between solar cell behavior and the microstructure and energetics at D-A interfaces.

We carefully contrive model planar and bulk heterojunctions that are simple, structurally well-defined and with representative interfaces so that they may help untangle the complex ensemble behavior of real BHJs. We do this by tuning the extent of molecular interactions, the interfacial molecular conformations, the extent of order in D and A and the composition in the mixed phase.

We select a subset of widely investigated small molecules based on their degree of crystallinity, their ability to be crystallized or templated to a given molecular packing/molecular orientation and their ability to mix with the fullerene-C_{60} acceptor. These materials are also vacuum-processable which makes them suitable for in-situ photoelectron spectroscopy studies in ultra high vacuum (UHV).

The outline of this thesis is as follows: In Chapter 2 we present a review of the role of structural order in OPVs. We explore in detail the impact of the microstructure of the organic semiconductors on the interfacial energy landscape. We also discuss the current understanding of how the interfacial energy landscape influences the photovoltaic performance in OPVs.

In Chapter 3 we explain the general methodology of this work. We mainly discuss how donor-acceptor interfaces were characterized in both thin-films and devices and how a range of molecular structures at interfaces were emulated using tailored bilayers and BHJs.

In Chapter 4 we investigate the impact of donor molecular packing orientation on interfacial mixing and on charge separation at the D-A interface. We probe the role of molecular conformation on interfacial order, charge separation and recombination.

The use of bilayer thin films, i.e. with just one donor-acceptor interface allows us to successfully decouple interfacial effects from bulk effects and explain the performance of solar cells in terms of degree of molecular mixing at the D-A interface.

In Chapter 5 we discuss the role of molecular conformation, the degree of order and composition in D and A and how they determine the energy of the frontier orbitals and the charge transfer state. We conduct detailed measurements of energy landscapes in model organic semiconductor systems and determine how these energy landscapes vary based on the degree of structural order and the molecular composition. We link large shifts in ionization and charge-transfer state energies of molecules in mixed phases to the ability of charges to overcome the interfacial binding energy and separate efficiently.

In Chapter 6 we discuss how coexisting phases in the donor differing in terms of degree of long-range order dictate the energies and the density of states of interfacial charge transfer states and the open circuit voltage. We do so by tuning the microstructure of donors, their texture and their ability to mix with C_{60}. We use both solar cell devices and modeling to detect and link the presence of the many CT states to the Voc in actual devices.

In Chapter 7 we conclude the entire work with a summary followed by perspectives for future work.

Chapter 2

Impact of Molecular Structure on the Interfacial Energy Landscape and the Open Circuit Voltage of Organic Solar Cells: A Review

In this chapter, we review the current understanding of structural factors that affect the energy landscape in organic solar cells. We start by introducing organic solar cells and the important figures - of - merit used to describe their photovoltaic performance. We then explore the microstructure of organic semiconductors and its implications in terms of the interfacial energy landscape. We finally discuss what role the interfacial energy landscape plays in determining the voltage output in organic solar cells and their photovoltaic performance in general.

2.1 Organic solar cells

2.1.1 What is an organic solar cell?

In general, a solar cell, or photovoltaic cell, is a semiconductor-based device that absorbs solar radiation and converts it directly into electricity. Organic solar cells utilize carbon-based synthetic organic semiconductors to convert solar energy into electrical energy.[36, 53] In these cells, two organic semiconductors are required for an efficient photovoltaic conversion. The organic semiconductors are essentially π-conjugated materials than can be either small molecules, oligomers or polymers. Because organic materials can be processed from solution or by low temperature vacuum sublimation, they offer a unique advantage in terms of low cost and large area fabrication. An

important trait of organic molecules is that they absorb visible light very efficiently and only a small amount of materials is needed to make solar cells that are optically thick (few hundreds of nanometres layers typically). In addition they are flexible and can be made transparent, which makes them suitable for integration into buildings or wearable devices.

2.1.2 The excitonic nature of organic solar cells

Organic solar cells distinguish themselves fundamentally from their inorganic counterparts. They are based on low dielectric constant organic materials. This implies that upon photoexcitation, the generated electron-holes pair, defined as excitons, are strongly bound and cannot be dissociated by the available thermal energy at room temperature (25 meV).[54] This limitation makes it necessary to use a second material whose role is to assist exciton dissociation. Typically, one component of the active layer absorbs most of the solar radiation and is often referred to as the donor while the other component provides the driving force splitting the excitons into free carriers and is referred to as the acceptor. When the donor and the acceptor are combined to produce electricity, they form the active layer. An organic solar cell can have one active layer (single-junction) or many active layers (multi-junction) with the aim of maximizing the output of the solar cell. In this work however, we only discuss single-junction organic solar cells.

2.1.3 Architectures of single-junction organic solar cells

2.1.3.1 Bilayer organic solar cells

The bilayer structure (also called a planar donor-acceptor heterojunction) was first developed by the Tang group[36] and constitute the simplest of all architectures used in organic solar cells. In bilayer solar cells the contact between the donor and acceptor components is limited to the single interface (Figure 2.1a). An exciton generated in

the bulk of the donor material thus has to reach that interface to dissociate into free charges, otherwise it recombines and the excitation is lost. Because of the short exciton diffusion length of organic donor materials, most excitons are lost through direct recombination.[55] For this reason, bilayer solar cells are usually made with very thin layers. Although thin layers enable the collection of most excitons, part of the incoming photons is not absorbed. An architecture that allows for thick cells (100 - 300 nm) and a large interfacial area to enable an efficient light absorption and which facilitates exciton collection and splitting is thus required. Such an architecture is discussed in the next section.

2.1.3.2 Bulk heterojunction solar cells

To circumvent the issue of low exciton diffusion length, the bulk heterojunction (BHJ) structure is employed.[53] In a BHJ, a bicontinuous nanoscale network with donor/acceptor (D/A) interfaces throughout the bulk is realized by blending a donor and an acceptor from solution or during vacuum deposition (Figure 2.1b).[56] In addition to the donor and the acceptor domains being within the exciton diffusion length, the three dimensional nature of the BHJ means a large interfacial area which further improves the collection of excitons. Most modern organic solar cells are fabricated in the BHJ architecture and most of these cells comprise one donor and one acceptor component. However, BHJ structures with more than one donor are starting to be explored.[21] Despite the advantages of the BHJ, the bilayer architecture remains useful for research as it is typically used to test concepts about device physics without the interferences that may arise from the architecture itself. In this work, very often we will be using the bilayer architecture for this reason.

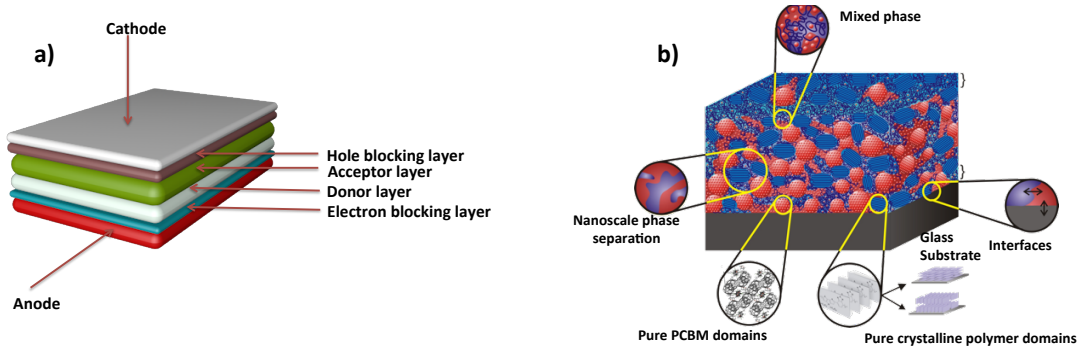

Figure 2.1: Sketches of common architectures of organic solar cells. (a) Bilayer structure containing two organic layers (the donor and the acceptor) sandwiched between two selective layers (the hole and electron blocking layers) and the conductive electrodes (cathode and anode). (b) Bulk heterojunction (BHJ) structure exhibiting a nanoscale blend of donor and acceptor materials. The nanoscale blend may feature phases of the donor and acceptor with different degree of purity and molecular arrangements. The BHJ schematic was adapted from the work of the McGehee and the Toney groups at Stanford.

2.1.4 Possible geometries of the solar cell stack

With reference to the direction of flow of electrons with respect to the substrate, two geometries of the solar cell stack can be distinguished: a normal and an inverted geometry. In normal geometry, electrons are collected by the top electrode while the holes are collected by the transparent bottom electrode. In the inverted geometry, the hole blocking layer and electron blocking layer are switched around. In this situation, the electrons are now collected by the bottom electrode and the holes by the top electrode. The inverted structure makes it unnecessary to use acidic blocking layers such as PEDOT:PSS.[1] Issues related to vertical phase separation, attributed to interactions with the certain blocking layers are also eliminated in the inverted geometry.[57] It is important to note that the concept of the stack's geometry applies only to BHJs and not to bilayers. in this work we have made bilayer and BHJ devices in the normal configuration only.

[1]PEDOT:PSS or poly(3,4-ethylenedioxythiophene)-poly(styrene sulfonate) is a conductive polymer mixture often used as an electron blocking layer in organic solar cells

2.1.5 Principal figures-of-merit of a solar cell

2.1.5.1 Jsc, Voc, FF and PCE

The photovoltaic performance of a solar cell can be measured by means of simple electrical characterization whereby the current density generated under illumination by the cell is recorded as a function of the voltage. The figures-of-merit of the solar cell can be extracted from this current-voltage characteristic (J-V curve). Three quantities, short-circuit current (Jsc), fill factor (FF), and open-circuit voltage (Voc) describe different aspects of the performance of the photovoltaic action (Figure 2.2). The power conversion efficiency (PCE), the ratio of the output power (P_{out}) to incident power (P_{in}) is expressed in terms of the parameters extracted from the J-V curve using Equation 2.7 and 2.2 .

$$\mathrm{PCE}(\%) = \mathrm{P_{out}}/\mathrm{P_{in}} = \frac{\mathrm{Jsc} \times \mathrm{FF} \times \mathrm{Voc}}{100} \tag{2.1}$$

Where,

$$\mathrm{FF}(\%) = \frac{\mathrm{J_M} \times \mathrm{V_M}}{\mathrm{Jsc} \times \mathrm{Voc}} \times 100 \tag{2.2}$$

With J_M and V_M being the current and the voltage at the maximum power point (MPP) respectively. MPP is the point in the current-voltage curve at which the output power reaches its maximum. Jsc is the current density generated by the device at short-circuit and when no bias is applied to the device. At Jsc, no power is generated since the carriers have zero electrochemical potential (i.e. quasi Fermi levels for electrons and holes perfectly aligned) and thus carriers bear no electrical energy. The short-circuit current depends strongly on the amount of light absorbed in the active layer of the device i.e. of the absorption coefficient of the absorber within the active layer. The design of conjugated materials that absorb sunlight efficiently

and thus maximize Jsc is discussed in depth here [58, 59].

FF describes the ability of the solar cell to generate current under conditions close to open circuit voltage. Pictorially, it is a measure of the squareness of the J-V curve in the power quadrant (Figure 2.2). In an efficient solar cell, the magnitude of the current that is generated by the cell near Voc remains close to the magnitude of the current it generates under short-circuit condition (no load). Strategies to increase FF without compromising other device parameters remain an important challenge in the organic photovoltaic (Organic Photovoltaic (OPV)) field. Recently, researchers have made major steps forward in associating a physical meaning to FF with the help of newly constructed models that describe FF for a wide range of OPV systems.[16] Voc is the voltage at which no current flows in the cell. Thus, at Voc, all the carriers recombined and no power is generated. Voc is a critical parameter in OPVs because its improvement is expected to boost PV performance significantly. In section 2.4 we discussed Voc in organic solar cells in more depth.

2.1.5.2 Quantum efficiencies

The quantum efficiency of a solar cell is a unitless measure of the amount of current that the cell produces per unit photon at each light wavelength. Because not all incident photons impinging the device are absorbed, it is important to differentiate between the number of electrons generated per unit photon absorbed in the active layer (the internal quantum efficiency-IQE), Equation 2.3, and the number of electrons generated for each incident photon (the external quantum efficiency measurement-EQE), Equation 2.4 . For a typical solar cell, the maximum value for the IQE or the EQE is 100%. However for devices exhibiting multiple exciton generation, i.e. in which one photon can generate more than one exciton, the quantum efficiencies may surpass 100%.[60]

$$\text{IQE} = \frac{\text{electrons generated}}{\text{absorbed photons}} \tag{2.3}$$

$$\text{EQE} = \frac{\text{electrons generated}}{\text{incoming photons}} \tag{2.4}$$

Thus, while the IQE relates directly to the electronic processes in the cell, the EQE depends strongly on the device's optical properties.[61] Taken together, IQE and EQE inform significantly on the ability of the device to absorb sunlight effectively and convert it to electricity.

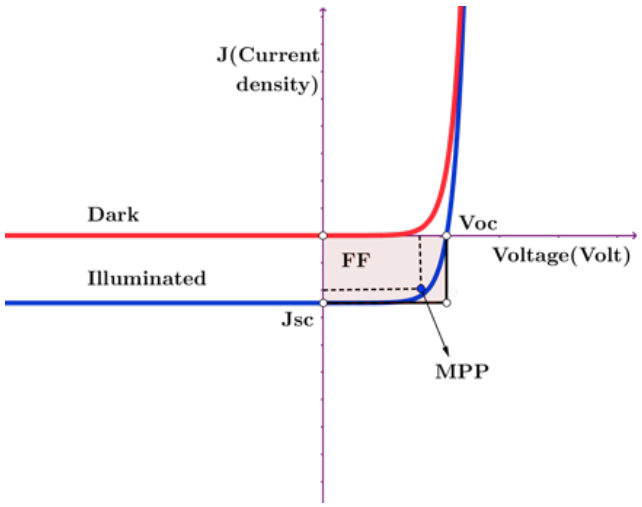

Figure 2.2: Typical currentvoltage characteristic of an organic solar cell in the dark and under illumination. FF, Jsc and Voc represent key device parameters from which the cell efficiency can be derived. MPP designates the maximum power point, which can also be related to device efficiency.

2.1.6 Electronic state diagram of organic solar cells

Photovoltaic processes in organic solar cells are commonly described with the aid of electronic state diagrams, which depict single and quasi-particles states and energies for the donor and acceptor materials. These diagrams are very useful because they capture the essential aspects of the photovoltaic action and allow one to break the otherwise very complex process into simple steps. Here we utilize a common scheme developed by Brédas and coworkers.[18] We first discuss the five important processes that synergistically take part in the photovoltaic action which are illustrated in a simplistic diagram shown in Figure 2.3. The incoming photons are absorbed in the bulk of the organic semiconductor, producing excitons that can diffuse over several nanometers during their lifetime.[38, 62] In the pure material, due to their bound nature, the ultimate fate of excitons is geminate charge recombination of the electron and hole. To dissociate the bound electron and hole, the common strategy is to exploit the difference in electronegativities of two materials that are chosen such that either their electron affinities or ionization potentials are misaligned. The material with the lowest electron affinity is called donor (D) and that with highest electron affinity is called acceptor (A). Efficient electron transfer in D-A systems exhibiting an offset in electron affinities of only 0.14 eV [36, 39, 40, 63] and as low as 50 meV have been reported.[64] The offset creates the driving force for the electron to undergo transfer from D to A. Research shows that after the electron transfer has occured, the electron and the hole remain in an excitonic state,[65] i.e. that they still interact coulombically, making it necessary to provide a further driving force to split the intermediate species (excitons in the CT state) into free carriers (mobile electron and hole). Finally, the free carriers should selectively be provided pathways to electrodes where they become available to produce work to an external circuit.

While the basic operation of an organic solar cell can be illustrated as in Figure 2.3 where states are represented by just one-electron wavefunctions (labelled here as

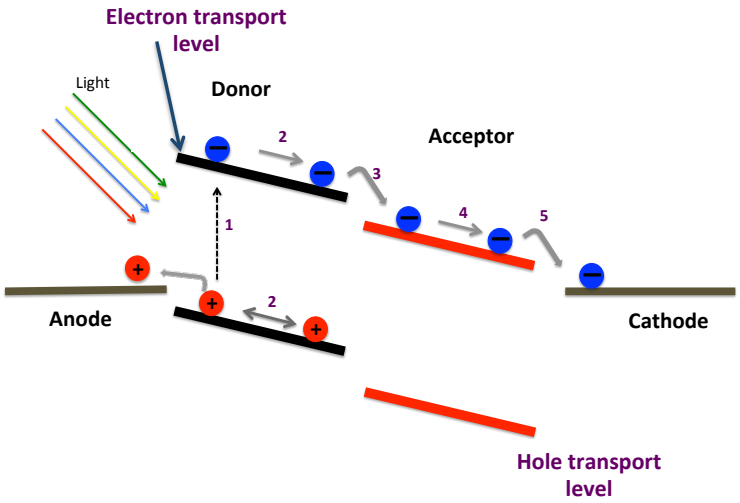

Figure 2.3: Simplified schematic showing the key working steps of an organic solar cell. Unlike in inorganic semiconductors, in which light absorption instantaneously results in the generation of free carriers (mobile electrons and holes), in organic semiconductors, due to their very low dielectric constant, photon absorption (step 1) rather results in the formation of a bound exciton, a neutral electron-hole pair in which the photo-generated electron continues to feel the coulombic attraction of the bound hole. For the solar cell to generate current, the exciton needs to diffuse (step 2) to an interface formed between the donor and the acceptor where it undergoes dissociation (step 3) and generate free carriers that subsequently drift (step 4) towards the respective electrodes where they couple to an external circuit (step 5).

transport levels but often referred to as HOMO and LUMO), photophysical processes in an organic solar cell must be described in terms of many electron wavefunctions (Figure 2.4). The absorption of photons in the bulk of the semiconductor leads to the formation of singlet excitons (singlets) in the S_1 state . These excitons diffuse to a D-A interface, undergo fission into triplet states T_1 or annihilate and return to the ground state S_0. A BHJ architecture, by design, maximizes the chances for most excitons to meet a D-A interface where electrons can undergo an ultrafast transfer (10 - 100 fs timescale) into interfacial charge transfer states.[29, 66] The efficiency of the electron transfer process (determined by k_{CT}), in the context of the Marcus theory,[67] is a function of the extent of the donor and acceptor wave-functions overlap, the energetic offset between the donor, the density of charge transfer states

and the reorganization energy associated with the electron transfer process.[68] After population of the CT manifold resulting into the formation of interfacial excitons, competition exists between several dissociation and recombination pathways. Since the transferred electron remains bound to the hole on the donor,[65, 69, 70] irrespective of which pathway actually dominates the CT separation, the remaining coulombic barrier needs to be overcome. Direct dissociation leading to long-range charge separation via vibrationally excited CT states (CT^*), often referred to as "hot" CT states, into CS^* states have been postulated, [71–73] however, it is still very much debated whether this pathway leads to efficient generation of free carriers. Through this route, the excess thermal energy is supposedly used to overcome the interfacial coulomb well. Alternatively, the "hot" CT exciton first vibrationally relaxes to the lowest electronic state in the CT manifold (CT_1) on an ultra-fast time scale ($\sim$1ps timescale) [74, 75] before it dissociates into CS. Whether direct dissociation from CT^* or relaxation into CT_1 dominates depends on which of the rates k^*_{CS} and k_{CS} is the highest. There is increasing evidence that dissociation through the relaxed CT state CT_1 is the dominant pathway and we adhere to this view throughout the remaining of this work.[74, 76–78]

When the electron is in the vibrationally relaxed CT state, CT_3 can be equally populated by spin inversion. The efficiency of this process is expected to be very high, owing to the relatively large separation between the hole and the electron in the CT states, CT_1 and CT_3 are very close energetically with an energy separation of only about 5 meV.[79] When the CT exciton is fully vibrationally relaxed, there still exists the possibility for the electron to transfer back to T_1 if T_1 falls energetically below CT_1/CT_3.[80, 81] As in the case of organic light emitting diodes, high charge concentrations in organic solar cells allow for large number of encounters between free holes and electrons leading to the formation of CT_1 and CT_3 excitons in a ratio that obeys spin statistics. This would imply that electron transfer from CT_3 to T_1 would

constitute the dominant recombination pathways even in state-of-the OPVs systems in which T_1 often falls below CT_3.

The direct, although weak dipole moment, between S_0 and CT_1, additionally allows the exciton to relax to the ground state. Formation of free carriers through CS would proceed at the rate k_{CS}, which depends on the CT state lifetime, the presence of delocalized CT states, a downhill energy cascade or entropic forces.[20] The energy of the final CS state, corresponding to a completely unbound electron-hole pair, is defined by the sum of the Ionization potential (IP) of the donor and electron affinity (EA) of the acceptor, E_{CS} =IP (D) + EA (A). E_{CS} also corresponds to the maximum achievable open-circuit voltage.

2.1.7 The role of polarization energies in organic semiconductors

The energy of the charge separated states depends heavily on the molecular environment present. While in the gas phase, molecules are essentially surrounded by vacuum, in the condensed phase, each molecule is surrounded by other molecules. The presence of a charge in an organic molecule in the solid state creates an electric field that the surrounding molecules experience. These surrounding molecules therefore polarize and form dipoles or quadrupoles that in turn interacts with the charged molecule in such a way that results in an energy gain. By the same mechanism, the electronic density on a neutral molecule, through dipole-dipole interaction, or induced-dipole induced-dipole interaction, stabilizes both the ground state and the excited states of the molecule.

The energy required to ionize a molecule either in the gas phase or the solid state is thus dependent on how well the charge is stabilized after the ionization process. The polarization energy is the quantity that accounts for the difference between the ionization potential or the electron affinity in the solid state and the gas phase (Equation

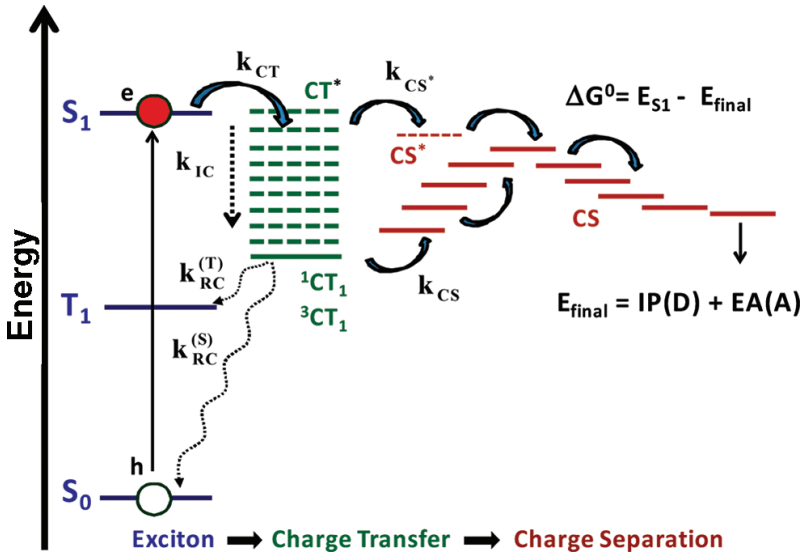

Figure 2.4: Electronic states diagram of an organic solar cell.[18] The set of blue-colored lines illustrates the states involved in the photon absorption and exciton generation processes and the set of red-colored lines illustrate the states occupied by free carriers and through which charge transport occurs. The green-colored lines are interfacial charge transfer states where excitons are split and generation of free carriers is initiated. The rate constant for electron transfer from S_1 to the CT manifold is denoted k_{CT} and the rate of thermalization of vibrationally excited CT states is denoted k_{IC}. Relaxation to T_1 or to the ground state S_0, from the relaxed CT states (CT_1 or CT_3) occurs at rates $k_{RC}^{(T)}$ and $k_{RC}^{(S)}$ respectively. The CT exciton can split to form charge separated states (CS* and CS) at rate k_{CS}^{*} or k_{CS} respectively. The energy the free carriers at the end of the separation process is $E_{final} = IP(D)+EA(A)$ and the change in the free energy for the entire process (photon absorption to free carriers formation) is $\Delta G^0 = E_{S1} - E_{final}$.

2.5 and 2.6).

$$P_+ = IE_{solid\ state} - IE_{gas\ phase} \tag{2.5}$$

$$P_- = EA_{solid\ state} - EA_{gas\ phase} \tag{2.6}$$

P_+ and P_- represent the energy difference between the IE (ionization energy) and the EA (electron affinity). Often, there exists an asymmetry between the values of P_+

and P_-, the common trend being that $P_+ > P_-$ for most materials.[82] Polarization is important in organic solar cells because charge separation is a balance between polarization and coulombic effect. Polarization tends to localize the hole in the donor and the electron on the acceptor while coulombic forces tend to drive the electron and the hole towards each other. Molecular structure has a significant influence on the polarization energy. This explains why polarization often decreases with the extent of conjugation. For instance, polarization decreases for more extended acenes. Packing also plays a big role. A striking example is that of pentacene and TIPS-pentacene [2]. While the electrostatic of pentance and TIPS-pentacene do not differ significantly (quadrupoles distribution are similar) the difference in polorarization energies is very significant. The reason for this significant discrepancy originates from the packing. Pentacene packs in a so-called herringbone structure while TIPS-pentacene packs in the so-called brickwork structure. In the herringbone structure, the quadrupole interactions are stabilizing while in the brickwork structure they are destabilizing. As a result, there occurs a large reduction in the polarization energy of TIPS-pentacene ($P_+ = 0.59$ eV and $P_- = 0.69$ eV) compared to pentacene ($P_+ = 1.02$ eV and $P_- = 0.79$ eV).[83] In this work polarization energies are determined from measured solid state ionization potentials and reported gas phase ionization potentials.

2.2 Energy landscape in organic solar cells

The energy landscape is used to refer to the energy states present in the active layer of the solar cell. These energy states are the reflection of materials compositions and microstructures. We wish to discuss the role of the latter on the energy landscape in organic solar cells.

[2]TIPS-pentacene:6,13-Bis(triisopropylsilylethynyl)pentacene

2.2.1 The role of the microstructure

The operation and performance of organic solar cells depends largely on the choice of the π-conjugated semiconducting material systems that compose the photoactive layer, their chemical structure and the way these molecules organize at various length scales in the solid state thin film. The chemical structure, together with the ordering and aggregation state of these semiconducting materials by and large determine the energetic landscape within the photoactive blend. This structural dependence is more pronounced in organic solar cells because the same active layer is expected to serve as the medium for all the processes that compose the photovoltaic action. In specific, the active layer is responsible for efficiently absorbing sunlight and then allowing the resulting photoexcited species (excitons) to diffuse to an organic heterojunction where they may dissociate into free carriers; these free carriers should subsequently be provided continuous and energetically favorable pathways for them to flow away from the heterojunction and be extracted at the appropriate electrodes. This multifunctional role places stringent requirements on the electronic and structural properties of organic semiconductors, as they must absorb, split excitons and extract charges. For instance, the amount of light that is absorbed, both exciton transport and charge separation are strongly dependent on the molecular structure of the absorbing material, its extent of order and the molecular orientation it adopts with respect to the substrate plane. Excitons that carry the photovoltaic energy are unfortunately neutral short lived species (lifetime in the order of the few ns).[84] Thus, they diffuse randomly in the active layer and during their lifetime may split or eventually recombine. The distance excitons can travel before they recombine depends on their diffusion coefficient and lifetime which both strongly depend on the electronic and structural properties of the medium in which they are generated.[62, 84–86] Because in addition, excitons in organic materials constitute pairs of coulombically bound charges (Frenkel-type excitons), [62] a driving force is necessary to overcome this

coulombic potential barrier. Such a driving force is available at an organic-organic interface where an electron accepting material with the right energy level offset favors electron transfer and the formation of an interfacial exciton over other processes that preserve or annihilate the excitons. The rate of electron transfer and dissociation of the bound interfacial excitons are dependent not only on fundamental electronic properties of the isolated electron donor and the electron acceptor materials but also on the degree of intermolecular interactions at that interface. These interactions have been found to be mostly electrostatic in nature and thus strongly dependent on the interfacial molecular conformation and local charge distribution. In addition, the spatial extent of the interfacial exciton is dependent on the extent of donor and acceptor interfacial order. Most organic semiconductors only exhibit partial order implying that the degree of order varies with the length scale under consideration. The photophysical response of these materials in their pure forms and when they are mixed to form composites is expected to reflect the inhomogeneity and the complexity that are inherent to their solid-state structures. For instance one or several monomers of a polymer chain may be involved in the absorption of a single photon depending on the conjugation length within the polymer backbone.[87, 88] Similarly, a single absorption event can take place across several interacting chromophores corresponding to different polymer segments.[62, 89, 90] It, therefore, becomes important not only to control the microstructure of the active layer, but also to be able to use appropriate tools to interrogate the film structure a posteriori. Because organic solar cells are not made from one active material, but of a composite of two materials often in the form of bicontinuous network, the structural complexity is even more amplified. A significant body of studies indicates that the voltage output of the organic solar cell depends sensitively on the materials structure right at the heterojunction. Understanding how interfacial structural details affect the photovoltaic performance is of particular interest.

Ultimately the solar characteristics (Jsc, FF, and Voc) are all dependent on the microstructure of the active layer. Much effort in the field of organic solar cells goes into establishing a relationship between device characteristics and the active layer microstructure in OPVs. We now discuss the role of structural order in organic semiconductors commonly used in OPVs. The highly complex morphology of the active layer is often classified in terms of domain size, domain purity and preferential orientation at the donor acceptor interface.[91, 92] Our discussion mainly includes the role of the degree of crystallinity of the donor and the acceptor, their miscibility, the orientation of the crystalline domains with respect to the substrate plane and the relative conformations at the donor acceptor interface.

2.2.2 Structural order in the bulk for polymers, oligomers, and small molecules

Semiconductors commonly used for organic solar cells are conjugated polymers, oligomers, and small molecules.[93–99] The ability of these materials to organize at a molecular level depends on their chemical structure and the process by which they are brought into their condensed form. Polymers and oligomers are large molecules and typically functionalized to increase their solubility in organic solvents. As a result, they exhibit a complex molecular structure which renders the crystallization process difficult. They tend to simultaneously form amorphous and crystalline domains during film formation. Small-molecules are smaller in size and molecular weight and can be solution-processed and/or vacuum- processed.[93, 96, 100, 101] However, as in the case of polymers and oligomers, they often condensed into thin films using fast deposition techniques, which may also favor formation of films with a low degree of order.[102, 103]

2.2.2.1 Polymers

Because polymers are made of extended molecular chains with many degrees of freedom they assume several conformations, which subsequently influence how they pack in films, when cast from solution or solidify from a melt. When aggregation is possible, film casting will result in the simultaneous formation of both amorphous and crystalline phases.[104] The ability for polymer chains to pack and the packing mode both depend on the polymer molecular structure, molecular weight, and processing conditions.[104–108] For instance, aggregation may originate from precursors formed in the liquid state. The degree of aggregation in solution depends on parameters such as choice of solvent, polymer concentration, molecular weight and conjugation length. These solution-formed aggregates are critical as they serve as nucleation sites during condensation to the solid state. Now we consider bulk heterojunctions in which the more conventional spherical symmetric fullerene or one of its soluble derivatives, such as $PC_{61}BM$[3] is used we focus on the donor molecular conformation. The architecture and possible conformations of the donor thus completely determines the range of possible interfacial molecular arrangements at the atomistic scale. Conjugated portions of polymers or small molecules are often planar. Contacts with fullerene can, therefore, happen with the π-conjugated backbone directly exposed to fullerene (face-on), one of the neat or functionalized edges in contact with the fullerene (edge-on or side-on). In addition, preferential access to specific functional segments can be favored through steric control.[109] Bao et al, show using highly volatile solvent and substrate temperature control, that the orientation of stacking planes in the much-studied thiophene based polymer RR(regio random)-P3HT[4] can be directed. Warm CH_2Cl_2 solution was directly cast on room temperature substrate, which served to seed PH3T crystallites growth with stacking planes oriented face-on. The more slow

[3] $PC_{61}BM$(Fullerene derivative):Phenyl-C_{61}-butyric acid methyl ester
[4] P3HT:Poly(3-hexylthiophene-2,5-diyl)

drop-casting process resulted in polymer chains adopting an edge-on orientation.[110] The degree of internal order on the polymer backbone was also to influence polymer packing. For instance, poly(3-hexylthiophene) (P3HT) crystalline domains assume two different orientations with respect to the substrate depending on the degree of regioregularity and its molecular weight. It has been found that highly regioregular (96% rr) and low molecular weight P3HT the polymer stacks with the conjugated backbone orthogonal to the plane of the substrate. On the contrast, when the polymer is only 81% regioregular, the crystallites (lamellae) orient in such a way that the conjugated backbone lies in the plane of the substrate.[111]

Through molecular chemistry, exchanging hydrogen atoms for fluorine atoms on the polymer backbone, researchers have also achieved interfacial molecular orientation control in a range of polymer/fullerene blends and demonstrated improved performance when a more face-on conformation is realized at the donor-acceptor interface.[112, 113] More recently, side-chain engineering, exquisite control of polymer aggregation has been achieved in high performing PffBT4T-2OD:$PC_{61}PM$ systems[5].[68,69] The outstanding coherence length of the polymer (four times larger than that of the equally high performing PTB7:$PC_{61}BM$)[6] and preferential face-on polymer backbone orientation were found to be critical in achieving high device performance. The appropriate choice of the side-chains length and its location on the polymer backbone enabled temperature-activated polymer aggregation in solution allowing a robust blend morphology which was found to be highly tolerant of the choice of fullerene. The research demonstrates how polymer structural control is crucial in achieving very high performing organic solar cells. Similarly, using atomic substitution, researchers were able to modify molecular orientation relative to the donor/acceptor heterojunction in devices featuring the series of electron-donating polymers; PNDT-

[5]PffBT4T-2OD:Poly[(5,6-difluoro-2,1,3-benzothiadiazol-4,7-diyl)-alt-(3,3-di(2-octyldodecyl)-2,2;5,2;5,2-quaterthiophen-5,5-diyl)]

[6]PTB7:Poly(4,8-bis[(2-ethylhexyl)oxy]benzo[1,2-b:4,5-b]dithiophene-2,6-diyl3-fluoro-2-[(2-ethylhexyl)carbonyl]thieno[3,4-b]thiophenediyl)

DTBT[7], PBnDTDTBT[8] and PBnDTTAZ[9]. They also found that face-on interfacial conformation was the main reason behind observed high device performance. They suggested that polymer molecular orientation dependence on solvent and material choice stemmed from differences in pre-aggregation in the solvent due to differences in backbone and side-chain solubility, as well as different morphological evolution during film casting.[112]

More recently, McGehee et al. using steric control (linear vs. branched side chains) on a series of PBDTTPD derivatives,[10] showed the influence of fullerene docking site of the polymer on charge separation efficiency. It appears that in BHJs based on push-pull polymers, when the acceptor moiety on the polymer is more sterically accessible and the donor moiety is more sterically hindered, the device performance is significantly increased (Figure 2.5). The work further supported the view that control of polymer:fullerene arrangement is critical to better photovoltaic performance in OPVs.[109]

2.2.2.2 Small molecules and oligomers

A number of small molecules donors, with different molecular geometry and size, and covering a wide range of degree of order are used in OSCs. Amongst these molecular donors, some of the most applied are acenes based small molecules, cyanines and phthalocyanines, oligothiophenes and Three-dimensional conjugated systems based on triphenylamine.[93] Cheap and highly absorbing small molecules metal based phthalocyanine often form highly oriented donor thin films with tunable molecular orientation.[114–119] These materials have been used in several studies to elucidate the role of donor molecular structure on OPV device performance. Molecular orienta-

[7]PNDTDTBTDTBT:poly[naphtho[2,1-b:3,4-b]dithiophene4,7-di(thiophen-2-yl)benzothiadiazole]
[8]PBnDTDTBT:polybenzo[1,2-b:4,5-b]dithiophene4,7-di(thiophen-2-yl)benzothiadiazole]
[9]PBnDTTAZ:polybenzo[1,2-b:4,5-b]dithiophene-2-alkyl-benzo[d][1,2,3]triazoles
[10]PBDTTPD: Poly[[5-(2-ethylhexyl)-5,6-dihydro-4,6-dioxo-4H-thieno[3,4-c]pyrrole-1,3-diyl][4,8-bis[(2-ethylhexyl)oxy]benzo[1,2-b:4,5-b]dithiophene-2,6-diyl]]

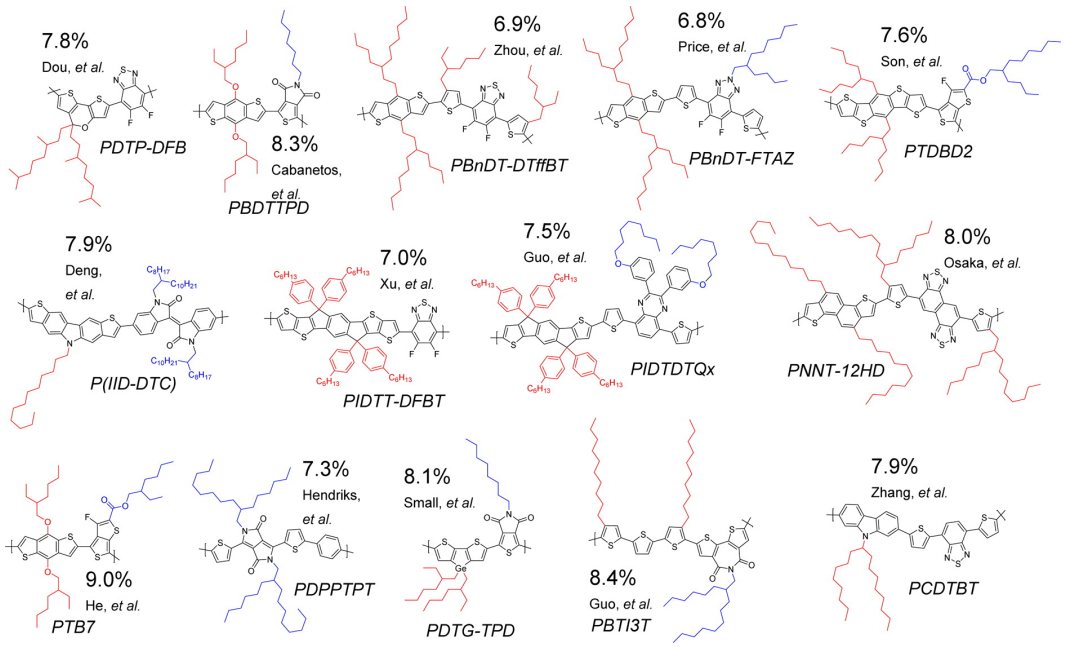

Figure 2.5: High-performing PV polymers and their power conversion efficiencies as reported in the literature, with red and blue substituents off the D and A moieties, respectively.[109]

tion of both planar zinc phthalocyanine (ZnPc) and copper phthalocyanines (CuPc), and thin films of other non-planar molecule such as lead phthalocyanine are particularly sensitive to substrate treatment.[114, 120, 121] For instance, thin layer of metal halide copper iodide on glass substrates coerces ZnPc and CuPc to switch from an edge-on to face-on packing. Such changes in molecular packing have been shown to affect pure thin film absorbance and the overall cell performance when applied in bilayer systems with fullerene as an acceptor.[114, 120, 121] Such improvements clearly indicate significant interfacial changes with change in the molecular orientation. Rand *et al.* suggested that the observed improved performance in the bilayer devices with ZnPc in the face on conformation was in part due to an increase in internal quantum efficiency accounted for via an improved D-A interfacial charge transfer. The acene based amorphous donor rubrene may form highly crystalline and optically thick films upon thermal annealing. The resulting films have been successfully applied

to OPV devices with donor layers thicknesses of up to 400 nm, suggesting that the exciton diffusion in the annealed rubrene films is significantly increased compare to that of amorphous films.[122] Although Jsc was significantly increased when annealed rubrene films were used, the Voc dropped by about 300 meV, suggesting that the gain secured in the bulk was compromised by losses at the D-A interface. Structural control in solution processed small molecule oligomers has been used to improve device performance using techniques akin to that discussed in the case of polymeric donors. Bazan et al. demonstrate interplay between intramolecular electronic structure and intermolecular packing preference in the solid state for a set of four isomorphic organic semiconductors. They altered a functional group on the molecule backbone and by that were able to control whether the donor molecule oriented on the substrate face-on or edge-on.[98]

2.2.3 Relationship between microstructure and energy landscape

A conjugated polymer film is composed of many individual polymer chains; what we have argued till this point is that, both the physical conformation of these chains and the way they pack together in a film determine many of the important optical and electronic properties that are critical to the operation of devices based on these materials. Polymer films consist of a large number of polymer chains. The way these chains organized internally and among themselves strongly influence the thin film optical properties. A single polymer chain can coil or twist. The level of coiling or twisting in the chain determines its effective conjugation length.[123–125] Several polymer chains may pack together, in a $\pi - \pi$ fashion, allowing the chromophores on their backbone to share their $\pi-$electrons and thus enabling charge delocalization. Often, static absorption measurements are used as a fingerprint of the microstructure. Typically, ordered polymers are made of microcrystalline domains embedded

in an amorphous matrix. Comparison of the absorption spectrum of RR-P3HT and RRa-P3HT shows significant differences in spectral shapes and shifts in the spectral position of the main vibronic peak by up to 0.45 eV.[126] In RR-P3HT, various degrees of redshift are often observed going from the solution phase to the crystalline phase depending on the film processing. The degree of shift and the evolution in the spectral shape have been attributed to the microstructure-dependent interplay of interchain (H-favoring) and intrachain (J-favoring) excitonic coupling.[127] More recently such large shifts were rather attributed to the level of torsion between the thiophene rings inside the P3HT chain.[128] Experimental studies on single crystals, thin films, and solutions of RR-P3HT show distinct absorption features associated with the amorphous and crystalline phase of the P3HT. A significant blue shift in the absorption onset of ∼70 nm was observed in going from single crystal to the thin film.[129] In addition to optical properties, electronic properties are also strongly affected by the microstructure. The ionizations potentials and electron affinities have been shown to vary significantly between amorphous and crystalline phase even for a single film (Figure 2.6).[130]

2.2.4 Electronic structure at the donor acceptor interface and role of molecular interactions

2.2.4.1 Intermixing

The morphology of blends is not the simple result of how the components of the blends solidify from solution or from vapors, but depends, in addition, on whether the component of the blends can lower the overall blend's free energy by forming a mixture. In the case of polymer fullerene systems, a number of studies demonstrate a strong tendency of polymers to mix with fullerenes (miscibility for P3HT volume fractions exceeding∼0.42) [52, 131] forming large volumes of mixed phases.[52, 92, 132–134] Interdiffusion studies in a P3HT/PCBM system have shown that $PC_{60}BM$

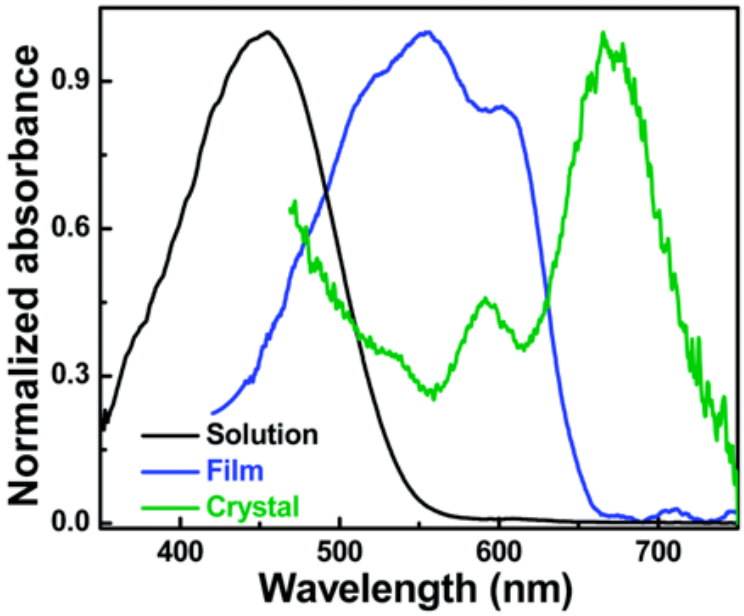

Figure 2.6: Normalized UV-Vis absorption spectra of P3HT solution (0.2 mg ml_1) at 50 °C (black), thin film of a thickness of ∼65 nm spin-cast from a homogeneous solution in 3-hexylthiophene (blue) and a single crystal of a thickness of ∼59 nm (olive) spin cast from a 3-hexylthiophene dispersion.[129]

aggregates and $PC_{60}BM$ molecular species are mobile in disordered P3HT phases in which they mix strongly, but remain immiscible in the lamellarly stacked P3HT chains.[132]

Using GISANS (grazing incidence small-angle neutron scattering), Ruderer et al. have shown that 18% vol of the film in ratio symmetric P3HT/PCBM blend is composed of molecularly dispersed PCBM in an amorphous P3HT matrix.[135] They also found that the amount of molecularly dispersed PCBM increases with the overall PCBM content suggesting that the intermixing of P3HT and PCBM is driven by strong intermolecular interaction in agreement with reported P3HT melting point depression in P3HT:PCBM blends.[131]

Other polymeric systems such as MDMO-PPV[11] [136] and pBTTT[12] have also been

[11]MDMO-PPV:Poly[2-methoxy-5-(3,7-dimethyloctyloxy)-1,4-phenylenevinylene]
[12]pBTTT:Poly(2,5-bis(3-hexadecylthiophen-2-yl)thieno[3,2-b]thiophene)

shown to strongly interact with PCBM. In the case of pBTTT: $PC_{71}BM$, research has shown that a highly ordered and thermodynamically stable bimolecular crystal is formed when the two materials were mixed. The intercalation was possible because of the presence of a free volume between the polymer side chains in which fullerene cage could fit (Figure 2.7).[136] Intercalations with fullerene have also been observed in many other polymer-fullerene systems.[137, 138] The general trend is that strong polymer-fullerene interactions exist in blends and are of the type Van der Waals. These interactions form a significant driving force for molecular mixing in most polymer-fullerene systems.[139]

Research also indicates that in high performing bulk heterojunction systems, the observed near-unity quantum yield is mostly accounted for by invoking the presence of high volumes of mixed phase. Similarly, increased photovoltaic performance in bilayer solar cells has been observed as a result of spontaneous interfacial mixing.[140, 141]

In small molecules, a number of theoretical studies point to strong miscibility between fullerene-C_{60} and donor molecules. Studies based on molecular dynamics simulations show markedly different mixing behavior with respect to the orientation in the squaraine-C_{60} and pentacene-C_{60} layer (Figure 2.8). When the squaraine and pentacene crystals are allowed to interact edge-on with C_{60} no mixing was observed. However when cofacial/face-on conformations were favored, substantial intermixing and disorder was observed in both systems.[50, 142] Based on neutron reflectivity experiments, studies on a BODIPY-based[13] bilayer system have equally shown a significant amount of interfacial mixing with the estimated thickness of the mixed layer to be ca.13 nm.[140]

[13]BODIPY:boron-dipyrromethene

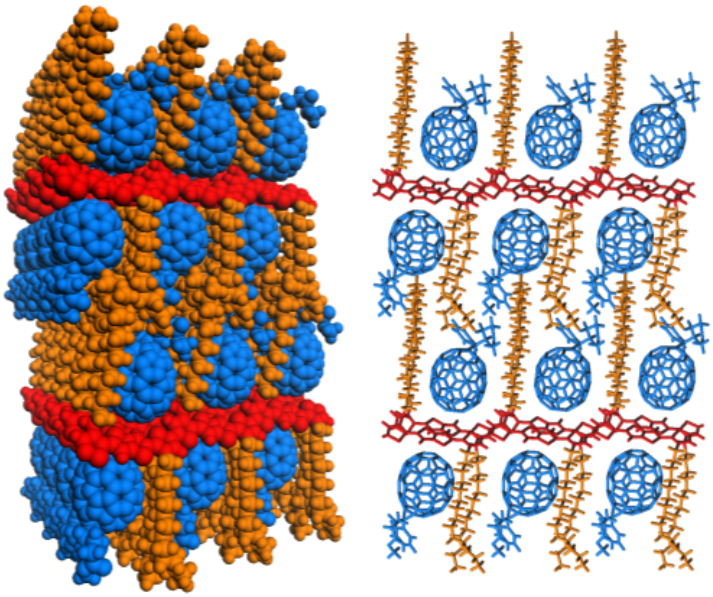

Figure 2.7: Space-filling structure of the PBTTT-C14:$PC_{71}BM$ bimolecular crystal. The polymer backbones, polymer side chains and fullerene molecules are red, orange and blue, respectively. The bimolecular crystal is viewed along the baxis of the co-crystal. This work first demonstrated the importance of molecular interaction in polymer-fullerene blends leading to intermixing in both semicrystalline and amorphous blends. Strong interactions between PBTTT and $PC_{71}BM$ drive fullerene into PBTTT, disrupting the PBTTT packing and inducing bends and twists in the PBTTT backbone and side chains.[143]

2.2.4.2 Role of the mixed phase

We have discussed how energy levels shift depending on the aggregation state-of-the-art material. The near unity quantum yield [144] in efficient organic solar cells would be synonymous to most excitons generated upon light absorption being effectively quenched and therefore suggesting a good amount of intermixing in the BHJ. Beyond enabling efficient excitons quenching (hence making exciton diffusion less necessary), mixed phases also enable efficient exciton splitting because materials band gap and energy levels of both the donor and the acceptor are significantly shifted, due to disorder, with respect to the ordered pure phases.[19, 129, 145, 146] CT excitons

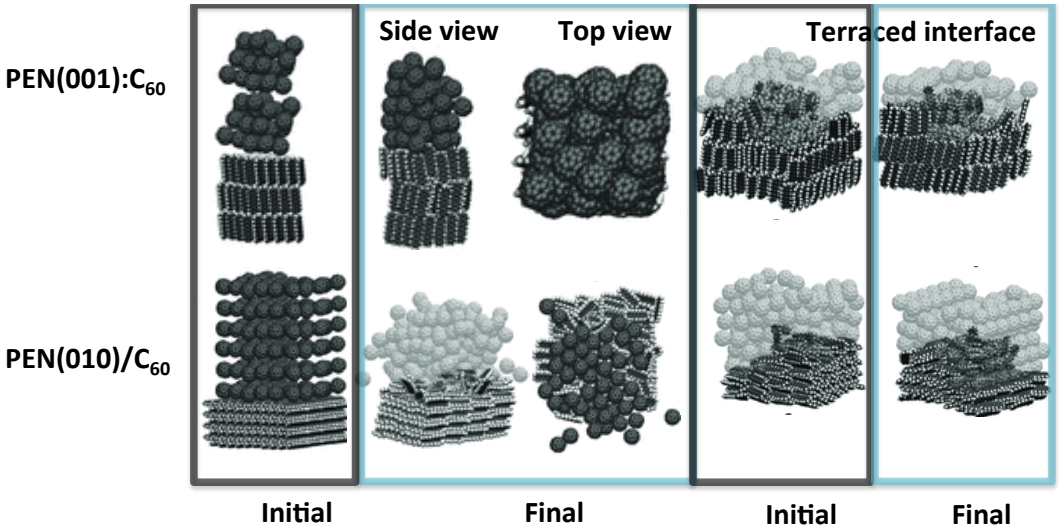

Figure 2.8: Initial configurations and snapshots of the side and top view after an elapsed time of 1.5 ns for: pentacene (001):C_{60} and pentacene (010):C_{60} with the pentacene crystal terminated with flat surface in the initial configuration; pentacene (001):C_{60} and pentacene (010):C_{60} with the pentacene crystal terminated with a terraced surface in the initial configuration. A significant amount of disorder and intermixing is seen at the pentacene/C_{60} interface in all cases except at the pentacene (001):C_{60} interface with the pentacene crystal terminated with a flat surface in the initial configuration.[142]

in the mixed phase thus experience a downhill energy gradient that facilitates their dissociation into free carriers by providing the driving force necessary to overcome coulombic binding. Reciprocally, free carriers experience energetic barriers towards the heterojunction, which limits the rate of carriers encounters and thus the rate of bimolecular recombinations (Figure 2.9). Another important factor is that of fullerene percolation in the mixed phase. Fullerene loading in the blends should exceed a certain threshold to form continuous transport paths without which the otherwise discontinuous fullerene domains would constitute morphological electron traps that would increase charge-carrier recombination.[147] These requirements become crucial in optically thick cells in which carriers need to move over hundreds of nanometers before they reach an electrode.

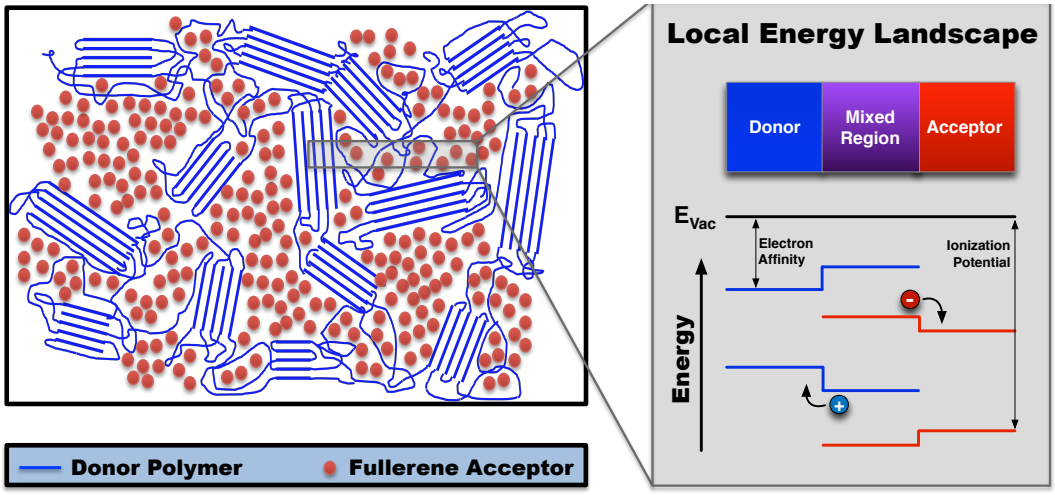

Figure 2.9: Right: Schematic of a BHJ solar cell based a semicrystalline polymer miscible with fullerene. Left: diagram showing the shifts in the local energetic landscape at the phase boundary between the donor, mixed and acceptor phases. EA is the electron affinity, IP is the ionization potential.[19]

2.2.5 Interactions causing energy level shifts

As we discussed above, the energy levels of the isolated donor and acceptor have little relevance for the understanding of the processes that occur during the photovoltaic action. When donor and acceptor materials come together, they form a composite whose electronic properties can be quite different from that of the separated materials. In most donor acceptor systems relevant for OPVs, these interactions have been shown to be essentially electrostatic in nature, [146, 148–150] involving dipoles or mutually induced dipoles, quadrupoles, or multipolar interactions, with only a few cases where strong interfacial molecular interactions inducing significant charge transfer in the order of $0.1|e|$ per molecule were observed.[151] Experimental and computational research have also shown that not only do these interactions drive the formation of the mixed phase as discussed above, they equally shift energy levels significantly.

Using Raman spectroscopy, Sweetnam et al. [146] In a comparative study of RR-P3HT:$PC_{70}BM$, RRa-P3HT:$PC_{70}BM$ blends, and pBTTT with a selected set of

PCBM derivatives, they conclusively show that energy levels shifts in the co-crystal of pBTTT:$PC_{70}BM$ are primarily due to conformational changes in the pBTTT polymer backbone, which becomes more planar in the crystal, and not to charge transfer. This work also highlighted the influence of conformation on interfacial energetics. In general, conjugated polymers and small molecules may exhibit permanent dipoles, quadrupoles, and other multipoles. In the case of the P3HT:PCBM systems, for instance, theoretical studies predict formation of large dipoles at the interface of PCBM that arise through polarization of the electron cloud of P3HT by the permanent dipole moment of PCBM.[152] Such induced polarization has been modeled using quantum mechanical methods in small molecule-fullerene bilayers. It was found that the local dipole at the interface was very sensitive to the relative arrangements of the pentacene and C_{60} molecules.[148] The presence of these interfacial dipoles has been linked through experimentation to detected shifts and broadening in the polymer HOMO and fullerene LUMO densities of states.[146]

Sweetnam and co-workers [153] have estimated that these shifts could be greater than 350 meV in the polymer in the case of the P3HT:PCBM blend. These interactions tend to destabilize the hole right at the donor acceptor interface or in the mixed phase, hence favoring CT excitons dissociation. Similarly, observations stemming from work on small molecules based model systems where the energetics at the heterojunction F_{16}-CuPc (face-on) or F_{16}-CuPc (edge-on) and PTCDA[14] was found to differ significantly, with the HOMO of the top PTCDA layers on the face-on F_{16}CuPc thin film is 0.3 eV higher than those on the edge-on F_{16}-CuPc thin film.[133]

[14]PTCDA:3,4,9,10-perylenetetracarboxylic dianhydride

2.2.6 Impact of interfacial molecular structure on carriers generation

2.2.6.1 Role of conformation and separation distance

The D-A interfacial energy level alignment depends strongly on the local geometry, namely the relative conformation and separation distance of the donor and the acceptor.[133] More specifically, the energy of the charge-transfer state varies with donor conformation and is expected to increase with their separation. Work based on P3HT and functionalized POPT[15] donor polymers blended with CN-PPV[16] [154] demonstrated the role of separation distance on the energy of the charge transfer state. For the P3HT:CNPPV system (with no side chains on P3HT) the CT energy of the single CT band falls in between the CT energies of the CT bands detected in the case of POPT:CNPPV system (with side chains on POPT). The author further sustained this experimental observation using computational methods that suggested an important role of both D-A separation and relative molecular conformation at the interface. The two CT bands in POPT:CNPPV blends were assigned to different POPT-CNPPV relative conformations. The out-of-plane twist of the phenyl rings was said to increase the separation distance between POPT and the acceptor molecule likely through steric repulsion from the phenyl rings, thus hindering direct backbone-to-backbone interactions. This would thus lead to the formation of the high-lying CT state. The low-lying CT state would correspond to a conformation whereby CNPPV more closely interacts with an accessible segment of the POPT polymer. Quantum mechanical studies in the case of OPVs based on small molecule pentacene and fullerene,[47] found an intriguing relationship between donor-acceptor separation and degree of charge delocalization. Decreasing the extent of donor-acceptor interactions by increasing their separation lead to more delocalization of charge and increase in

[15]POPT:Phenyloctyl substituted thiophene
[16]CN-PPV:Cyano-Polyphenylene vinylene

the CT energy as a result of the decrease in electronhole binding energy.

2.2.7 Influence of the extent of order: Delocalization

In addition to being instrumental for bulk charge and exciton transport, research shows that the extent of aggregation of both D and A play a crucial role at the donor acceptor interface in terms of energetics. We shall now discuss the implications of the aggregation of D and A for CT energy.

2.2.7.1 Role of fullerene aggregation

Several studies support the idea that CT excitons formation from free carriers does not necessarily result into charge annihilation. As discussed above, carriers would undergo several attempts to dissociate from CT states mainly because CT states have an appreciable lifetime (100 ps to several ns), which exceeds the time necessary for charges separation to occur. [76, 155, 156] In the absence of an energy gradient that would favor charge intermolecular hopping away from the interface, entropy would be the dominant mechanism by which free carriers formation from bound CT states would occur.[17] However, for this mechanism to be operative, the high entropic states in which charges would be free from coulombic interaction need to be in the vicinity of the heterojunction in the form of delocalized band states. Research based on atomistic modeling and ultrafast optical probes showed that efficient dissociation occurs when the interfacial bound electron-hole pairs are promoted, via infrared illumination, to delocalized band states.[76] This conclusion can be paralleled with similar work that has posed the need for such delocalized states as a necessary condition for a long-distance electron transfer to occur, effectively turning otherwise "cold" excitons into "hot" CT excitons that have high chances of escaping the Coulomb trap.[69] Using electro-absorption measurements, Giebink et al. show that C_{60} aggregates of size

at ∼4 nm are required for efficient separation in NPD:C_{60} blends[17]. The increase in amorphous NPD ratio in these blends was found to disrupt C_{60} aggregation and control blend dielectric constant which result in an increased CT state energy because of increased electron confinement in less aggregated fullerene-C_{60} (Figure 2.10).[157] More recently, studies investigating recombination via CT states in polymer:fullerene blends with aggregated and non-aggregated soluble fullerene derivatives show that relaxations of CT_3 to T_1 were important only in blends with non-aggregated PCBM clearly indicating the role of PCBM aggregates in providing alternative pathways that compete efficiently with relaxation to T_1.[41] In PCDTBT:$PCB_{61}M$ photovoltaic blends, CT excitons were found to create free charge carriers very efficiently on an ultrafast time scale. The observed low efficiency of the device was attributed to a large amount of bimolecular recombination and not to an inefficient CT excitons splitting corroborating the now accepted picture that CT excitons split efficiently in most OPVs.[158] Durrant et al. show that PCBM crystallization causes its electron affinity to increase, providing an energetic driving force for spatial separation of electrons and holes. They propose that a key attribute of PCBM is its ability to both mix with donor polymers while at the same time form co-existing relatively pure crystalline domains with a higher electron affinity which offers a driving force for electrons out of the mixed phase.[77]

2.2.7.2 Role of donor aggregation

First principle calculations performed on a pentacene/C_{60} interface have shown a very strong dependence of the extent of hole delocalization on the interfacial energetics.[47] Increasing the size of pentacene clusters resulted in the enhancement of hole delocalization and the lowering of the energy of CT state and the decrease of the CT state state binding energy. The lowering of the CT state energy was mainly due to the

[17]NPD:N,N-Di(1-naphthyl)-N,N-diphenyl-(1,1-biphenyl)-4,4-diamine

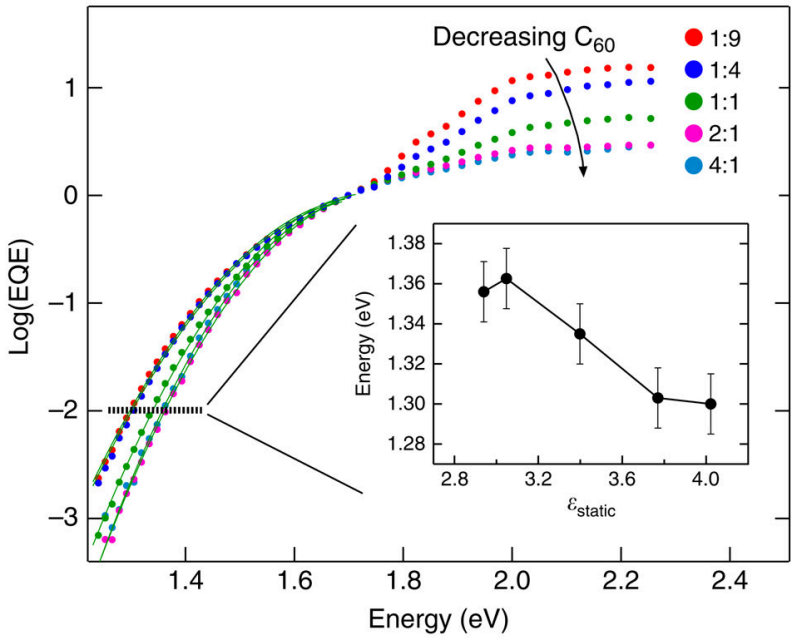

Figure 2.10: External quantum efficiency (EQE) data for devices with varying (NPD):C_{60} ratio, Green lines indicate fits and the inset displays the energy shift occurring along the dashed line at constant EQE. Error bars in the inset reflect the standard deviations estimated from EQE measurements on multiple devices.[157]

lowering of the ionization potential of the pentacene cluster. Polarons and excitons in microcrystalline RR-P3HT thin films have been suggested to exhibit an intra and intermolecular character revealing the important role of interchain interactions.[111] Salleo et al. have investigated interfacial energetics in organic ternary blends. Using aggregating polymers and miscible fullerenes. By varying the degree of aggregation of polymer and fullerene, they found that besides polarization, polymers aggregation was responsible for the formation of the lowest-energy charge transfer states, which primarily determined Voc. They also found that in a ternary blend, with two polymers exhibiting different degree of aggregation, interfacial CT states population was significantly influenced by both of the polymers and their structural orders and morphology carried over to Voc as an indirect consequence of the modulation of CT states distribution. Vandewal et al., by controlling the fraction of P3HT fibrils in

blends of P3HT:PCBM, observed a redshift in CT state energy as the fraction of P3HT fibrils was increased and remarked that changes in CT state energy correlated well with changes in device Voc. The redshifts in CT sate energies were assigned to corresponding shifts in polymers HOMO level that follow polymer aggregation into nanofibrils (Figure 2.11).[159]

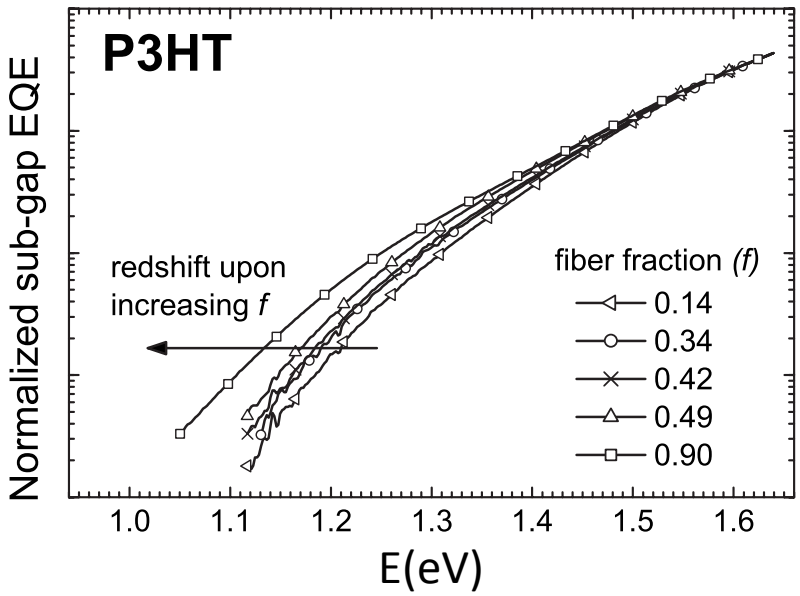

Figure 2.11: EQE spectra measured in the subgap region of nanofiber P3HT:PCBM photovoltaic devices with a defined P3HT nanofiber to total polymer fraction f. Upon increasing the fiber fraction, the CT absorption band redshifts.[159]

2.3 The charge-transfer state energy and the open circuit voltage

We would first like to describe the process of free carriers generation in organic solar cells as a preface to the discussion of the relationship between the charge-transfer state energy and the open circuit voltage. As discussed earlier, in order to split the bound excitons a driving force is required to overcome the coulombic interaction between the electron and the hole. This is achieved with the offset in the energy levels

of the donor and the acceptor, which promotes photoinduced electron transfer to the acceptor. However, there is evidence that after this initial stage of the charge transfer process, the hole on the donor and the electron on the acceptor still remain coulombically bound forming interfacial charge transfer state excitons. The evidence for such bound excitons has been demonstrated through several studies based on highly sensitive measurements of the absorption and photovoltaic action spectrum, or in photoluminescence and electroluminescence measurements through donor acceptor interfaces.[160–163] Because of the energy level offset at the donor acceptor interface, the downhill electron transfer implies energy losses for the excitons. The bound CT excitons thus have a smaller energy separation than the excitons in the donor bulk. Thus, although the absorption occurs in the bulk of the donor and not at the interface, the Voc is not related to the optical gap of the donor but to the interfacial gap corresponding to the direct optical transition from excitations of subgap interfacial CT states (charge-transfer transition)[43, 44] or their radiative below gap decay.[164, 165]

In reality, this upper bound is almost never achieved because of other processes, geminate and non-geminate recombination for instance, that compete with CT excitons dissociation into free carriers. A rigorous analysis by Koen et al. based on the assumptions of the detailed balance, has shown that the photovolatge of organic solar cells is ultimately determined by the charge transfer state energy but diminished by losses due to the high number of donor acceptor interfacial contacts and the presence of non radiative recombinations pathways, often quantified in terms of the electroluminescence yield.[160, 166] One of the strengths of the model is that it allows extraction of the CT state energy very accurately; morphological effects and electronic interactions are taken into account, and accurate estimation of Voc losses from simple measurements of subgap quantum yield can be achieved. This model suggests that the open circuit voltage would be increased by reducing the number of

interfacial contacts and nonradiative recombination pathways which are essentially CT states vibrational modes that allow the CT excitons to return to the ground state through thermal relaxation.[167] In this model, however the entropic contribution to Voc is not considered.

In fact, CT excitons have a certain lifetime; therefore CT exciton dissociation is not a one-off process. Free carriers can meet and form CT excitons, which can undergo several attempts to split, therefore increasing the probability of dissociation. More recently, Burke et al, have shown that these multiple attempts to dissociation agree with the commonly observed reduced Langevin recombination factor and implies that there exists a thermodynamic equilibrium between charge transfer (CT) states and free carriers.[20] This description implies a greater role of entropy, which thus provides a driving force for exciton dissociation. The model links open-circuit voltage loss of organic solar cells to the high extent of interfacial mixing, low CT state lifetime, large amounts of interfacial energetic disorder and CT state binding energies hence suggesting at the same time how each of these factors should be optimized to improve Voc. Studies based on Monte Carlo simulations have also shown, that a fundamental requirements for efficient dissociation from relaxed CT states are high CT states lifetimes and high local mobilities.[19] High CT state lifetimes enable multiple attempts to dissociation for CT excitons while a high local mobility gives the electron a chance to escape the Coulombic well as results of extended hops. Voc can be readily expressed in terms of interfacial energetics. We now wish to present commonly used models for Voc while highlighting their important features.

2.4 Relationship between interfacial energetics and open circuit voltage

There exist several models in the literature that describe Voc using electrical models and various degrees of empirical and molecular descriptors.[168–173] In this section we

discuss the most common models, emphasizing their predictive power and the degree to which they capture the relevant materials structure. It is widely acknowledged that when ohmic contacts are deployed, Voc depends primarily on the electronic states of the hole and electron transport materials and not the electrode work functions. Equation 2.7 describes one such model.

$$\mathrm{qVoc} = (\mathrm{IP_D} - \mathrm{EA_A}) - \mathrm{q}\Delta\mathrm{Voc} \tag{2.7}$$

Where $\mathrm{IP_D}$ and $\mathrm{EA_A}$ are the ionization potentials and electron affinity of the donor and acceptor respectively. $\mathrm{q}\Delta\mathrm{Voc}$ is an empirical term whose numerical value is often taken to be between 0.3 eV and 0.6 eV with some deviations.

Equation 2.7 suggests three ideas. The first is that to maximize Voc, it is sufficient to maximize the first term by designing material that can achieve a wider interfacial gap ($\mathrm{E_g^{DA}} = \mathrm{IP_D} - \mathrm{EA_A}$). While this is an important guideline, it inadequately suggests that pair of donor acceptor materials with the same interfacial gap will yield the same Voc. The second is that $\mathrm{IP_D}$ and $\mathrm{EA_A}$ often refer to their values for the isolated materials ignoring the important role of interactions in the blend. Finally, the empirical loss term $\mathrm{q}\Delta\mathrm{Voc}$, regarded as a constant, carries no clues of its origin, its expected dependence on temperature, and of how it can be minimized.

Considering Voc as the energetic distance that corresponds to the splitting of the quasi Fermi levels of holes and electrons in D and A and using classical semiconductor theory for perfectly ordered semiconductors, Voc takes the form of Equation 2.8.

$$qV_{oc} = E_F^n - E_F^p = E_g^{DA} - kTln\frac{N_C N_V}{n * p} \tag{2.8}$$

Where N_C and N_V are effective densities of states for electrons and holes in the semiconductors, and n and p are volumes densities of electrons and holes. The assumption that goes into this equation is that the product $n * p$ in Equation 2.8 is set by the

equilibrium between recombination and generation.

In this model, the loss term clearly indicates linear temperature dependence and a logarithmic dependence on effective densities and carriers concentrations. Equation 2.8 suggests that high Voc is achieved (maximum splitting of the quasi Fermi levels) for a wide interfacial gap, and low effective densities of states and high charge concentration (at Voc) around the hole and electron transport levels. These typical values of charge carrier densities at 1 sun illumination are n, p=$10^{16} - 10^{17} cm^{-3}$ [42, 174] and $N_{C,V} = 10^{20} - 10^{21} cm^3$. With these numbers, Equation 2.8 predicts Voc losses in the range of 0.3 to 0.6 V in agreement with experimental observations.[46, 168] Clearly, the model fails however, to capture disorder in the organic materials and more importantly does not account for the recombination that would result from the expected voltage dependence of n and p. Thus models that account for the broadening of electronic transport levels been proposed (Equation 2.9).

$$qV_{oc} = E_F^n - E_F^p = E_g^{DA} - (\sigma_n^2 + \sigma_p^2)/2kT - kTln\frac{N_C N_V}{n * p} \tag{2.9}$$

Where $\sigma_n$and $\sigma_p$are the width of the densities of states for electrons and holes respectively. In taking into account the energetic disorder, Equation 2.9 does capture a key structural feature of the organic semiconductor. However, the premises of both Equation 2.8& 2.9 hinge on the equilibrium between direct band-to-band recombination and generation at Voc. However, in organic bulk heterojunctions, free electron, and holes mostly recombine via CT states. Therefore CT states characteristics should feature in any description of Voc.

Assumptions should now be made regarding recombinations through CT sates. Experimental observations motivate three important assumptions. (1) CT states formation arises from encounters of free carriers (2) CT states can disappear by either recombination or dissociation (3) free carrier generation occurs via dissociation of relaxed CT states (4) there is reciprocity between CT absorption absorption and electrolu-

minescence. (1) and (2) simply say the CT states are formed from free carriers and they form and dissociate faster that they relaxed into the ground state. So effectively CT states should be regarded as free carriers generation centers. Based on the above assumptions and by modeling CT states as Marcus absorbers, Vandewal et al arrived at Equation 2.10 for Voc:

$$V_{oc} = \frac{E_{CT}}{q} + \frac{kT}{q} ln \frac{J_{sc} h^3 c^2}{f q 2\pi E_{CT}} + \frac{kT}{q} ln(EQE_{EL}) \tag{2.10}$$

Where $f = IQE_P V * f_\sigma * N_{CT}$. f is oscillator strength factor which scales with the internal quantum efficiency of the photovoltaic action from direct CT state absorption (IQE_{PV}), the oscillator strength associated with the direct transition from ground state to CT states (f_σ) and the number density of interfacial CT complexes (N_{CT}). E_{CT} is the energy of the charge transfer state, λ the reorganization energy associated with a CT absorption event and EQE_{EL} the external quantum efficiency of CT state electroluminescence. Equation 2.10 suggests that Voc is determined by CT state properties through, energy of the charge transfer state ($\mathrm{E_{CT}}$), f and λ. It also shows the functional dependence of Voc on temperature and allows extrapolating at 0 K. In fact, extrapolation Voc (T) to 0 K for organic solar cells agree exceptionally well with E_V.[45] Equation 2.10 also suggests ways to minimize Voc losses. Increasing the energy of the CT state, reducing the f term by reducing the density of charge transfer complexes N_{CT} or decreasing non-radiative recombination (by increasing EQE_{EL}) will also improve Voc. With the additional that CT states formation is in equilibrium with free carriers formation from CT states, Equation 2.11 can de derived.

$$qV_{oc} = E_{CT}^{exp} - ln(\frac{qfN_0 L}{\tau_{ct} J_s c}) \tag{2.11}$$

Where,

$$E_{CT}^{exp} = E_{CT}^{T=0K} - \sigma^2/2kT \tag{2.12}$$

E_{CT}^{exp} is the temperature-dependent experimental charge transfer state energy, τ_{CT} is the CT state lifetime, f is the fraction of the film forming the interface,N_0 is the molecular density, and L is the thickness of the active layer. To increase Voc, E_{CT} and σ_{CT} need to be increased, the disorder σ decreased and f chosen such that Voc is maximized. The energetic cost associated with the charge transfer process constitutes an unavoidable source of energetic loss in itself. However, several studies have shown that an energy gap as low as 50 meV between S_1 and CT_1 (or CT_3) when fullerenes are used as the acceptor is sufficient for an effective charge transfer [63, 175–177] and no additional benefit results observed when this driving force is increased. The process where free carriers meet and form CT excitons, which may then recombine into the ground state, can reverse the process of the formation of free carriers from CT excitons. Recombination of charges generated from the same exciton differs fundamentally from recombination from a pair of two unrelated free carriers. Understanding and controlling each of this processes is crucial in the effort to improve the photovoltaic performance of organic solar cells.

2.5 Conclusions

The complex molecular arrangements in the bulk heterojunction give rise to an intricate and inhomogeneous landscape, which strongly influences the performance of organic solar cells. This is because the optoelectronic processes that lead to the photovoltaic action are shaped by this energy landscape. The diversity in materials, the variety of processing conditions add to the complexity of the bulk heterojunction itself making attempts to establish structure-property relationship trends in this system extremely challenging. The materials structure right at the heterojunction, in particular, plays a crucial role in determining the efficiency of the photovoltaic action. It is crucial to characterize these interfaces and link their various structural aspects to the efficiency of processes that are primarily governed by molecular struc-

ture. For instance, CT state energy and charge separated states energy depend on the in-situ ionization potential and the electron affinity of the acceptor. These quantities markedly depend on the materials structure of the thin-film and at the heterojunction. Thus, it is important to contrive models that examine the mechanism of this dependence. While techniques such as grazing incidence small-angle neutron scattering (GISANS) enable the investigation of the polymer structure in blends with fullerene, the average fullerene domain size and the interfacial area between polymer and fullerene in BHJ, such techniques remain highly inaccessible to most research groups.[135, 178] In addition, the complexity of data generated by such techniques makes them inaccessible to a large audience. It thus is important to imagine model systems that emulate the BHJ and lend themselves well to common investigation tools and whereby the possible types of interfaces and microstructures present in a typical BHJ are recreated purposely (without relying on the spontaneous development of the microstructure) and their role examined separately. Such studies would guide understanding of particular the role of various structural distinct instances of the heterojunction. Although, sensitive probes such as below gap optical measurements yield important information about interfacial energetics and in particular the charge transfer state energy, they lack specific information about the energetics of individual components in the blend that would inform strategies to improve the photovoltaic performance. Similarly, materials energetics across the bulk heterojunction is often treated without discrimination of the variations in the chemical composition in the phases across the film under consideration notwithstanding the fact that it is commonly observed that vertical differentiation in film composition manifests in these blends. Thus, studies that consider a range of material composition are required. Finally it is critically important to regard CT states as wide distributions of states in accordance to the underlying materials structure complexity.

Chapter 3

Methodology and general description of the work

In this chapter, we present the methodology employed to conduct our research. As discussed in the introduction, we seek to understand what molecular arrangements are prevalent at organic-organic donor-acceptor interfaces and how these arrangements influence the interfacial materials energy landscape and the photophysical processes that influence the photovoltaic action.

We now wish to discuss how such donor-acceptor interfaces were characterized in both thin-films and devices, how molecular structure at interfaces were emulated and how the material systems were selected.

3.1 Thin film deposition methods and interface engineering

The main deposition method we employed throughout this study is vacuum sublimation. We essentially used deposition in Ultra High vacuum (UHV) during the study of interfaces.

3.1.1 The Ultra High Vacuum (UHV) system

The ultra high vacuum system (UHV) used in this research is an Omicron chamber (manufactured by Omicron NanoTechnology, Taunusstein, Germany) equipped with thin film deposition capabilities and surface science tools. Thin film deposition tools are located in a molecular beam epitaxy (MBE) chamber and consist of effusion cells and an e-beam evaporator. The surface science tools, used for surface preparation

and analysis are located in the analysis chamber and consist of spectroscopy tools (including electron diffraction) such as an electron gun, primary beam source(s) such as X-ray and UV-sources. Detection means include an electron energy analyser, a mass spectrometer and a luminescence screen. Samples handling is done with various manipulators, fast entry lock chambers and sample transfer systems (vacuum suitcases). High vacuum is achieved and maintained with the use of several turbo molecular pumps, ions pumps and titanium sublimation pumps.

3.1.2 Deposition strategies and conditions

3.1.2.1 Thin film deposition by Molecular Beam Epitaxy (MBE)

All deposition experiments were performed in conditions which emulate the device fabrication. Organic thin films were mainly fabricated in an MBE deposition chamber (Figure 3.1). The Omicron chamber is equipped with several Knudsen-type cells (Figure 3.2) that allow us to evaporate the small molecules donors and acceptors onto substrates that can be rotated, heated and cooled. The Knudsen cells (Model NTEZ 40-10-KS) are effusion cells equipped with cooling shrouds, a shutter with automated control, heating elements surrounded by a heat shield and a crucible thermocouple assembly mounted on a port flange (Figure 3.2). In addition to having heat shields, the cells also include a water jacket that further enables better temperature control. Besides the excellent temperature control, these cells also display, as a consequence, high flux stability, which allows deposition of submonolayers at very stable rates and high precision. These sources can also be heated simultaneously; a feature which is very useful for the fabrication of blend films. The fast acting shutters (actuation time less than 0.2s) are useful for monolayer film growth control and to avoid undesired composition gradient in blends. To maintain a high purity of the material, I avoided cross-contamination by thoroughly cleaning the source with polar solvents at each material loading cycle. The UHV conditions ensure high directionality of the

molecular beam and little interactions of molecules in the gas phase, before they have reached the substrate.

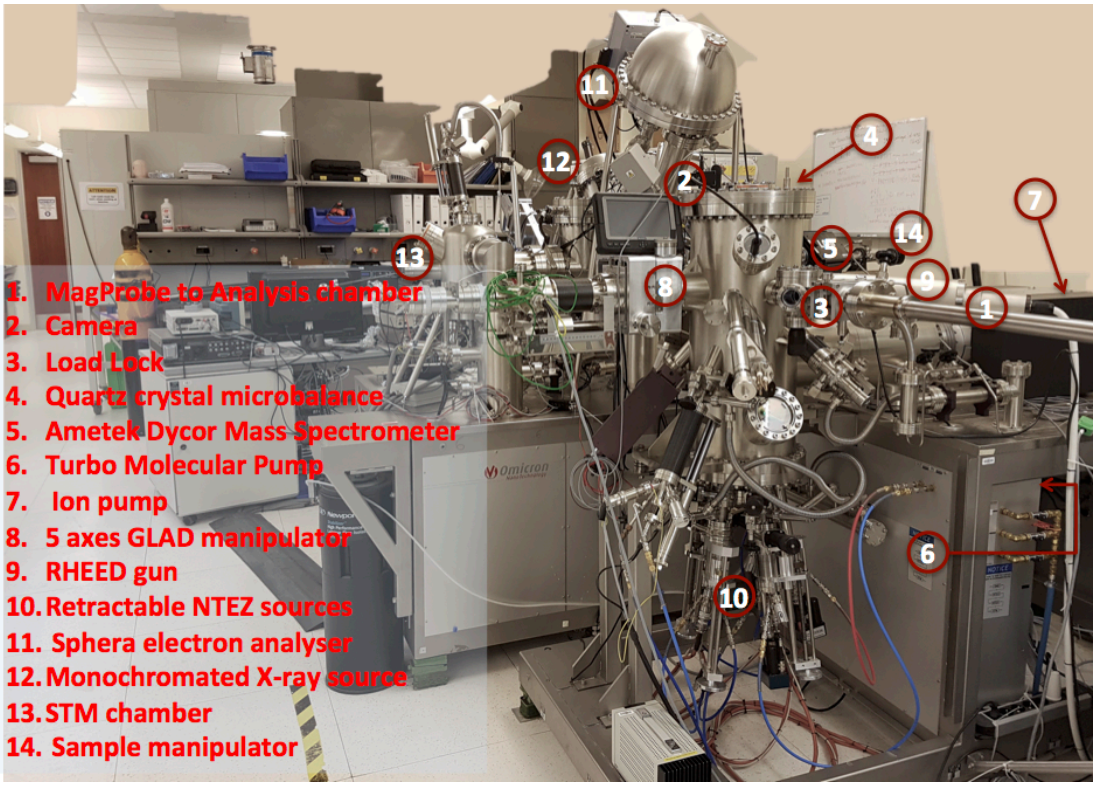

Figure 3.1: Analysis and MBE chambers

3.1.2.2 Deposition of pure films and donor-acceptor blends

For thin films used for XPS and UPS, the films were deposited on argon-sputtered cleaned gold foil. The deposition rate was kept low (<1 Å/s) for pure films of all materials. For blends, two materials were deposited simultaneously. The deposition rate of each material in the blend was adjusted to meet the targeted blend ratio. To ensure rate stability before actual deposition of the blend films, the rate of deposition of each material was monitored separately for a prolonged period. For very dilute blends, further calibration of the deposition rate was performed by subliming about 5 nm of the material with the smallest concentration in the blend at very low rate (0.1

Å /S) and calculating the average deposition rate manually, based on the deposition time. When it was necessary to replicate mixed interfacial layers, thin blend layers were grown at the donor-acceptor interface. By cooling the substrate before depositing the acceptor layer, I could limit spontaneous interfacial mixing.

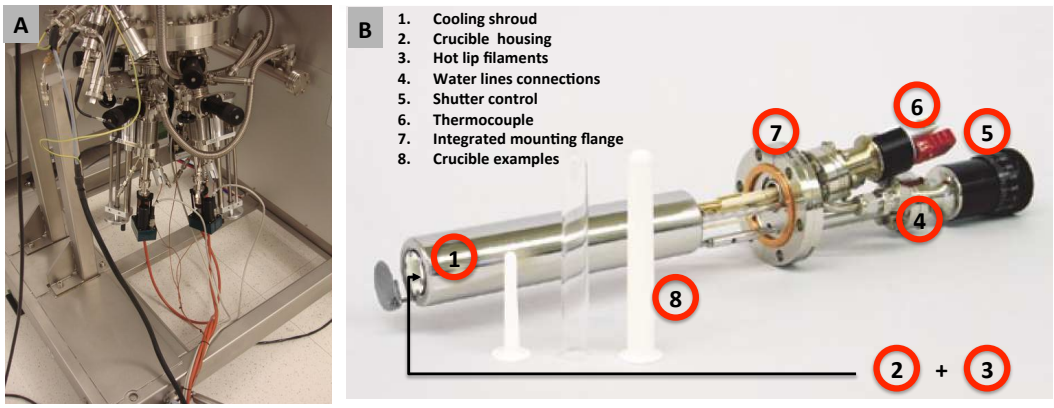

Figure 3.2: (A): Set of NTEZ effusion cells connected to the MBE chamber maintained under UHV conditions (range 1 - 9×10^{-10}mbar). The cells contain the donor molecules and fullerene-C_{60} in the form of powder, which are kept hot to ensure constant degassing of the materials. (B): Internal structure of an MBE Kompenten Knudsen source and examples of crucibles from which materials are sublimed.

3.1.2.3 Substrate temperature control and rotation

Rotation was applied to the substrate during thin film growth to assure better thin uniformity. Rotational speeds of 5 to 10 RPM were used. Substrate heating is achieved through resistive heating of heater made of a tantalum wire mesh at the sample base. At maximum heating power, a substrate temperature of 1000 K can be attained. However the ability to cool the substrate was the most important feature as it allowed to control donor aggregation and interfacial mixing. This was achieved by using liquid nitrogen (LN2) to cool the sample stage. LN2 was fed into the cooling shroud from a condensing coil immersed in an LN2 dewar. Temperature down to 173 K could be achieved. The substrate temperature was monitored with a thermocouple mounted on the substrate stage.

3.1.3 Thin films annealing strategies

I fabricate donor layers exhibiting an heterogeneous structure including both ordered and disordered phases by exploiting rubrene thin film properties. Rubrene can be made crystalline by simple abrupt annealing using a hot plate kept under inert environment. By annealing the as deposited thin film at 150 °C and 170 °C for various durations, I achieved rubrene films containing various fractions of crystalline (triclinic and orthorhombic phase) and amorphous phase. In addition these films (including amorphous films) are textured which gives an additional degree of control over interfacial conformation in bilayers with C_{60}.

3.1.4 Thickness measurement

Film thickness measurements were done in-situ, using a thickness calibrated quartz crystal microbalance. The thickness calibration was done for each material by making thin films of the corresponding material with a series of nominal thicknesses. The actual thickness was then measured using Variable Angle Spectroscopic Ellipsometry (VASE). VASE was performed using an M-2000XI rotating compensator (J. A. Woollam Co., Inc). Films used for Ellipsometry were grown on Si (100) with a 300 nm thermal oxide in MBE or Angstrom evaporator chamber. VASE spectra in the range 210 nm to 1689 nm were recorded at eight different angles of incidence with respect to the substrate normal from 45° to 79°, with 5° increment. The organic film was regarded as isotropic material, and the refractive index was determined using Cauchy dispersion model. All data analysis was performed using the EASETM and WVASE32 software packages (J. A. Woollam Co., Inc). The thickness of inorganic thin films (metal electrodes and copper iodide) was measured using Veeco DEKTAK 6M Stylus Profiler with a vertical resolution of <1 nm. The thickness was determined from the measurement of a step height of trench across the surface.

3.2 Photoelectron spectroscopy

To verify the bulk and interface composition and determine the electronic structure of organic semiconductors thin films, lab based spectroscopic techniques were used. Below we discuss the operating principles of these techniques and how they were used to characterize bulk and interfaces in single layers or stacks.

3.2.1 Ex-situ photoelectron spectroscopy (XPS and UPS)

3.2.1.1 XPS

XPS was used to verify the surface composition of the organic thin films and investigate interfacial mixing. XPS is a commonly used technique for the characterization of surfaces. Its most attractive features include chemical state identification and elemental composition with very high surface sensitivity. Because of this, experiments must be carried out under vacuum (pressure better than 1.0×10^{-6} mbar) to avoid photoelectrons scattering with background gaseous species and surface contamination.

In XPS one uses X-rays of characteristic wavelength to excite strongly bound electrons often called core electrons from the atoms in the sample to the vacuum level (photon-in-electron-out spectroscopy). The electrons emitted from the sample each possess a kinetic energy that is characteristic of the orbital from which the electron was dislodged. The photoelectrons generated are then collected and analyzed with a spherical analyzer. By resolving the kinetic energy of the electrons one can determine the binding energy of the electrons given an appropriate calibration of the spectrometer. Since the intensity of the signal depends on numbers of electrons emitted and their mean free path, knowledge of this latter quantity enables the determination of the sample relative surface composition.

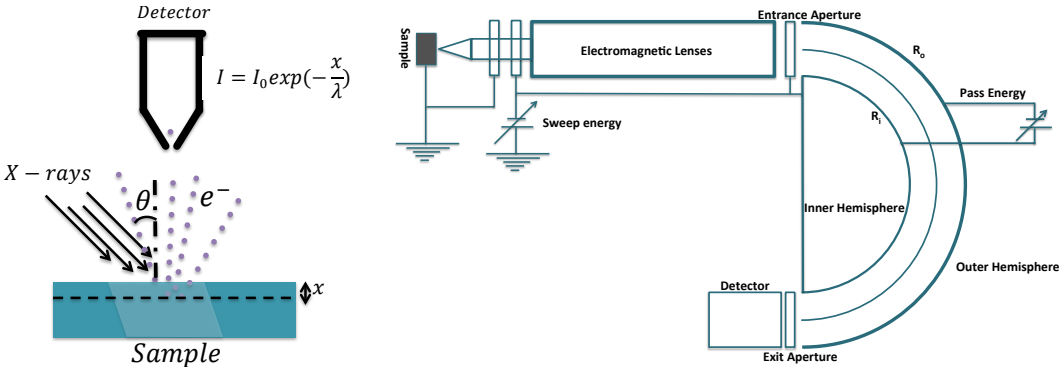

Figure 3.3: Left: Schematic showing the interaction between incoming X-rays and a sample, the resulting photoemission process and the signal intensity dependence on the locus of electrons emission within the sample. Right: Illustrations of the main components of a hemispherical analyser and their relationship to each other.

3.2.1.2 The hemispherical analyzer

The hemispherical analyzer effectively serves as an electron monochromator, which resolves the photoelectron signal in a continuum spectrum. The area of the sample being analyzed is determined by the focal length of the electromagnetic lens placed upfront at the analyzer entrance (Figure 3.3). A certain tolerance on the energy of the electron that is transmitted should be allowed to maximize the photoelectron signal. This is done through controlling the width of the analyzer entrance slit which also determines the acceptance angle. For the XPS spectra, we use an acceptance angle of 8°. Ideally, we would like to use the largest possible slit. However the larger the width of the entrance slit (W), the smaller the resolution ($\frac{\Delta E}{E_P}$), i.e., the broader the peaks (Equation 3.1).

$$\frac{\Delta E}{E_P} \propto \sqrt{\frac{W}{R_P}} \tag{3.1}$$

The pass energy is related to the inner and outer radii of the hemispherical portion

of the analyzer according to Equation 3.2.

$$E_P = K_S(\frac{R_o}{R_i} - \frac{R_i}{R_o})^{-1} \tag{3.2}$$

Where K_S is the spectrometer constant. R_i and R_o are illustrated in (Figure 3.3).

3.2.1.3 Origin of surface sensitivity and spectrum generation in XPS

The X-rays source used in our laboratory is a monochromatized Al Kα excitation (1486.7 eV) connected to the analysis chamber (Figure 3.1). The use of a monochromator (Quartz Crystal) eliminates the presence of photons coming from secondary atomic transitions, which otherwise leads to the appearance of satellite lines in the XPS spectra. For thin films, the incoming X-rays beam interacts with the entire sample volume. Because of the inelastic scattering, most of the photoelectrons do not have sufficient kinetic energy to escape the sample and only those emitted form the near surface monolayers (10 -100 top monolayers) escape and enter the analyser. The thickness of the sample near the surface that is effectively probed by the X-rays, the analysis depth, depends on the electron mean free path (IMFP:λ) near the sample surface. A precise knowledge of the analysis depth can thus be achieved if the inelastic mean free path, λ, of the electrons is known. With the assumption that the photoelectrons do not interact among themselves, the decay in the fraction of photoelectrons intensity emitted from a certain depth within the sample is given by Equation 3.3.

$$I = I_0 \; exp(-\frac{x}{\lambda}) \tag{3.3}$$

Where x is displacement of the electron from its point of photoemission (Figure 3.3). The exponential dependence on the photoelectron signal on distance implies that 95%

of the electrons that make it out of the sample are emitted within 3λ below the sample surface; 3λ thus rightly approximates the analysis depth. In a solid, each excitation possesses a characteristic energy. The energy loss incurred by electrons during a scattering process is thus dependent on their kinetic energy only. For this reason, the IMFP exhibits a quasi-universal behavior.[179] The following relation empirically describes its dependence with the electron kinetic energy E (Equation 3.4).

$$\lambda = \frac{a}{E^2} + b \times \sqrt{E} \tag{3.4}$$

Where a and b are phenomenological constants, which depend on specific nature of the compound. For organic semiconductors, λ is in the order of 5 Å at 100 eV which about the typical intermolecular distance in molecular compounds. Mean free paths, however, are also strongly dependent on materials composition. This fact is exploited in the study of interfaces. When the interface is formed by deposition of an overlayer, the XPS signal coming from the underlayer decays exponentially with the increasing overlayer thickness in the case where there is no intermixing. When there is intermixing, the XPS signal from the underlayer will attenuate less strongly. Comparing XPS signal decay behavior can be used to track intermixing at donor-acceptor interfaces.

3.2.1.4 Quantification in XPS

The measured intensities I_i (Equation 3.5) of the core i levels orbitals is proportional to the number of atoms in the volume N_i, the cross section for photoemission of the core level σ_i the angular distribution factor, the electron mean free path λ, the transmission function of the analyzer T.

$$I_i = k\sigma_i \Phi \lambda T N_i \tag{3.5}$$

Where k is a proportionality constant, which takes into account non-idealities of the instrument. Because of the dependence of the factors such as λ and T on the kinetic energy of the electrons, comparison of peak intensities in XPS requires prior corrections that account for this fact. This is done by applying the appropriate sensitivities factors, as provided by the instrument manufacturer, to measured intensities. λ may need to be further corrected depending on the nature of the sample and the geometry of the experiment. For peak identification and quantification of the spectra, we have used CASAXPS, a software suite commonly used for spectroscopy data processing.

3.2.1.5 Energy of the photoelectrons in XPS

In this discussion, we neglect the role intramolecular relaxation effects that occur after the photoionization process that occurs upon X-ray illumination. This is equivalent to saying that we assume that Koopmans theorem is valid, meaning that no relaxations effects arise when an electron is excited to the vacuum level, and therefore the negative of the orbital energy equates the measured binding energy.

The elastically scattered photoelectrons emitted by the illuminated sample light have kinetic energy that is specific of the orbitals from which they originated. However because the difference in the work function of the sample (Φ_s) and the work function of the analyzer (Φ_a) creates an effective contact potential, the kinetic energy of the electrons as seen by the sample (E_{ks}) and analyzer (E_{ka}) are not identical. The accepted convention is to measure the kinetic energy of the electrons with respect to the reference frame of the analyzer (Figure 3.4).

Thus, the set of relations in the Equations 3.6 to 3.9 hold.

$$E_{ks} = h\nu - (E_b + \Phi_s) \tag{3.6}$$

$$E_{ka} = E_{ks} - (\Phi_a - \Phi_s) \tag{3.7}$$

$$E_{ka} = h\nu - E_b - \Phi_a \tag{3.8}$$

$$E_b = h\nu - E_{ka} - \Phi_a \tag{3.9}$$

Equation 3.9 indicates that the measured binding energies are independent of the work function of the sample, but do depend on the work function of the analyzer. Therefore it is necessary to determine the work function of the analyzer accurately. Calibration of the XPS instrument was carried out regularly using polycrystalline Gold sample of high-purity to determine the work function of the analyzer.

3.2.1.6 Ultraviolet photoelectron spectroscopy (UPS)

X-ray photoelectron spectroscopy has a relatively low energy resolution and photoionization cross-section for states around the Fermi level and is therefore not suitable for an accurate determination of the ionization potential of most organic semiconducting materials. Thus we use UPS to measure the ionization potential of our organic films. UPS experiments were carried out using the analysis chamber of our Omicron ultrahigh-vacuum (UHV) with a base pressure 5×10^{10} mbar. The organic thin films were transferred in the chamber without air exposure from a nitrogen glove box using a vacuum suitcase or in vacuum directly from the MBE chamber. The photoelectron spectra were generated using a hemispherical electron energy analyzer (Omicron EIS-SPHERA). The UPS spectra were measured with pass energies, not more 3.0 eV and a constant pass energy mode. We choose the entrance slit of diameter less than dimater 6mm mm corresponding to an acceptance angle of 8° to both maxi-

mize signal intensity and resolution (Table 3.1). The analyzer resolution (105 meV) was determined by measuring the width of the Fermi edge of a sputtered cleaned polycrystalline gold foil. The film work function was calculated by subtracting the sum of the total width (16.28 eV) of the photoelectron spectrum from the photon energy. A negative bias of 5V was applied to the substrate before the UPS measurement to separate photoelectrons emitted by the sample from those emitted by the analyser.

The ionization potential of the film was determined by adding to the film work function, the valence band onset. Since numbers of organic semiconducting materials absorb light in the UV range, they are prone to degradation under UV irradiation. This is characterized by the distortions of the photoelectron spectra with time while the sample is illuminated. Since the extent of the degradation is proportional to the intensity of the photon beam, a way to prevent or decrease sample degradation is by using an aperture at the source (UV-lamp) to attenuate the intensity of the photons. For most organic thin films we studied, the lamp intensity was attenuated to the twelfth of tits maximum intensity. Also, the dwell time was to further minimized to limit sample exposure to UV-light. We used a two-stage HIS 13 VUV Helium based capillary discharge lamp with photon energy of 21.22eV as the beam source. A 100 mA discharge current was applied such that the emission from the He II line at 40.8 eV was minimal.

Table 3.1: Magnification and corresponding acceptance angles for our omicron SPHERA electron anlyser.

Magnification mode	**Magnification**	**Angular acceptance**	**Analysis area** [1]
High	× 5	±8°	1.5 mm
Medium	× 2	±4 °	3 mm
Low	× 1	±1 °	6mm

[1](diameter) for 6 mm diameter entrance slit. The analysis area is defined as the ratio of the slit size and the magnification.

3.2.1.7 Determination of film Ionization potentials from UPS measurements

The ionization potentials of metals and semiconducting materials can be determined from a UPS spectrum (Figure 3.4). There are however several important assumptions that should hold for the data extracted from the spectra to be meaningful. The first assumption is that the sample is in electrical equilibrium with the analyzer. This is satisfied by using high conducting Gold foil as a substrate and making sure the substrate shares the same ground with the analyzer. The second assumption is that the analyzer work function remains unchanged regardless on the sample being measured. The last assumption is that the lowest kinetic energy electrons (those with effectively zero kinetic energy) originate from the sample and not from the analyzer. It is equivalent to saying that the work function of the analyzer is smaller than the samples work function. This is ensured by negatively biasing the sample, increasing the effective contact potential ($\Phi_a - \Phi_s$) thus giving extra kinetic energy to the otherwise low energy photoelectrons. Equations 3.10 and 3.11 relate the ionization potential and work function of the samples to the photon energy and typical features of a UPS spectrum (Figure 3.4).

$$IP = h\nu - SECO + Onset \tag{3.10}$$

$$WF = \Phi_s = h - SECO \tag{3.11}$$

SECO is the energy corresponding to the cut-off of the spectrum in the region where the signal originates mostly from secondary electrons. The Onset is the energy corresponding to the position of the HOMO or the valence band with respect to the Fermi level (Figure 3.4). The high kinetic energy cut-off occurs when electrons are ejected from the Fermi level, i.e., with the highest kinetic energy hence lowest binding energy.

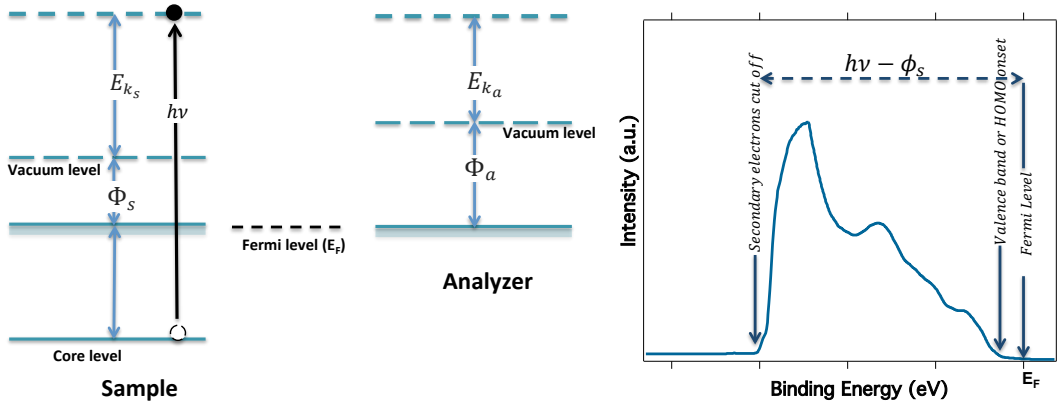

Figure 3.4: (Left) Schematic energy level diagram of a conducting sample in electrical contact with the analyzer. **(Right)** Typical UPS spectrum of a semiconducting sample showing the main features of the spectrum and their relationship to the energy levels of the sample.

3.2.2 In situ XPS and UPS

For the temperature dependent XPS measurements, the donor film was first cooled to -100 °C before deposition of C_{60} and left to heat up to room temperature while spectra were continually collected. This process involved the use of a cold stage in the thermal evaporation chamber and a cold stage in the analysis chamber.

When probing intermixing, the C_{60} overlayer was deposited in a stepwise manner. After each C_{60} deposition cycle, the sample was transferred from the MBE to the analysis chamber where XPS and UPS were performed sequentially. The C_{60} deposition, XPS and UPS measurements sequence were repeated until no further decay or shifts were observed in the spectra.

3.3 Device fabrication, testing and optoelectronic measurements

3.3.1 Sample transfer (vacuum suitcase)

Thin film transfer from the UHV system to the glove box was done via a vacuum suitcase, which prevents exposure of the devices or thin films to air (Figure 3.5). The bakeable vacuum suitcase provides high vacuum conditions thanks to a pumping system to which it is coupled allowing the evacuation of the vacuum suitcase before transfer from the glove box to the UHV, further minimizing chances of oxidation during the otherwise lengthy transfers. The vacuum suitcase sample holder assembly can accommodate up to four samples. This feature allowed for the simultaneous fabrication of up to four devices in the MBE chamber followed by a batch transfer to the glove box.

3.3.2 Device fabrication

3.3.2.1 Substrates preparation

Substrates selection: The selection was based on substrates transparency, roughness, and conductivity. Films prepared for X-rays spectroscopy were grown on gold foil because gold is inert and highly conductive. For optical measurements, bare glass substrates or quartz were used. For X-ray diffraction studies quartz was preferred for its flatness. However, silicon substrates with a top oxide layer of few hundreds nanometer thick were used occasionally.

Substrates cleaning: Gold substrates were cleaned in-situ using bombardment with a collimated argon ion beam (partial pressure of 5×10^{-6} mbar) for 15 minutes. Survey analysis with XPS was then used to confirm the surface cleanliness. ITO (Indium Tin Oxide), glass, Quartz, and SiO2/Si were cleaned by immersing the substrates in an ultrasonic bath, made of a dilute sodium dodecyl sulfate solution, for 15 minutes, fol-

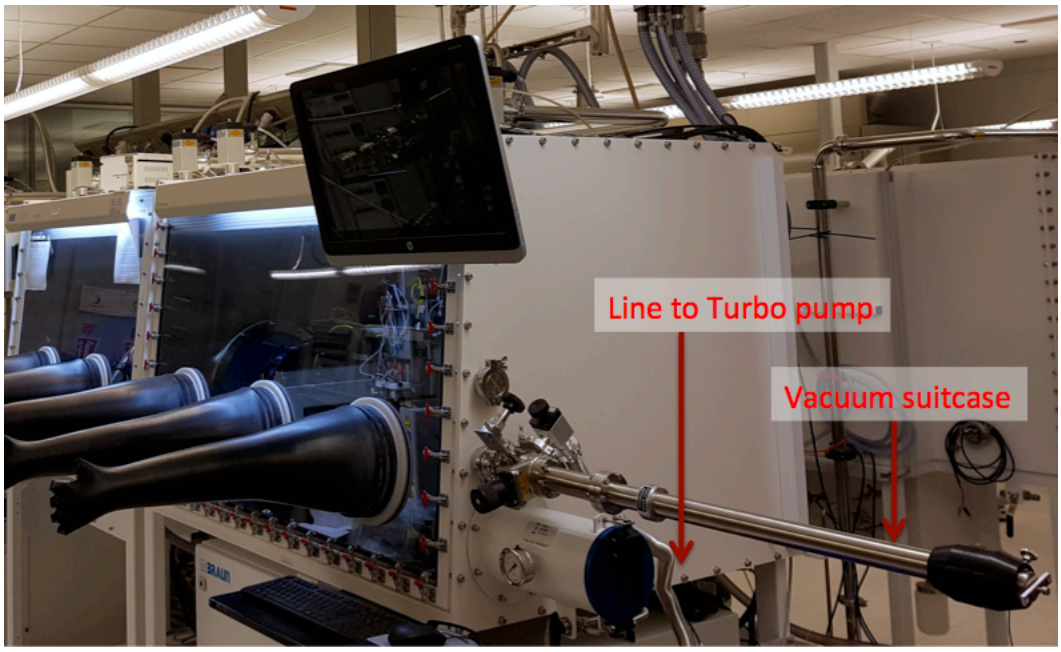

Figure 3.5: Bakeable vacuum suitcase attached to a nitrogen glove box and equipped with an evacuation line connected to a turbo pump. The suitcase contains a sample cassette, and allows samples to be transferred from the glove box the UHV chamber without air exposure.

lowed by several rinses and sonication in deionized water for 5 minutes. Cleaning then proceeded with polar solvents by sequential sonication in acetone and isopropanol for 15 minutes each. The substrates were then blow-dried with nitrogen gas and exposed to UV generated ozone for 12 minutes.

Substrate surface energy control: Surface energy control was used to control film growth. In specific, a templating approach was utilized whereby an ultrathin Copper Iodide (CuI) layer was coated on the substrate before film growth. The CuI was evaporated from a thermal evaporator onto pre-cleaned substrates and when necessary transferred to the UHV chamber via a specially designed vacuum suitcase (Figure 3.5) equipped with a turbomolecular pump for the deposition of organic films.

3.3.2.2 Device fabrication

Pre-cleaned substrates were transferred into nitrogen filled glovebox for the device fabrication. The devices were fabricated where in an Angstrom thermal evaporator (Evovac, Angstrom Engineering systems), (Figure 3.6) integrated into a glove box. The chamber features six Resistive sources for metal evaporation and interlayers, four Thermal (RADAK) sources for small organic molecules deposition, source shutters and a gradient and stepping substrate shutter. The sources are arranged into clusters assigned to metal, interlayers and organic layers deposition, each equipped with a QCM deposition rate sensor. The substrate stage can be both resistively heated (max temp 150 °C) and LN2 cooled down to -100°C.

Figure 3.6: Angstrom evaporator and solar simulator housed in an Mbraun nitrogen gas filled glovebox.

3.3.2.3 Device testing

The solar cells were tested under one sun condition using simulated solar radiation generated by a solar simulator housed outside a glove box. The light beam was coupled into the box through a quartz window. The solar simulator (ABET technologies, Class AAA) is based on 300W Xenon arc source. The filtered light has a 99% spectral match to the AM1.5 spectrum and about a 90% match over the bandwidth of a typical organic cell. The lamp calibration was done with a KG5 filtered Si diode.

Important solar cell parameters Jsc, Voc, and FF can be obtained from basic current voltage scans (J-V curves). The extraction of such parameters is based on various electrical models and equivalent circuits. An idealized electrical model consist of electrical components including in series, a light-induced source (I_L), Series resistance (R_S) and in parallel a diode characterized by saturation current (Is) and an ideality factor ($n = 1$) and a shunt resistance (R_{SH}). In high-performing solar cells, the series resistance is vanishingly small while the shunt resistance is extremely large (In the order of Gigaohms/cm^2). A schematic of such an equivalent circuit is presented in Figure 3.7.

The current flowing through the circuit when there is no load is given by Equation 3.12.

$$I = I_S(e^{\frac{qV}{kT}} - 1) - I_L \tag{3.12}$$

Where, I_S is the diode saturation current and I_L is the photocurrent. For the sake of simplicity, we will limit our discussion only to the idealized equivalent circuit of an organic solar cell. All devices were fabricated in the standard configuration with the convention that the cathode (Aluminum) is the electron-collecting electrode, the anode (ITO) is the hole-collecting electrode and positive current flows from the cathode

to the anode. At equilibrium (no applied bias) Fermi levels of the individual materials are aligned and because of the work function difference between the electrodes, the HOMO and LUMO levels of the donor are skewed. Under forward bias (electron injection at the cathode), in the dark, the electron injection barrier (EIB) needs to be overcome before electron can be injected allowing a current to flow. In the reverse bias, very low amount of current can flow through the device. Under illumination, in forward bias, the photocurrent (positive) and the dark current (negative) are in competition. As the voltage is increased, more and more dark current is generated until dark current exactly compensates the photocurrent and at this point, no net current flows through the device. The voltage at which this occurs is the open circuit voltage. In reverse bias, since the dark current is extremely small, almost all the current originates from the photocurrent. In a good solar cell, no dependence of the current on the voltage should be observed in this regime. A voltage dependence of the current in this regime often indicates non-geminate recombination, as carriers need an extra push from the field to get out of the device.

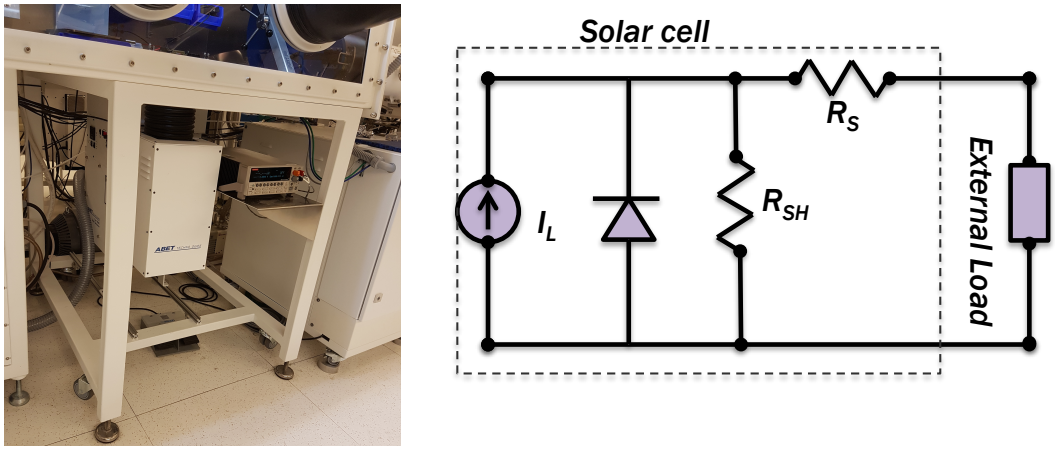

Figure 3.7: (Left) An ABET AM1.5 solar simulator connected to nitrogen glove box. **(Right)** Electrical model of an organic solar cell.

3.3.2.4 Device parameters

Device parameters such as Jsc, FF and Voc are obtained from J-V curves. JV-curves measurements were done with the aid of commercial software (TracerII, Rera systems) with also provided control over a source meter (Keithley 2400). Before each set of measurements the solar simulator irradiance as calibrated using a silicon Calibrated Reference Cell (ABET, Model 15150). Both forward bias and reverse bias measurements were performed. During the measurements the voltage applied to the cell is swept from negative to positive values (often above Voc) and the current is collected at each voltage increment. Settling time between 10^{-3} s and 10^{-1}s were applied and light and dark measurements respectively. Jsc, FF, and Voc were automatically derived at the end of the measurement by internal software procedures. The cell area was 0.1 cm^2. For each substrate (Figure 3.7), ten devices were tested, and the reported device parameters values were based on at least 20 devices. The series resistance was determined as the inverse of the slope of the J-V curve in the far-forward region of the characteristics where the logarithm of the curve is linear. The shunt resistance was determined as the inverse slope of the J-V curves in the linear portion of this curve in reverse bias.

3.3.3 Sensitive External Quantum Efficiency (EQE) and Photothermal Deflection Spectroscopy (PDS): Set up, measurements and other considerations

To measure the interfacial charge transfer state, we use a very sensitive probe capable of detecting weak subgap absorption events relation to optical transitions at the donor-acceptor interface by CT states complexes. One way to detect these absorption events is to measure changes in refractive index, due to the heat wave generated upon light absorption by CT states, of a liquid in thermal equilibrium with the organic film being probed. Another way is to, detect the current originating from dissociation of

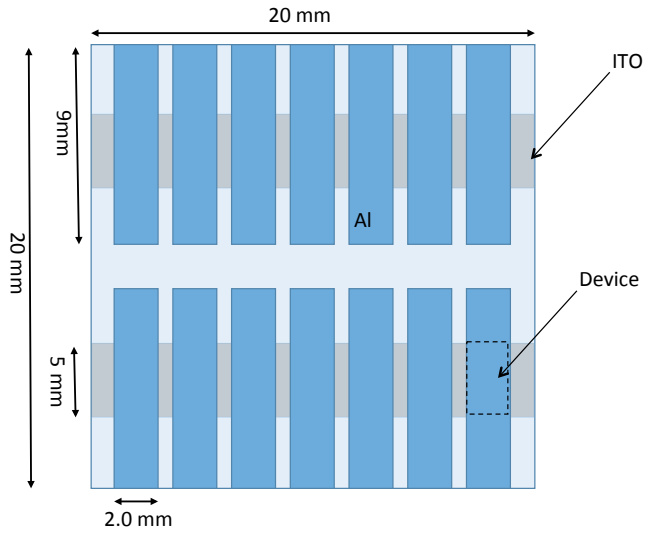

Figure 3.8: Device layout on a patterned ITO substrates showing ITO strips, metal electrodes patterns. The light blue area represents the active layer.

CT excitons generated by direct interfacial light absorption by the solar cell. We first discuss the latter technique then the former.

3.3.3.1 Spectrally resolved sensitive external quantum efficiency measurements

White light is sent from a xenon source (Newport 300W ozone free xenon arc lamp) and input into a monochromator and transported to the sample mounted on the stage in nitrogen filled glove box. Between the sample and the light source, is placed an optic assembly composed filters mounted on a filter wheel, a diaphragm to control the size of the light spot and focusing lense. The light beam is chopped using, an optical chopper (Stanford Research Systems SR540 optical chopper), and a lock-in amplifier (Stanford Research Systems SR830 lock-in amplifier) are used to improve signal-to- noise. The apparatus is semi-automated using Labview visual instruments to control the monochromator (Oriel Cornerstone 260 1/4m monochromatic) and a

lock-in amplifier (Figure 3.9). The monochromatic light intensity was calibrated with Ge and Si photodiodes. The subgap region of the collected EQE spectra is fitted to Equation 3.13.[180]

$$EQE_{PV} = \frac{1}{E\sqrt{4\pi\lambda kT}} \exp \frac{-(E_{CT} - \lambda - E)^2}{4kT} \tag{3.13}$$

Where λ is, the reorganization energy and f is a term proportional to the number of CT states and the square of the electronic coupling element. E_{CT} is the energy of the charge transfer state. The parameters E_{CT}, λ, and f are extracted from a sensitive EQE measurement by a Gaussian fit of the CT absorption portion of the spectrum.

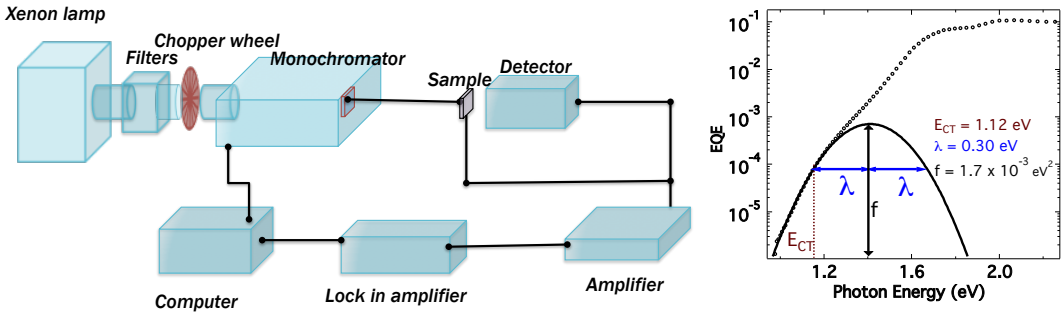

Figure 3.9: Schematic of the set up use for above and below gap EQE measurements. Spectrally resolved EQE signal (dotted line) signal plotted on a log-linear scale to make the signal origination from CT states absorption in the below region on the x-scale more pronounced. The parameters E_{CT}, λ, and f are shown in relationship with the fit (Solid line).

3.3.3.2 Photothermal deflection spectroscopy (PDS)

One limitation of the subgap sensitive EQE is that the signal is scaled with the internal quantum efficiency of the dissociation of the CT states generated by direct interfacial excitation. For this reason, Photothermal Deflection Spectroscopy (PDS) is used to determine the real CT state absorption. Since CT states have very weak oscillator strength, the absorption event in PDS is not detected with the conventional

approach whereby a single light beam that excites the sample is detected after the absorption event. Instead in PDS, two light beams are exploited; the excitation beam, a chopped monochromatic light beam, chosen such as to excite the subgap CT states, first illuminates the sample. The periodic absorption events (light is chopped) inevitably result in a periodic fluctuation of the sample temperature. The sample equilibrates with surrounding liquid in which it is immersed through heat waves that cause a fluctuation in the refractive index of the liquid. The second beam, often a HeNe laser light, is then sent a grazing incidence on the surface of the liquid to detect these changes in refraction index of the liquid. A position sensitive detector is used to detect the deflection of the laser beam from the change in the liquid refractive index and sample absorption coefficient are derived.[181, 182]

3.3.3.3 Above gap EQE

The spectral response of the solar cells was measured by illuminated the cell with monochromatic light and recording the current generate as a function of the wavelength of the light. The quantum efficiency at each wavelength was calculated by taking the ratio of this current to the current produced by a calibration photodiode correct to its responsitivity. From the EQE spectra, the photocurrent was predicted and compared to the actual Jsc. Agreement of these two values was found with about 10 % accuracy.

3.3.4 Electroluminescence (EL)

Because CT emission is very weak in organic solar cells, it is often hard to extract the CT emission buried in the the emission coming from the band tails of the pure phase of materials. In EL, since the injection charge carriers in the donor and acceptor layer populate CT states, leaves recombination at the interface as the only possibility for encounters under appropriate biasing. At low forward voltages and low injection

currents, injected charges will remain in the layer in which they were injected (in the donor or the acceptor) and recombination in the pure phase of the donor or the acceptor will be limited. I have measured EL on rubrene bilayers with the structure Device structure: Glass/ITO/PEDOT:PSS/50 nm rubrene/50nmC_{60}/12nm Bphen/ 110nm Al. The device was biased using a Keithley 2400 and kept in a custom-built nitrogen chamber equipped with pins for electrical connections. A cooled CCD camera was used as the detector.

3.4 Materials characterization

3.4.1 Grazing incidence wide angle x-ray scattering (GIWAXS)

To investigate near-surface and bulk crystallinity, and molecular packing of the thin films, grazing incidence wide angle x-ray scattering (GIWAXS) measurements were performed using x-ray synchrotron radiation at the Cornell High Energy Synchrotron Source (CHESS) and the Stanford Synchrotron Radiation Lightsource (SSRL). The need for both CHESS and SSRL was due to scheduling reasons. X-rays with a wavelength of 1.15 Å (10.78 keV) was used (CHESS) which is in the typical range of wavelength used for organic samples. The diffraction patterns were recorded using a highly sensitive Pilatus 200 K area detector (Rigaku) with a pixel size of 172 m. The x-ray incidence angle with respect to the sample surface was varied from 0.12° to 0.5° with 5 intermediate points in between and the sample to detector distance was in the range of 100 to 200 mm. At SSRL, we used similar conditions but utilizing photon of wavelength 0.976 Å (12.703 keV), a MAR345 image plate area detector and a 400 mm sample to detector distance. In addition the sample chamber was helium-filled. The advantage of synchrotron radiation is the high photon flux allowing little sample exposure, and yet good data statistics, and the collection of two-dimensional diffraction patterns, which are made possible by the use of areal detectors. At very low incidence angle (0.1 - 0.2°) and below the film critical angle (Equation 3.14) of refrac-

tion, information about crystalline structures in the near-surface region of the active layer can be gained. Above the critical angle, the entire film is probed.

$$\alpha_c = \sqrt{2\delta} \tag{3.14}$$

where δ is $1-n$, n being the samples index of refraction. [183] GIWAXS is a hard X-rays, two-dimensional based structural characterization technique used to gain quantitative information about the size, shape, orientation, and disorder of crystallites. GIWAXS may be applied to both solid and fluids. The scattering pattern is generated by placing a sample in the path of a X-rays at a grazing angle, typically <0.2°, and detecting the scattered light using a two-dimensional detector often oriented in the plane normal to substrate surface. The scattering pattern consists of Bragg reflections whose shape and position reveal a reciprocal space from which the real space symmetry of the crystallites and crystallographic parameters can be deduced. The intensity of the peaks contains quantitative information about the volume of the crystalline portion of the sample (Figure 3.10). GIWAXS is also used to determine the orientation of crystallites with respect to the substrate. In ZnPc/C_{60} bilayers, in addition to determining molecular orientation (Figure 3.10), it was possible to correlate the scattering profiles of specific lattice planes with the degree of interfacial mixing. In donor-acceptor blends GIWAXS was used to study the evolution of donor or acceptor degree of aggregation with composition.

For elastic scattering, i.e., when conservation of momentum transfer holds, and for an in plane geometry, the following widely used conventions apply. if $\overrightarrow{k_i}$ and $\overrightarrow{k_o}$ are the incident and the diffracted wave vectors then, $|\overrightarrow{k_i}| = |\overrightarrow{k_o}| = \frac{2\pi}{\lambda}$, 2θ denotes the oblique angle between $\overrightarrow{k_i}$, $\overrightarrow{k_o}$ (Figure 3.11). Based on the conservation of momentum, the total momentum transfer is given by Equation 3.15.

$$\overrightarrow{q} = \overrightarrow{k_o} - \overrightarrow{k_i} = \frac{4\pi}{\lambda}\sin(\theta) \tag{3.15}$$

The coordinate of the momentum transfer q is given by Equation 3.16.

$$\begin{aligned} q_x &= k_o \cos(2\theta) \cos\alpha_o + k_i \cos\alpha_i \\ q_y &= k_o \sin(2\theta) \cos\alpha_o \\ q_z &= k_o \sin\alpha_o + k_i \sin\alpha_i \end{aligned} \tag{3.16}$$

Where, q_x is in-plane wave vector transfer component in the scattering plane, q_y is the in-plane wave vector transfer component normal to the scattering plane and q_z is the wave vector transfer component normal to the surface.

The total in-plane wave vector transfer is given by Equation 3.17.

$$q_r = \sqrt{q_x^2 + q_y^2} \tag{3.17}$$

3.4.1.1 Data analysis

2D-powder patterns were converted into one dimensional patterns (q or 2θ versus intensity using the well known program Fit2D.[184] The software was used to apply a polarization correction, the detector geometry distortion correction and other geometric corrections to the raw data. Sample related corrections such as sample absorbance, beam divergence and energy dispersion, footprint of the illuminated sample area and refraction correction, which is usually negligible in GIWAXS. These corrections are supposed to be negligible in the case of organic thin films.

3.4.2 Atomic Force Microscopy (AFM)

A high precision Agilent 5400 SPM/Atomic Force Microscope (AFM) housed in an isolation chamber was used to measure the surface topography of the thin films. A silicon pyramid-shaped probe was used to raster-scans the film surface at the micron scale. The topography was essentially used to determine the surface roughness.

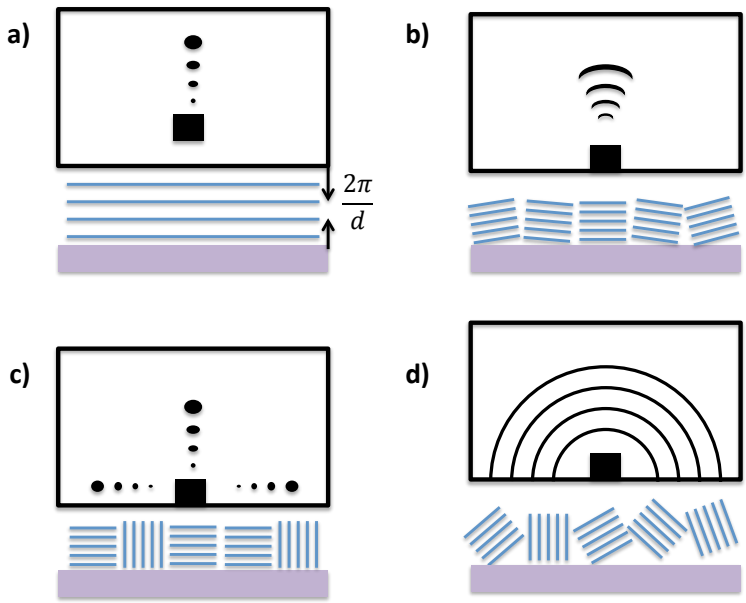

Figure 3.10: Illustration of hypothetical film crystallinity relevant for organic semiconductors. The colored sketches show crystallographic planes (not molecules) and corresponding 2D GIWAXS patterns. a) Perfectly oriented crystal with horizontally oriented lattice planes giving rising very sharp Bragg peaks in the vertical direction b) Oriented crystallites with quasi-horizontal lattice planes. The diffraction pattern is made crescent in the vertical direction c) oriented crystallites with vertical and horizontal orientations. The diffraction pattern consist of Bragg peaks appearing in both the vertical and horizontal direction d) Randomly oriented crystallites (2D powder). The diffraction pattern consists of diffraction rings. Illustrations adapted from [183].

3.4.3 Transmission Electron Microscopy (TEM)

Complementarily to X-rays scattering, we probe real space thin morphology at the nanometer level using high-resolution transmission electron microscopy (TEM). TEM has an advantage over X-rays because, with TEM, one probes with an electron beam, which can be focused down to several angstroms thus, providing very precise and local morphological information. Selected area diffraction (SAD) information at similar length scales, which reveals in addition to morphology the local crystalline structure of the material. TEM analysis of the organic films was done using a transmission electron microscope operating at 300 kV (Titan Cryo Twin, FEI Company, Hillsboro,

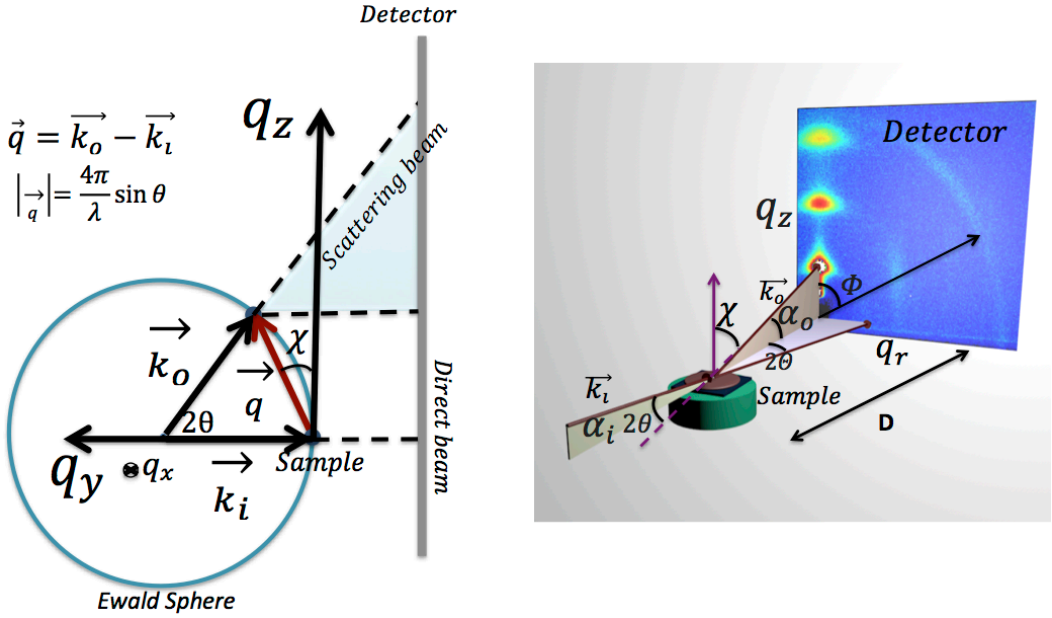

Figure 3.11: Schematic picture of the experimental set-up used in GIWAXS showed in projection with the Ewald sphere **(Left)** and in three dimensions **(Right)**. The scattering X-rays are detected with a 2D detector oriented vertically and placed a distance D from the sample. χ is the angle between the qz direction and q in the reciprocal space. α_i and α_f are the incident and exit angles. 2Θ is the in-plane scattering angle and Φ is the polar angle on the detector plane with respect to the direct beam.

OR) to acquire plan-view micrographs SAD patterns. Samples were prepared by lifting the films through overnight immersion in de-ionized water. The floating film flakes were then transferred onto a copper grid and dried under vacuum for few hours before experimentation. The SAD diffraction patterns were indexed using the online simulation tool Web Electron Microscopy Applications Software (WebEMAPS).[185]

3.4.4 Ultraviolet-visible spectroscopy (UV-Vis)

Absorption spectra were acquired with a Cary 5000 (Varian) spectrophotometer on films prepared on quartz substrates. The spectrophotometer was equipped with an integrating sphere attachment capable of measuring the spectral characteristics from approximately 300 to 2500 nm. A double beam was used to minimize noise. Spectra

were collected in transmission and reflection modes and corrected for background.

3.5 Material systems

We selected low molecular weight, vacuum-processable conjugated small molecules as materials for the active layer. Vacuum processable small molecules have the advantage of being amenable to a high degree of film growth control and purity when processed under ultra-high vacuum (UHV) conditions. UHV is of particular importance because it enables in-situ studies on freshly grown films to be conducted without air exposure, allowing elimination of possible sample contamination or materials oxidation. We selected a subset of small molecules based on their degree of crystallinity, their ability to be crystallized or templated to a given molecular packing /molecular orientation, and their polarity and polarizability. Other considerations included commercial availability and degree of purity.

3.5.0.1 Small molecule acceptor

We selected fullerene-C_{60} (Molecular structure in Figure 3.12) as the acceptor material for the entire work. Fullerene-C_{60} is available in extremely high purity and can be processed in vacuum. In addition, fullerene-C_{60} exhibits a remarkable molecular symmetry. Because of its spherical symmetry, we concerned ourselves not with the acceptors molecular orientation, thus simplifying structural complexity at the donor-acceptor interface. Finally, because it is a widely used acceptor, studies based on OPV systems with fullerene-C_{60} as an acceptor find a much broader scientific interest.

3.5.0.2 Small molecule donors

Donor molecules (Molecular structures shown in Figure 3.12) are selected according to their crystallinity, ability to be crystallized in thin-films and their polarity or polarizability. The following materials were used in the study:

- Zinc Phthalocyanine (ZnPc)
- Sexithiophene (6T)
- benzannulated boron dipyrromethene (bDIP).
- N,N-Bis(naphthalen-1-yl)-N,N-bis(phenyl)benzidine (NPD)
- 5,6,11,12-Tetraphenylnaphthacene (Rubrene)

3.5.0.3 Crystallinity of the materials

Crystalline donors: To investigate the role of donor molecular packing on interfacial energetics and charge separation at the D-A interface, we use ZnPc as a donor. ZnPc forms highly crystalline and textured films as deposited. Moreover, through substrate surface modification, the thin film texture can be altered. The impact of donor degree of order on D-A interfacial properties was equally assessed. Therefore, we choose donor molecules, which in addition to exhibiting long-range order in thin films also exhibit a high polarization energy. For this purpose, we use 6T and bDIP. They all form highly crystalline and textured films. Rubrene, an amorphous small molecule that also forms highly crystalline films upon annealing was used to compliment the above-listed molecules because of its tunable degree of crystallinity and high CT state oscillator strength.

Amorphous donors: In the series on of donor-acceptor interfaces we aim at recreating, donor-acceptor interfaces formed with a disordered donor are equally of interest.

To create such interfaces, we use NPD and rubrene, two conjugated organic small molecules that form amorphous thin films as deposited.

3.5.0.4 Polarity and polarizability of the materials

Interactions between neighboring donor and acceptor molecules surely play a major role in determining the interfacial energetics. However, interactions of the molecules with their surrounding in the pure phase equally plays a critical role. Energy levels are significantly shifted in going from isolated molecules in the gas phase to densely arranged molecules in the solid state. This characteristic is determined by materials polarity and polarizability. Thus the donor materials were chosen to cover a range of polarity and polarizabilities. In Table 3.2 we show the dipole moments and polarization energies of the materials used in this study.

Table 3.2: Structure and properties of small molecules investigated in this thesis.

Materials	**Thin-film crystallinity** [2]	**Crystal structure** [3]	**Polar?**	**PE** [4](eV)
ZnPc	Polycrystalline	Triclinic (P1)	No	1.1 [186]
Rubrene	Amorphous	Orthorhombic(C ma)/monoclinic (P 21/c)/triclinic(P1)	No	1.1 [187]
6T	Polycrystalline	Monoclinic (P 21/c)	Yes	2
NPD	Amorphous	-	No	1.4
bDIP	Polycrystalline	-	Yes	-
C_{60}	Polycrystalline	Cubic (P a 3)	No	1.2

3.5.0.5 Materials source and purity

All materials were purchased in their purest possible grade (>99.5%). bDIP was synthesized in the Thompson group at the University of Southern California based on a previous report from the Ono group,[187] and sublimed twice before use. All

[4]As deposited
[4]Single crystal
[4]Polarization Energy

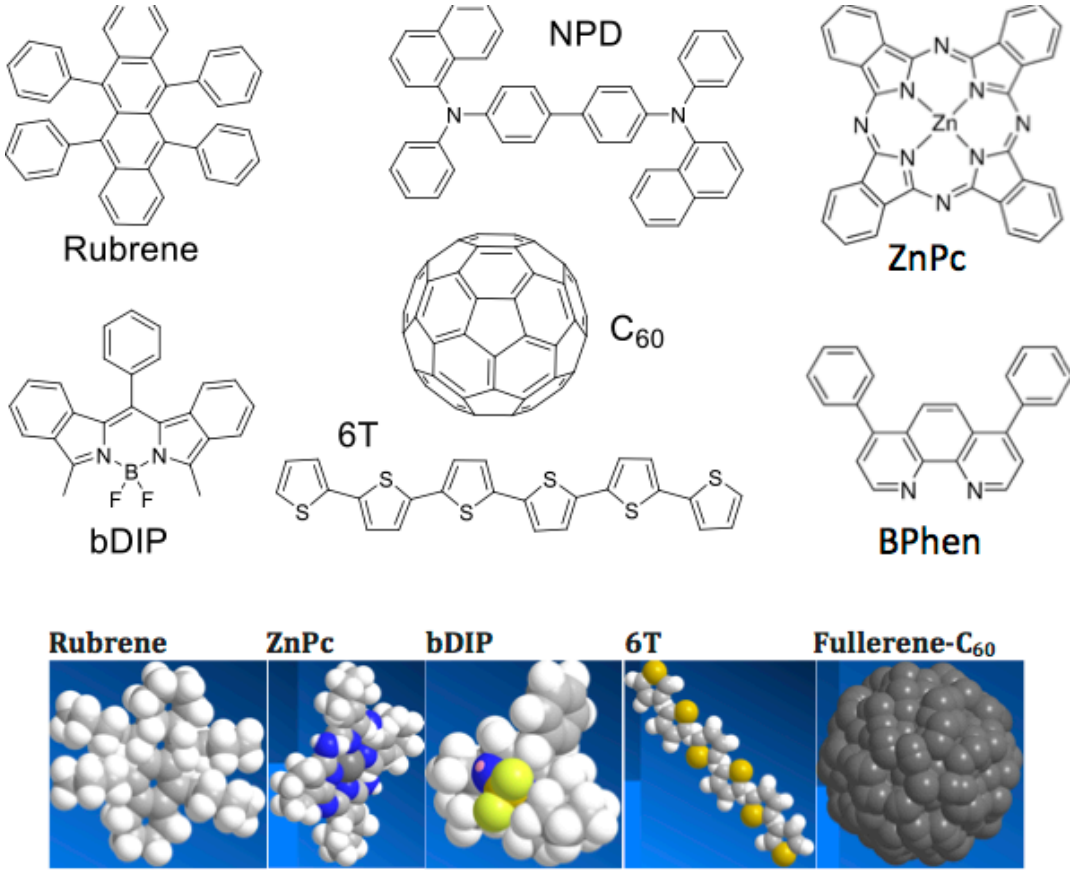

Figure 3.12: Chemical structures and three dimensional spacefill models of the donor molecules and the acceptor C_{60} molecule used in this study. BPhen, the molecule used as the hole-blocking layer is also shown.

materials were further purified in the UHV-MBE chamber by baking the evaporation source containing the materials overnight at 95 to 120 °C. To further purify the materials, a small fraction of the crucible content was discarded by heating the source at a temperature high enough to sublime low melting point impurities before the first film deposition. Rubrene, NPD, 6T, and C_{60} were purchased from Sigma-Aldrich Co. ZnPc was purchased from Jilin OLED Material Tech Co.

3.5.1 Engineering order at donor-acceptor Interfaces and blends

3.5.1.1 Controlling interfacial molecular conformation

Planar interfaces: Planar interfaces form in bilayer stacks when there is no considerable mixing at the interface. In bilayers the advantage of a donor-acceptor interface, which is spatially confined, allows one to perform controlled in-situ interfacial studies. This is possible because the bilayer stack is grown sequentially, and in the absence of mixing, the structural order of both the donor and the acceptor as assumed in pure thin films is maintained in the stack. This also implies that the structural order in the donor layer and the acceptor layer can be tuned independently enabling fabrication of interfaces with controlled molecular confirmation (Figure 3.13B, C & D).

3.5.1.2 Controlling interfacial mixing

As discussed later in Chapter 4 interfacial mixing may occur spontaneously in the presence of certain donor conformation. We utilize a specialized feature of our MBE manipulator, which allows deposition under cryogenic conditions; we can also tune the degree of interfacial mixing.

3.5.1.3 Controlling the degree of crystallinity of the donor and the acceptor

Dilute blends: To create model systems in which the extent of donor or acceptor aggregation is minimized, dilute donor-acceptor blends were utilized. Dilute blends are blends made of a donor in a matrix of the acceptor or vice versa. In the dilute blends with an otherwise crystalline solute, the solute is expected to aggregate less since its molecules would be sparse because of the high donor loading. The situation is reversed in dilute blends of the acceptor in a donor matrix (Figure 3.13F & G).

These blends are made using the ability that the MBE chamber gives us, precisely, to deposit the donor and the acceptor simultaneously and to control each materials deposition independently.

Blends with high content of donor or acceptor: At a comparable degree of loading of both donor and acceptor in the blend, we expect to replicate conditions close to most BHJs. Such systems may feature a combination of mixed phases, aggregated or non-aggregated pure phases in various proportions (Figure 3.13E & H).

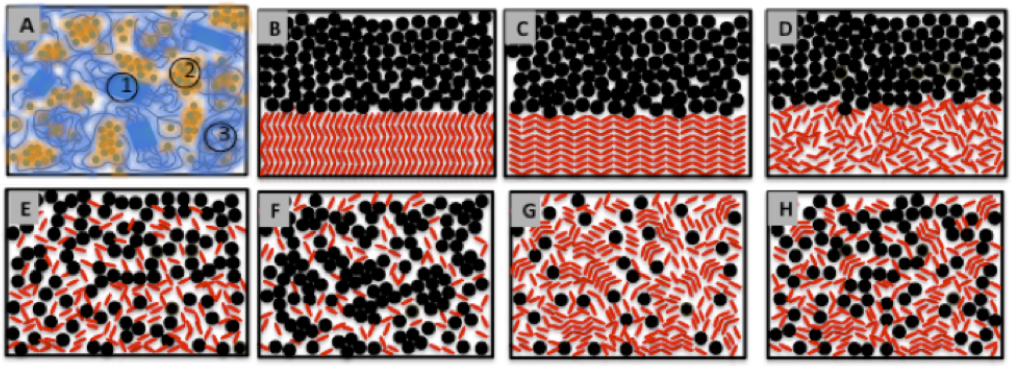

Figure 3.13: (A): BHJ active layer featuring aggregated polymer phases (1) aggregated fullerene phases (2) mixed phases (3) and interfaces between these phases. (B, C & D): Models systems that emulate the BHJ in (A) through small molecules bilayers structures with an ordered and oriented donor (B, C) and a disordered donor (D). (E, F, G) A small molecule blends with completely disordered blend, a blend with a diluted donor content, and a diluted acceptor content. (H) A blend with a comparable amount of donor and acceptor as in (A) representing the standard small molecules BHJ with interfaces at phases boundaries with phases of various degrees of order and which can be understood in terms of a complex arrangement the simpler interfaces found in (B, C, D, E, F & G).

Chapter 4

Impact of Molecular Orientation and Spontaneous Interfacial Mixing on the Performance of Organic Solar Cells

4.1 Introduction

In this chapter, we investigate the impact of donor molecular packing on charge separation at the D-A interface. We also discuss how molecular packing influences exciton diffusion and free carriers recombination. As discussed in previous chapters, it is exceedingly difficult to probe the molecular orientation in bulk heterojunctions because have many interfaces, and they are arranged with varying angles with respect to the substrate. One of the best ways to study the interface is to make bilayer solar cells with just one donor-acceptor (D-A) interface. Zinc phthalocyanine (ZnPc) is particularly interesting to study because it forms highly crystalline thin films with edge-on molecular orientation. Moreover, the film molecular orientation can be adjusted by using a 2-nm-thick copper iodide seed layer to template film growth. Previous studies have claimed that solar cells in which fullerene acceptor molecules touch the face of ZnPc have more current than the ones in which the fullerenes touch the edge of ZnPc (Figure 4.1) because of suppressed recombination. Although this may be true, it is not entirely certain that orientation alone is the factor leading to suppressed recombination.[121] For instance, recent computational studies of small-molecule interfaces indicate that the molecular orientation of D molecules with respect to fullerene A molecules can determine the degree of molecular mixing and disorder at the D-A interface, pointing to miscibility behaviors between D and

A which are dependent on the structural order in D.[50, 188] As a matter of fact, the lack of a precise knowledge of the exact structural configuration at the D-A interface would lead to difficulties in building accurate predictive models and interpretation of device data. Therefore, it appears necessary to pinpoint the precise role of molecular packing that one first needs to characterize D-A interfaces in OPVs with much more care.

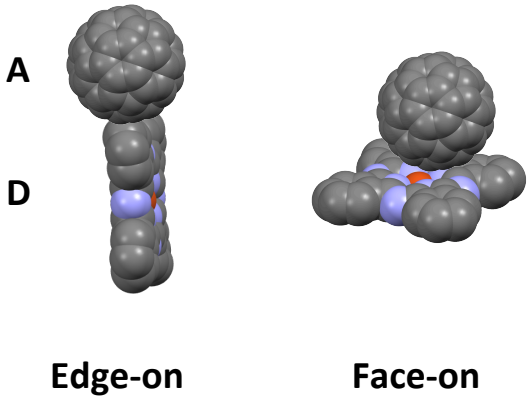

Figure 4.1: Hypothetical molecular conformations at the D-A interface in ZnPc/C_{60} bilayers

We have more thoroughly characterized the system using in situ x-ray photoelectron spectroscopy and x-ray scattering and found that the interfaces are not as sharp as previous studies claimed when formed at room temperature or above. Fullerenes have a much stronger tendency to mix into the face-on films than into the edge-on films. Moreover, we show that almost all of the increase in the current with face-on films can be attributed to improved exciton diffusion and the formation of a spontaneously mixed interface, not suppressed recombination.

4.2 Miscibility at the D-A interface in edge-on and face-on ZnPc/C_{60} bilayer films

We now wish to investigate the impact of molecular packing on the miscibility of ZnPc and C_{60} right at the D-A interface. We first characterize molecular packing in pure ZnPc films and subsequently we investigate interfacial mixing using ZnPc/C_{60} bilayers.

4.2.1 Characterization the molecular packing of the pure ZnPc thin films

The molecular packing texture was modified from predominantly edge-on texture on ITO/SiO2 to face-on texture by pre-coating the substrate with a 2 nm templating layer of copper iodide (CuI).[120, 189–192] The seed CuI layer essentially modifies the substrate surface energy in a way that favors the growth of the ZnPc film with a face-on packing. However, the exact details of the templating mechanism remain unclear. It is important to fully characterize the pure ZnPc films before proceeding to the characterization of the bilayers. Two-dimensional grazing incidence wide-angle x-ray scattering (GIWAXS) was used the main structural characterization technique. In Figure 4.2, we present the two-dimensional grazing incidence wide-angle x-ray scattering (GIWAXS) data and corresponding integrated intensities in the horizontal (in-plane) and vertical (out-of-plane) directions, which we use to determine the crystalline texture and the stacking orientation of ZnPc in thin films.[114, 189, 192] ZnPc films are known to form both and polymorphs (Figure 4.3) on non- interacting substrates at room temperature. Both phases are monoclinic with lattice parameters a=25.92 Å, b=3.79 Å and c=23.92 Å (γ phase or also (α phase) and a=19.41 Å , b=4.79 β and c=14.63 Å (β phase).[193]
The ZnPc/ITO film exhibits scattering peaks at 4.95 nm^{-1} in the vertical direction and at 5.11 nm^{-1} and 18.52 nm^{-1} in the horizontal direction (Figure 4.4a),

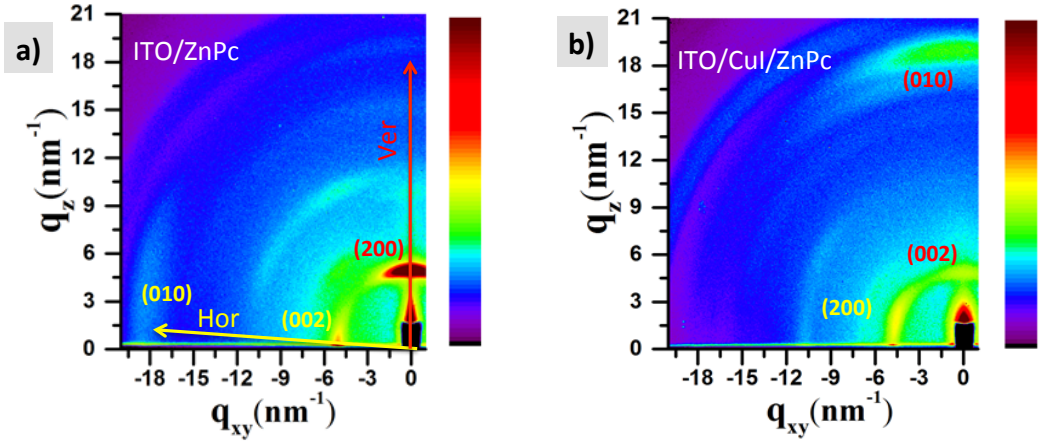

Figure 4.2: 2D GIWAXS patterns of 20 nm-thick ZnPc films grown on ITO/glass (a) and on 2nm CuI-coated ITO/glass (b) substrates. Qxy and Qz refer to the in-plane and out-of-plane components of the scattering vector respectively.

corresponding respectively to d_{200}=1.27 nm, d_{002}=1.23 nm and d_{010}=0.34 nm of the phase of ZnPc with the (002) plane parallel to the substrate, indicative of the edge-on stacking texture. By contrast, the ZnPc/CuI/ITO films exhibit scattering peaks at 4.91 nm^{-1} and 18.96 nm^{-1} in the vertical direction and 4.76 nm^{-1} in the horizontal direction (Figure 4.4b), corresponding respectively to d_{002}=1.28 nm, d_{010}=0.33 nm and d_{200}=1.32 nm of the phase of ZnPc with the (010) plane parallel to the substrate, indicative of the face-on stacking texture. The (010) peak corresponds to scattering along the $\pi - \pi^{\star}$ stacking direction, and clearly orients itself parallel to the substrate plane in edge-on stacked molecules and perpendicular to the substrate plane in face-on stacked molecules. We found these results to be consistent with what has been reported previously. [114, 189]

4.2.2 Characterization of the D-A interface in ZnPc/C_{60} bi-layers

We first utilize photoelectron spectroscopy to monitor the attenuation of the ZnPc signal during stepwise deposition of C_{60} on top of the pristine ZnPc films. X-ray

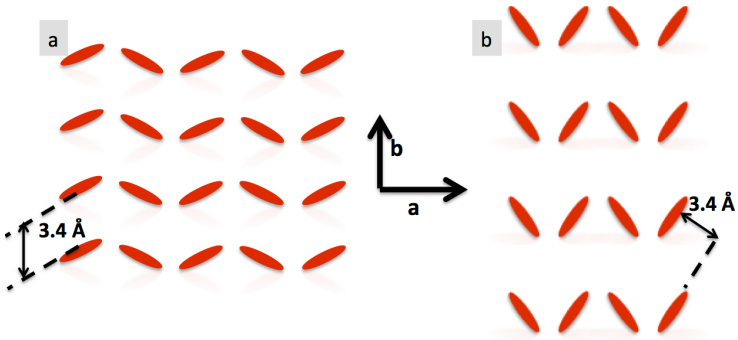

Figure 4.3: Schematic showing the herringbone columnar packing of the α-phase (left) and the β-phase (right) of ZnPc.

photoelectron spectroscopy (XPS) and ultraviolet photoelectron spectroscopy (UPS) are non-invasive and do not induce further intermixing, as sputtering based depth-profiling techniques such as secondary ion mass spectrometry may. In UPS and XPS the escape probability of photoelectrons decreases exponentially with the sampling depth as discussed in Chapter 3. This feature can be used to probe intermolecular mixing at the interface between two layers. In the case of a non-mixing, discrete interface, the signal from the underlayer follows a rapid exponential decay as it gets buried, with typical inelastic mean free paths of ca. 1 nm in UPS and ca. 3 nm in XPS. [194, 195] If mixing occurs, the rate of attenuation from the underlayer will decrease as ZnPc mixes with the top C_{60} layer. We perform stepwise deposition of C_{60} on top of a pristine ZnPc film at room temperature (RT) while monitoring the nitrogen core electron N1s signal (XPS) or the ZnPc HOMO peak (UPS) area (Figure 4.5). The observed trends in the decay rates reveal a slower decrease in the case of face-on ZnPc as opposed to edge-on ZnPc. These differences in attenuation rates most likely indicate more interfacial molecular mixing taking place in the case of face-on ZnPc on ITO/CuI than in the case of edge-on ZnPc on ITO.

Since differences in film morphology and surface coverage would invalidate the in situ XPS and UPS conclusions, atomic force microscopy (AFM) was performed on

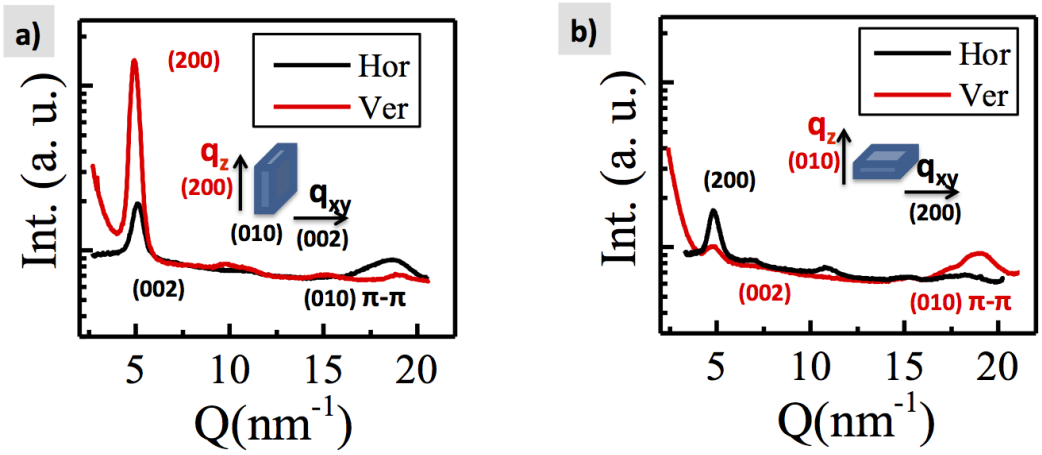

Figure 4.4: Integration plots of images in Figure 4.1 in the horizontal (black) and vertical (red) directions of the ZnPc films grown on ITO/glass (a) and on 2nm CuI-coated ITO/glass (b) substrates. Qxy and Qz refer to the in-plane and out-of-plane components of the scattering vector, respectively.

the edge-on and face-on ZnPc films before and after C_{60} deposition to compare the roughness of the bare films and surface coverage with C_{60}. The AFM analysis indicates that both ZnPc films are initially equally smooth and become equally smoother after 3 nm C_{60} deposition (Figure 4.6). This confirms that the differences in attenuation trends are not primarily influenced by morphological factors and can be assigned to differences in the extent of interfacial mixing.

To further validate these observations, we have complimented the surface-sensitive in situ XPS and UPS studies with more bulk sensitive measurements relying on a systematic GIWAXS analysis of fullerene-fullerene scattering with increasing thickness of fullerene on face-on and edge-on stacked ZnPc. Above the critical angle of the film, GIWAXS probes the entire sample volume, including the buried fullerene-ZnPc interface. We specifically look for the evolution of fullerene scattering features with increasing deposited thickness, which should behave monotonically if fullerene does not mix with the underlayer, whereas the same signal should decrease if instead fullerene diffuses and mixes with the ZnPc underlayer. While no significant change

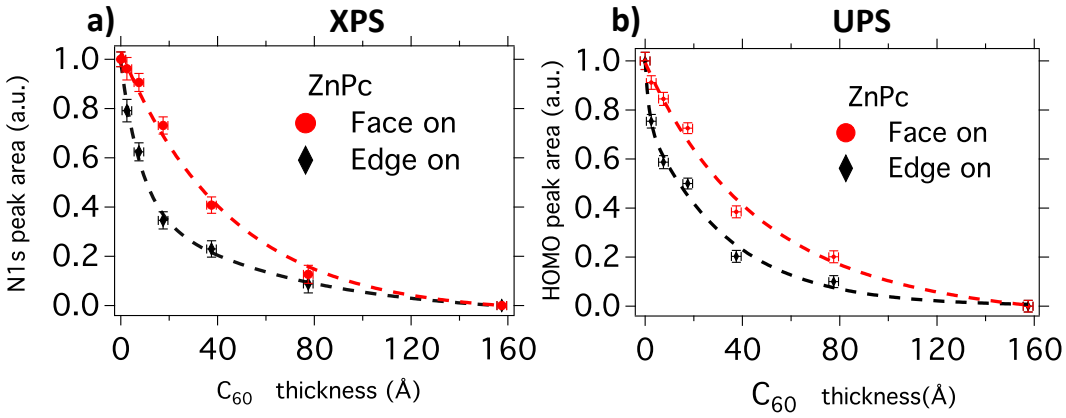

Figure 4.5: Attenuation of the nitrogen 1s peak from XPS (a) and ZnPc HOMO peak from UPS (b) of face-on and edge-on ZnPc with increasing C_{60} thickness. Both curves feature a more rapid decay of the photoelectron signal from the ZnPc layer in the edge-on case. In the face-on case the slower decay of the signal suggests more interfacial mixing. The dotted lines are added as visual guides to the eye. The nitrogen 1s peak was selected for the analysis because of its larger peak strength as compared to the Zinc 2p peak.

was detected in the evolution of the ZnPc peak, the C_{60} peak evolution indicates meaningful differences between edge-on and face-on ZnPc/C_{60} bilayers (Figure 4.7). Fitting the fullerene peak to a Gaussian function and preforming appropriate background subtractions, we plot the integrated fullerene signal as a function of the layer thickness (Figure 4.8). We observe that the C_{60} signal increases quasi linearly both on face-on and edge-on ZnPc films with increased fullerene thickness but consistently, the fullerene signal from edge-on samples are higher than that of face-on samples. This shows that in the face-on case, a portion of the C_{60} layer, and particularly the part deposited initially, scatters less than on edge-on ZnPc. Yet, it is known that the C_{60} peak has the same characteristics in both cases meaning the crystallite orientation in both cases were isotropic and the d-spacing is identical within the experimental error. We further remark that, the integrated scattered intensity of the 30 nm thick fullerene film on edge-on ZnPc is remarkably close to that of 30 nm C_{60} on bare ITO while the scattered intensity of the 30 nm thick film on face-on ZnPc is substantially

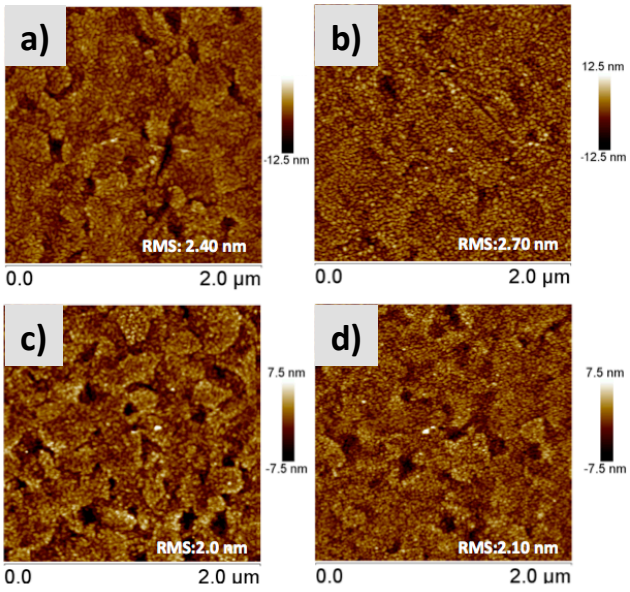

Figure 4.6: Shown in (a) are AFM topographic images (2μm x 2μm) of 20nm-thick pure ZnPc films evaporated at 0.5 Å/s on bare ITO. In (a) is a pure ZnPc film and in (c) is the same film with an additional 3nm-C_{60} layer . In (b) is the ZnPc film on CuI-coated ITO and in (d) is the film in (b) with an additional 3nm-C_{60} layer . Although the films appear to present slightly different morphology, they have a very similar root mean squared roughness both before and after C_{60} deposition ($\sim$2 nm) and surface area ($\sim$4.1 μm^2) implying that differences in surface physical roughness does not account when comparing the number of interfacial charge transfer states.

lower than the control on ITO, indicating that more C_{60} was lost through diffusion into the underlayer (Figure 4.7). In light of the GIWAXS, XPS and UPS results, we conclude that when fullerene-C_{60} is deposited on face-on ZnPc, it mixes to a greater extent than when it is deposited on edge-on ZnPc, in agreement with computational predictions which have identified differences in surface energies of face-on and edge-on films as the main driving force for interfacial mixing.[50]

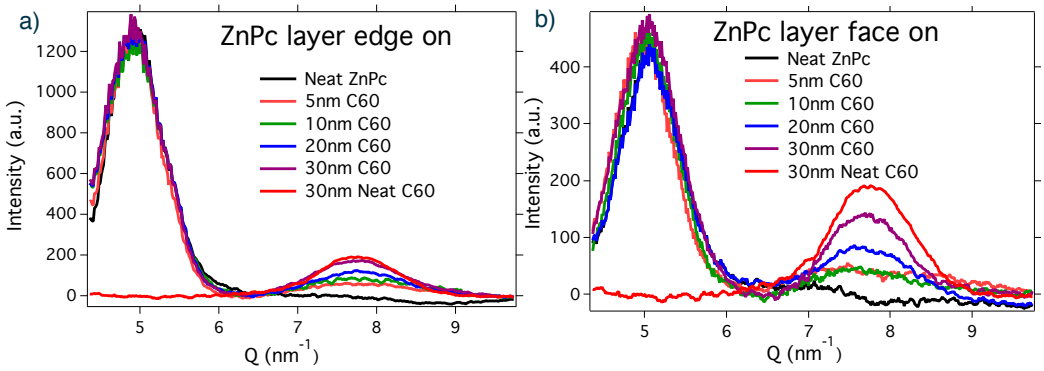

Figure 4.7: Line cuts showing the integrated scattered signal from the (200) and (002) peaks (at ∼4.9 nm-1) for ZnPc and for C_{60} (at ∼7.7 nm-1). Shown on the (a) is the evolution of the scattering signal on edge-on ZnPc on the (b) is the similar for face-on ZnPc.

4.3 Impact of interfacial mixing on the photovoltaic performance

We evaluate the impact of spontaneous interfacial mixing for the above molecular packing orientations by fabricating a series of devices with different ZnPc molecular packing orientations at room temperature. The device architectures are based on the standard device stacks: ITO/ZnPc (20 nm)/C_{60} (45 nm)/BCP (12 nm)/Al (100 nm) for edge-on ZnPc and ITO/CuI (2 nm)/ZnPc (20 nm)/C_{60} (45 nm)/BCP (12 nm)/Al (100 nm) for face-on ZnPc (Figure 4.9). The J-V curves and associated bilayer cartoons are presented in Figure 4.10 to 4.13, while device parameters and statistics are summarized in Table 4.1. The device characteristics of room temperature ZnPc and C_{60} on ITO and CuI/ITO are consistent with previously reported data whereby an increase in PCE of 70% was observed, [4] namely from 1.7% to 2.9% in going from a predominantly edge-on to face-on stacking orientation in the ZnPc layer.
To make solar cells with minimized interfacial mixing, we cool the substrate to 100 °C after ZnPc deposition at room temperature and subsequently deposit C_{60} on ZnPc (Table 4.1 Frozen C_{60}, Figure 4.10a,b).

With these cells, a reduction in the device PV performance is observed from 1.7%

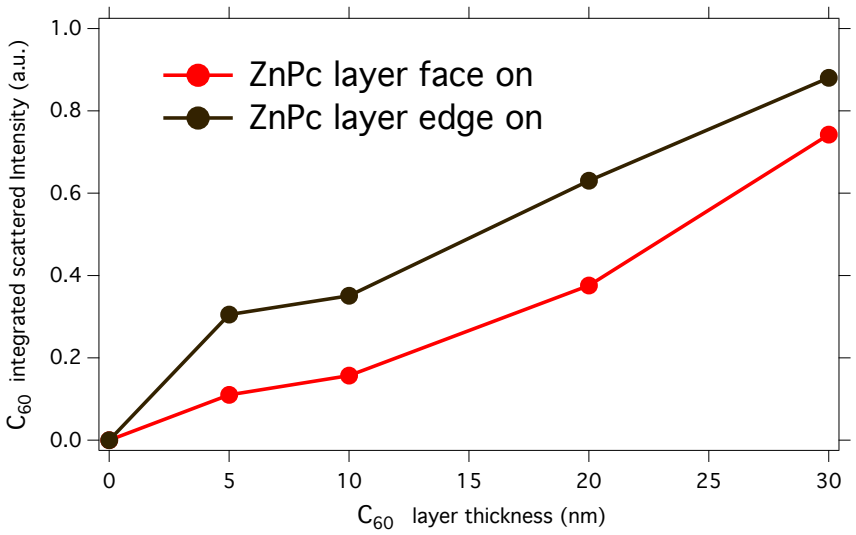

Figure 4.8: Integrated fullerene signal as a function of the C_{60} layer thickness. The data was obtained by fitting the fullerene peak for each thickness to a Gaussian function from which the peak area was computed and normalized to the area of the fullerene peak from a pure 30 nm neat fullerene film. On both face-on and edge-on ZnPc, the C_{60} signal increases quasi linearly with increased fullerene thickness but consistently, the fullerene signal from edge-on samples are higher than that of face-on samples indicating that in the face-on case, portion of the C_{60} layer scatters less light compare to the edge-on film. It is to be noted that the integrated scattered intensity of 30 nm fullerene for the sample with 30 nm was remarkably close to that of 30 nm C_{60} on bare ITO (30 nm neat C_{60}) as shown in Figure 4.7.

to 1.4% and from 2.9% to 2.3 % in the edge-on and face-on cases, respectively. This mostly stems from a reduction in photocurrents; ∼0.5 mAcm-2 vs. ∼1.10 mAcm-2 drops in the edge-on and face-on cases, respectively. A small decrease in FF is also noted in both cases and could be attributed to the presence of more disorder in the C_{60} layer deposited in cryogenic conditions. While we do not exclude the possibility of some interfacial mixing occurring once the device returns slowly to room temperature (Figure 4.11), we expect that molecules diffuse less once the bilayer is formed since molecules in the bulk or at the interface often do not enjoy the same degree of mobility as do molecules at surfaces. [196–198] The significant reduction in Jsc upon minimizing the intermixing suggests that the difference in photocurrents in devices prepared at room temperature is in part due to differences in the degree of

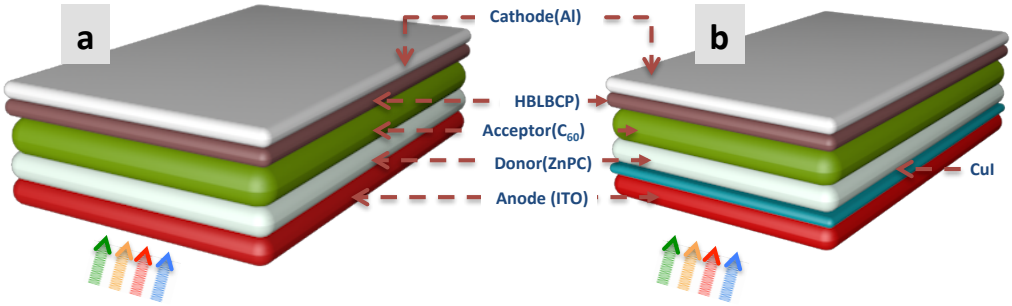

Figure 4.9: Bilayer device stacks ITO/ZnPc (20 nm)/C_{60} (45 nm)/BCP (12 nm)/Al (100 nm) for edge-on ZnPc (a) and ITO/CuI (2 nm)/ZnPc (20 nm)/C_{60} (45 nm)/BCP (12 nm)/Al (100 nm) for face-on ZnPc (b).

interfacial mixing for face-on and edge-on packed ZnPc films. This more favorably affects the BL device photocurrent in the face-on case since the mixed phase has been shown to induce band gap widening which leads to an energetic cascade that assists excitons dissociation. [146, 199]

To further probe whether interfacial mixing is a key and positive contributor to the performance improvement in face-on vs. edge-on BL solar cells, BL devices with a deliberately 1:1 mixed 3 nm interfacial layer on top of edge-on and face-on ZnPc films (Figure 4.12a,c) were fabricated. As expected, the presence of the mixed layer improves the edge-on BL device efficiency by ∼23% from 1.7% to 2.1%, and by ∼10% in the face-on case. The deliberately introduced mixed layer is hence less beneficial for the face-on device, which already had a mixed region spontaneously formed. More importantly the Voc of the face-on device remains unchanged at ∼0.6V while an increase in Voc, to practically an identical value to that of the face-on device, is observed for the edge-on device. In the frozen ZnPc devices (Table 4.1) the opposite trend in Voc is observed and vice versa, confirming that the reason for the observed changes in Voc is associated to the degree of interfacial mixing. Although a more focused study of recombination mechanisms is needed to fully understand these changes in Voc, the observations presented herein provide strong indication that the

Table 4.1: Photovoltaic performance characteristics measured under 100 mW/cm2 simulated AM1.5 irradiation. Jsc is short-circuit current density, FF is fill factor, Voc is the open-circuit voltage and PCE is power conversion efficiency. Standard bilayer refers to the RT devices under investigation.

Description	**Standard bilayer**		**Frozen C_{60}**		**Standard bilayer with mixed interface**		**Frozen ZnPc and C_{60},(Disordered bulk and more abrupt interface)**	
ZnPc stacking orientation	Edge-on	Face-on	Edge-on	Face-on	Edge-on	Face-on	Edge-on	Face-on
ZnPc dep. temp. [°C]	25	25	25	25	25	25	-100	-100
C_{60} dep. temp. [°C]	25	25	-100	-100	25	25	-100	-100
Mixed interlayer?	No	No	No	No	Yes	Yes	No	No
Voc [V]	0.57± 0.02	0.61± 0.01	0.56± 0.03	0.61± 0.02	0.60± 0.02	0.60± 0.02	0.58± 0.02	0.58± 0.01
FF [%]	63.30± 0.5	70± 0.4	59.70± 0.5	68.10± 0.6	62.40± 0.6	69.10± 0.3	66.30± 0.4	64.00± 0.6
Jsc [mA/cm2]	4.70±0.1	6.70±0.1	4.10±0.1	5.60±0.1	5.60± 0.1	7.70± 0.1	4.40± 0.1	5.20± 0.1
PCE [%]	1.70± 0.06	2.90± 0.04	1.40± 0.04	2.30± 0.05	2.10± 0.05	3.20± 0.04	1.70± 0.05	1.90± 0.06

spontaneously formed mixed layer is responsible for the higher Voc observed in the face-on devices. However, this increase in Voc stemming from the mixed phase is a priori counterintuitive when examined from the point of view of disorder in the mixed interfacial layer, but as will be discussed later and has been shown in the context of polymer:fullerene solar cells, disorder in the mixed interfacial phase favorably impacts interfacial energetics in a manner that favors charge generation.[146, 199] Hence, in light of these results together with the photoelectron spectroscopy data, it appears that more spontaneous interfacial mixing occurs in nominally face-on BL devices than in edge-on ones fabricated at RT, and that this interfacial mixing is in part responsible for the higher photocurrent, Voc and power conversion efficiency in the face-on devices.

A direct and inevitable consequence of intermixing should be an increase in the number of ZnPc:C_{60} bimolecular charge transfer (CT) complexes at the D-A interface. An important characteristic of the CT complex is that it can be photoexcited by direct sub-gap monochromatic illumination and the resulting excited states can generate free charges, which can be collected by the electrodes. The generated charges can be

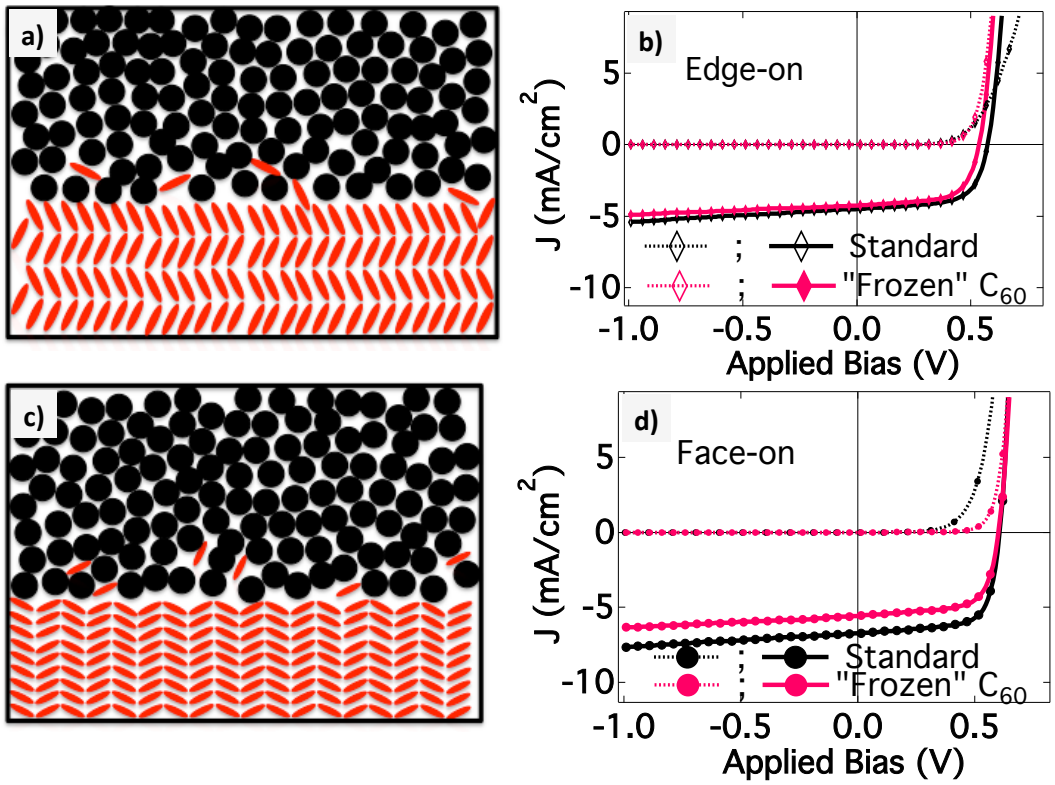

Figure 4.10: Current-voltage characteristics under illumination (solid curves) and in the dark (dotted lines) of face-on and edge-on ZnPc/C_{60} BL solar cells with altered interfacial and bulk molecular packing structures (b,d). The black color shows the characteristics of the standard devices for comparison. The schematic in (a,c) illustrates the ZnPc molecular conformation and the extent of mixing at the interface. The fullerene-C_{60} is deposited at -100 °C (referred to as frozen) to reduce interfacial mixing in order to achieve a more abrupt interface.

detected by a sensitive external quantum efficiency (EQE) measurement performed on a PV device, making it possible to directly investigate interfacial mixing in actual devices. The EQE from the charge transfer state absorption band is modeled by Equation 4.1.

$$EQE_{PV} = \frac{1}{E\sqrt{4\pi\lambda kT}} \exp \frac{-(E_{CT} - \lambda - E)^2}{4kT} \tag{4.1}$$

Here, as discussed in Chapter 2, E_{CT} is the energy of the CT state, λ is related to the reorganization energy and energetic disorder,[180] and f is directly related to the

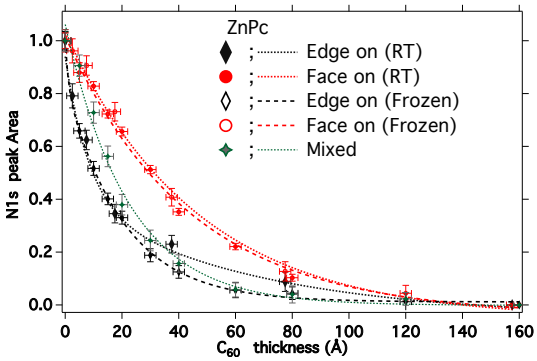

Figure 4.11: Attenuation of the nitrogen 1s peak from XPS of face-on and edge-on ZnPc for RT, frozen ZnPc with a mixed interface. Introducing a mixed layer results in a faster attenuation, which further supports, our hypothesis that the difference in attenuation for the face-on and edge ZnPc is indeed attributed to the extent of mixing. The attenuation trend for the frozen edge on ZnPc shows the fastest decay. However in the case of the frozen face-on ZnPc, the decay trend is very similar to that of the room temperature face-on ZnPc and clearly indicates that comparable degree of mixing occurs.

intensity of the CT absorbance band. Specifically, f is the product of the number of interfacial CT complexes, the internal quantum efficiency (IQE) of the CT state, and the square of the electronic coupling matrix element. Therefore, f should be proportional to the film thickness if the CT states are assumed distributed evenly throughout the film. In addition, with f being directly proportional to the number of CT complexes, an increase in f for the same material system can be utilized as a means of determining the relative number of CT complexes. Based on this, we have fabricated a series of BL devices with variable ZnPc thickness and measured the strength of the CT absorbance (Figure 4.14a,b). Fitting the CT band to the above equation, we extract f and E_{CT} for each device (Table 4.2). The magnitude of the CT absorbance increases with ZnPc thickness (Figure 4.15) in the face-on case ($\sim$90% increase in f) while remaining virtually unchanged in the edge-on case. It is important to note that the direct excitation (1.5-2.0 eV) of the face-on ZnPc also increases with increased thickness and follows the same trend as the CT band excitation. This could therefore lead to a misinterpretation of the observed increase

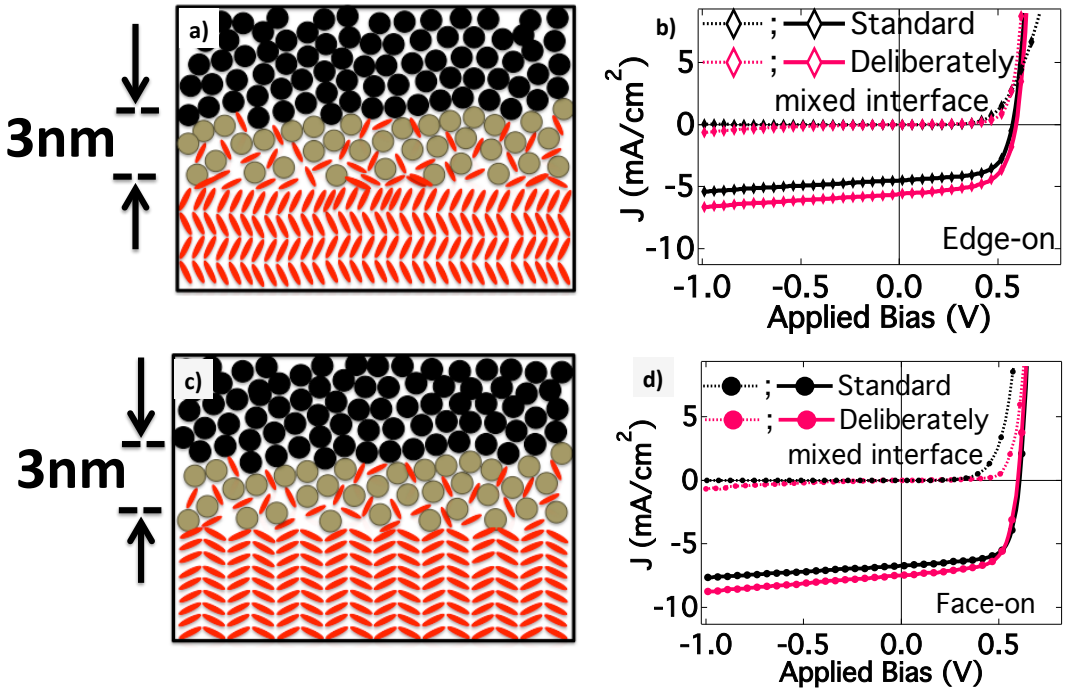

Figure 4.12: Current-voltage characteristics under illumination (solid curves) and in the dark (dotted lines) of face-on and edge-on ZnPc/C_{60} BL solar cells with altered interfacial and bulk molecular packing structures. The black color shows the characteristics of the standard devices for comparison. The inset schematics illustrate the ZnPc molecular conformation and the extent of mixing at the interface. The grey circles illustrate fullerene-C_{60} in the deliberately mixed layer (a, c). Devices made with a deliberately mixed co-deposited interfacial layer demonstrating the impact of the mixed layer on PV performance (b, d).

in f (Figure 4.14b,d). However, looking at the corresponding trends in the edge-on ZnPc whereby the increase in the direct excitation leads to virtually no increase in the CT band excitation (Figure 4.14 a,c), we conclude that the opposite trend observed in the face-on case is indeed due to a real increase in CT absorption at the D-A interface and not to any tailing of the absorption of ZnPc. In addition, we rule out the possibility that the difference in CT state absorption may be due to differences in interfacial physical roughness between the edge-on and face-on films on the basis of AFM analysis (Figure 4.6), which revealed very similar surface roughness for both types of films. Similarly, one might argue that the D/A electronic coupling

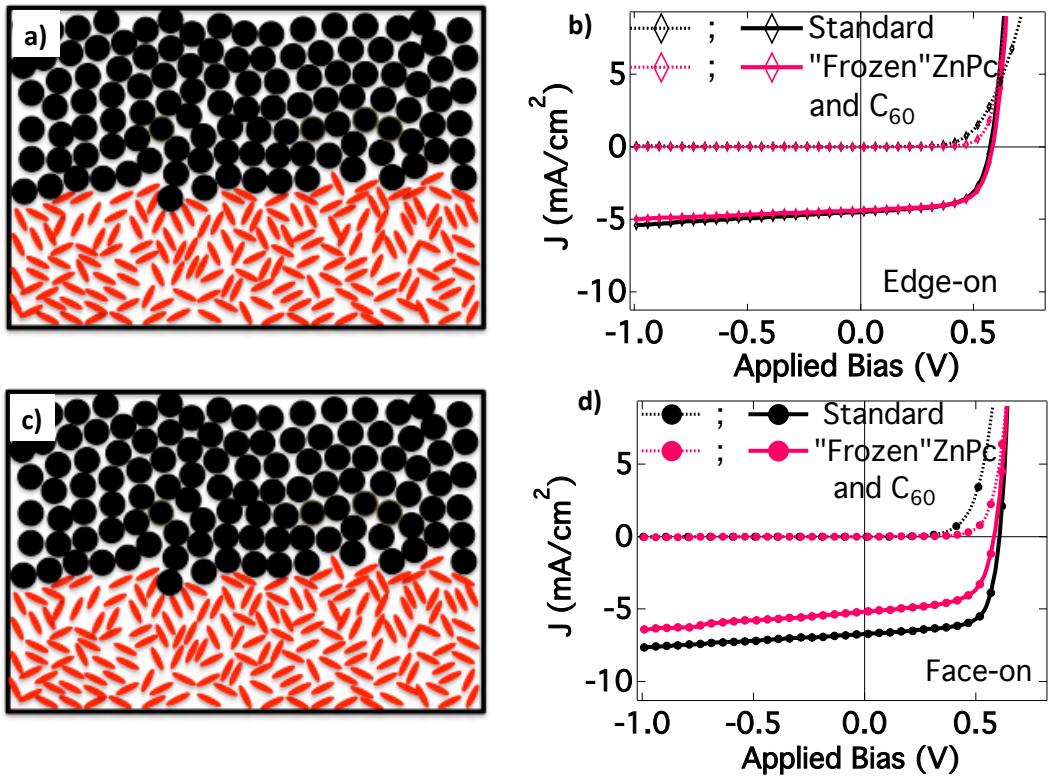

Figure 4.13: Current-voltage characteristics under illumination (solid curves) and in the dark (dotted lines) of face-on and edge-on ZnPc/C_{60} BL solar cells with altered interfacial and bulk molecular packing structures. The black color shows the characteristics of the standard devices for comparison. The inset schematics illustrate the ZnPc molecular conformation and the extent of mixing at the interface (a, c). Both the ZnPc and C_{60} layers are deposited at -100 °C and therefore frozen to achieve a more abrupt interface and a disordered ZnPc bulk (b, d).

should be lower in the edge-on orientation, which decreases f, resulting in fewer subgap states being excited upon illumination. However, we believe that even if that were the case, the dependence of the CT absorption on the film thickness for films prepared in identical conditions should still be representative of the variation in the true concentration of CT states that are formed as the film thickness is varied, making such relative comparisons meaningful. Hence, the increase in CT absorbance most likely corresponds to an increase in the number of CT states as a result of increased mixing at the face-on ZnPc/C_{60} interface. The fact that f increases with

film thickness in case of face-on stacked ZnPc films, but not for edge-on stacked films is consistent with no additional intermixing occurring upon deposition of the first monolayer of fullerene in the latter case, whereas in the former case the supply of more fullerene allows the system the undergo further intermixing, resulting in more CT state formation.

4.4 Role of bulk molecular packing and interfacial mixing on the amount of excitons reaching a D-A interface

We now have a better handle over the influence that the degree of mixing at the D-A interface can have on the device photocurrent. One should not forget, however, that differences in molecular orientation at the interface stem from stacking differences in the bulk of the donor film. Bulk orientation differences may impact the exciton diffusion length and film absorbance, and therefore affect the device photocurrent. We evaluate the differences in the number of excitons reaching a D-A interface by comparing the EQE of BL devices with different ZnPc thickness, both in predominantly edge-on and face-on orientations (Figure 4.14c,d). The EQE signal in the case of the edge-on BL devices increases marginally with the ZnPc layer thickness in the key spectral range 1.5-2.2 eV corresponding to the ZnPc Q-band absorption. By contrast, a significant increase of EQE is seen with increasing thickness of face-on ZnPc. These observations indicate that more excitons are reaching the D-A interface for thicker ZnPc films in the presence of predominantly face-on stacking of ZnPc molecules in the donor layer than in the presence of edge-on stacking, likely due to both differences in exciton diffusion length and interfacial mixing in favor of the former.

We further seek to isolate and validate the contributions to the photocurrent from the bulk molecular packing and interfacial mixing. We have fabricated devices wherein both the ZnPc and the C_{60} layers are deposited at cryogenic temperatures. This promotes a reduced molecular ordering in the ZnPc bulk (Figure 4.16) while also

maintaining a minimally mixed interface. The device results (Table 4.1, Frozen ZnPc and C_{60} and Figure 4.13b,d) show very close PCEs for BL devices on Indium Tin Oxide (ITO) and ITO/CuI, namely 1.7% and 1.9%, respectively, consistent with the fact that both the interface and the bulk are nearly identical in the two device architectures. In comparison to the previous case in which C_{60} was deposited under cryogenic conditions on ZnPc deposited at room temperature (2.3%), the BL device fabricated fully in cryogenic conditions on CuI/ITO exhibits a further decrease in PCE attributed to all device performance parameters degrading, especially the FF. We find it intriguing and telling that a disordered crystalline ZnPc film should behave just as well as a predominantly edge-on oriented polycrystalline film in terms of device performance. This may be an indication that out-of-plane exciton diffusion in small-molecule donor films exhibiting predominantly in-plane -stacking is similar to that of a fully disordered layer.

Table 4.2: Electronic coupling term and charge transfer state energy values extracted from fitting the absorption band of the CT state obtained from sensitive EQE measurements on devices with variable ZnPc thickness

	Edge-on		**Face-on**	
ZnPc thickness (nm)	f(x10-4 eV^2)	E_{CT} (eV)	f(x10-4 eV^2)	E_{CT} (eV)
4	1.50	1.16	1.40	1.14
6	1.58	1.13	1.69	1.15
8	1.48	1.10	1.97	1.13
10	1.54	1.14	2.67	1.13

Importantly, these results indicate that bulk ordering and stacking direction play important roles alongside interfacial mixing at improving PV performance in small-molecule organic solar cells. The same may not be true in polymer-fullerene solar cells, where intrachain transport is believed to be a dominant contributor to carrier and energy transport.[108, 200, 201] Finally, the mixed interfacial layer in face-on devices is believed to introduce an energetic gradient between the pure fullerene and ZnPc phases that should assist in charge separation and reduce geminate recombination as

has been demonstrated by others.[146, 199] This could explain the increase in Voc in the edge-on ZnPc device with deliberate mixing.

4.5 Conclusions

The present study reveals the impact that stacking orientation can have on the donor-acceptor interface in organic solar cells. We have focused our attention on vacuum-deposited bilayer solar cells where state-of-the-art ultra high vacuum molecular beam deposition techniques allow us to control and ultimately decouple interfacial and bulk molecular stacking effects, with broad implications for either solution and vacuum deposited small-molecule, oligomer and polymer based bilayer and bulk heterojunction solar cells. Through careful experimentation we find that differences in stacking orientation in the bulk and surface of ZnPc films can lead to significant differences in the mixing behavior at the interface with C_{60}. We demonstrate that spontaneous interfacial mixing at room temperature is more favored in face-on terminated ZnPc films than in edge-on terminated ones. The induced mixed layer benefits the bilayer solar cells by increasing the photocurrent and open circuit voltage and its presence at the D-A interface is believed to promote charge separation owing to changes in the energetic landscape that it creates. We have also found that when the molecules pack face-on in the bulk, this contributes to more excitons reaching D-A interfaces, and hence also accounts for the observed improvement in device photocurrent. This study highlights the importance of molecular packing in OPV bilayer devices and its dual impact on both bulk and interfacial PV processes. The ability to precisely control the molecular orientation both in the bulk and at the D-A interface in order to achieve more face-on donor films may play a key role in enabling further improvements in PV performance. This study equally highlights the risks associated to extrapolating interface-related conclusions and interpreting device performances simply on the basis of bulk molecular stacking information in small molecules solar cells either in bilayer

or bulk heterojunction device configurations without looking at the state of frontier molecules before and after bilayer formation. While some of the outcomes of the study, such as the link between bulk molecular stacking and exciton diffusion, may not directly apply beyond bilayer solar cells to modern bulk heterojunction systems, our approach nevertheless offers opportunities to investigate a subset of interfaces within a typical bulk heterojunction solar cell but which, due to their extremely complex combination of morphologies, currently cannot be directly addressed using mean-field spectroscopic techniques. Certainly, the conclusions of this study, with regards to spontaneous interfacial mixing, its link to conformation of frontier molecules and the influence of mixing on free carrier generation and recombination are believed to be widely applicable to bulk heterojunction solar cells. [202–204]

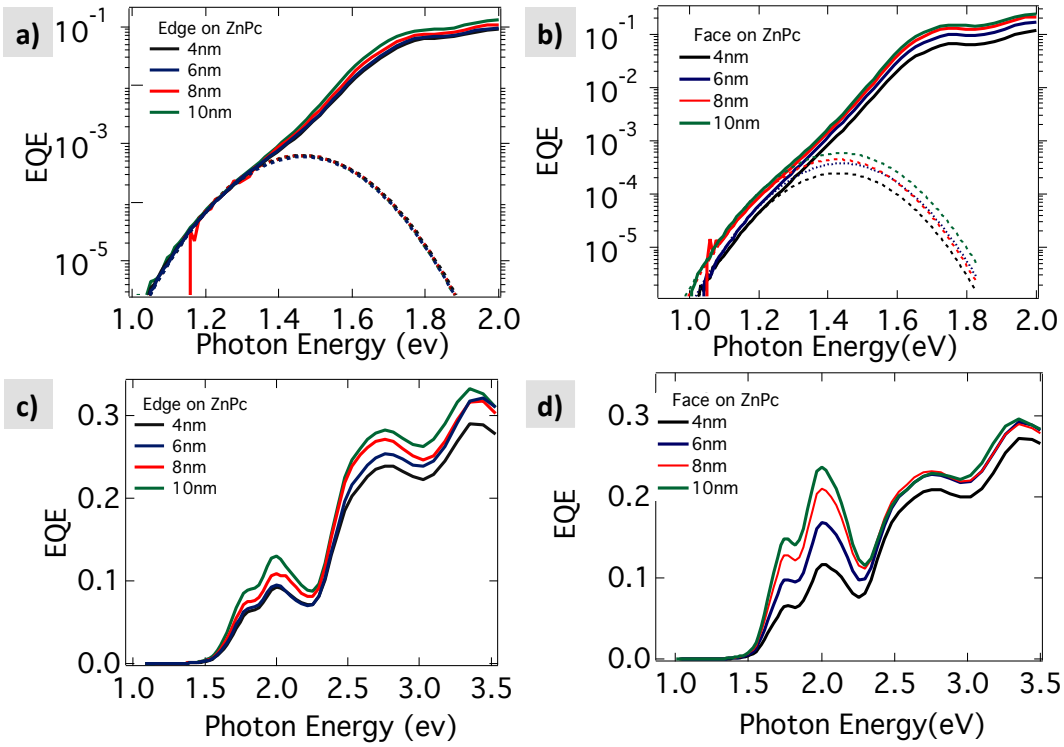

Figure 4.14: Spectrally resolved sensitive EQE spectra of ZnPc/C_{60} BL cells including in the subgap spectral range with varying thickness of predominantly edge-on (a) and face-on (b) stacked ZnPc deposited at room temperature showing the evolution of the CT absorption band. The fits (dotted curves) are performed to extract the electronic coupling term (f), which is directly proportional to the number of interfacial charge transfer states. Bottom: Evolution of the spectral response of the ZnPc/C_{60} BL solar cells with edge-on (c) and face-on ZnPc donor layer (d) as a function of the ZnPc layer thickness. For the edge-on ZnPc BL devices, the EQE increases only marginally with increasing ZnPc layer thickness. For the face-on ZnPc BL devices, the EQE signal increases more markedly with increasing ZnPc thickness.

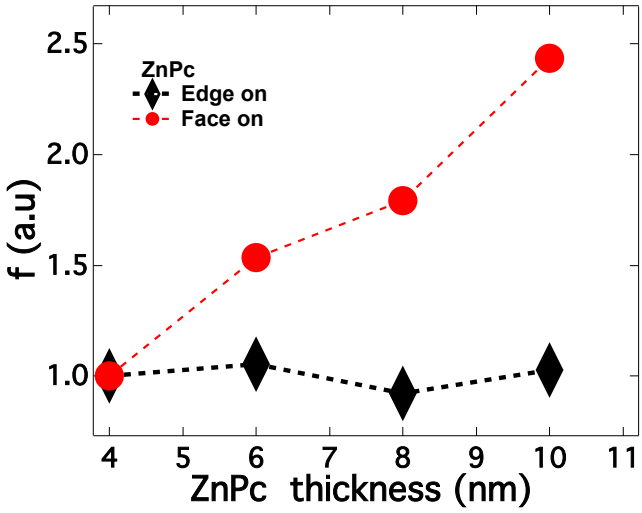

Figure 4.15: Evolution of f with ZnPc film thickness for the edge-on and face-on stacked BL devices. The increase observed in the case of face-on stacked ZnPc indicates increased degree of interfacial mixing.

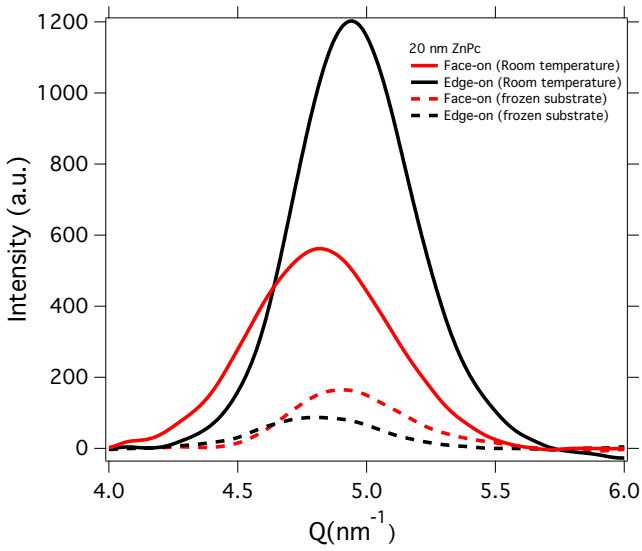

Figure 4.16: Combined integrated peak intensities for (200) and (002) peaks for edge-on (on ITO) and face-on (on CuI) ZnPc films grown at room temperature and on a frozen substrate (-100 °C). The scattering intensity is significantly reduced for the films cast under cryogenic conditions indicating that suggesting that most of the film volume is disordered even if some portion of film remains crystalline or recrystallizes.

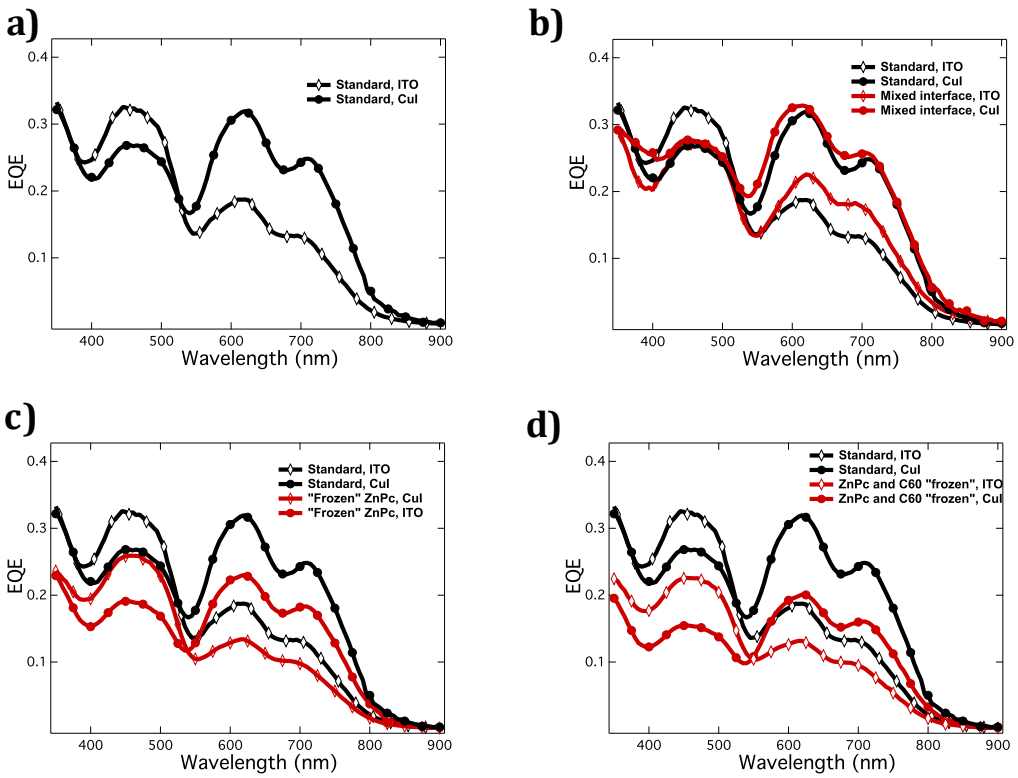

Figure 4.17: Comparison of EQE responses of the ZnPc:C_{60} bilayer solar cells. Standard devices only (a); standard devices with devices with a 3 nm deliberately mixed layer (b) with devices with more abrupt interface i.e. frozen ZnPc (c) and with devices with disordered ZnPc bulk and more abrupt interface i.e. ZnPc and C_{60} both frozen (d).

Chapter 5

The Roles of Structural Order, Intermolecular Interactions and Conformation in D-A blends and Implications for Excitons Dissociation

5.1 Introduction

In Chapter 4 we showed, using crystalline ZnPc as donor, how donor molecular packing orientation influences the nanoscale interfacial order and exciton dissociation yield in solar cells. We found that the donor-packing determines the direction of efficient exciton transport but also impacts the degree of interfacial order owing to ZnPc mixing with fullerene preferentially in the face-on conformation. The formation of the mixed interfacial phase in the case where the donor packed face-on provided the suitable interfacial energetic landscape for efficient exciton splitting into free carriers. But how exactly the favorable energy landscape comes about owing to the presence of the mixed phase was not discussed. In this chapter we discuss the factors that determine the energy landscape a various donor-fullerene interfaces in organic solar cells. The energy landscape in organic semiconducting materials significantly influences charge and exciton behavior, which are both critical to the operation of organic electronic devices. These energy landscapes can change dramatically depending on the phases that are present in the material. For instance, the presence of a charge in an organic molecule in the solid state creates and electric field that the surrounding molecules experience. Theses surrounding molecules therefore respond to the presence of an electric field by the formation dipoles or quadrupoles that in turn interacts which the

charge molecule in such a way that energy gain results. By the same mechanism, the electronic density on a neutral molecule through dipole-dipole interaction or induced dipole induced dipole interaction stabilizes the both the ground state and the first excited state of the molecules. Under those circumstances, the materials shift with a magnitude that depends on both the density and chemical natures of the molecules that surrounds each molecule. In a donor acceptor blend, pure phases of donor or acceptor and mixed phases of donor and acceptor exhibiting different degrees of order and composition can all coexist. In this work, ultraviolet photoelectron spectroscopy (UPS) measurements of ionization energies (IEs) and external quantum efficiency measurements of charge-transfer (CT) state energies (E_{CT}) are used to characterize energy landscapes of four molecular photovoltaic material systems, NPD, bDIP and 6T used with C_{60} to make bilayer and blends. The significant finding is that the ionization energies (IEs) and the energy of the charge transfer state (E_{CT}) values vary enormously depending on the blends structural order and phase composition. In the sexithiophene:C_{60} system both the IE of sexithiophene and C_{60} shift by over 0.4 eV while E_{CT} shifts by 0.5 eV depending on molecular composition. By contrast, in the rubrene:C_{60} system the IE of rubrene and C_{60} vary by $\leq$0.11 eV and E_{CT} changes by $\leq$0.04 eV as the material composition varies. The large magnitude of the shifts in the 6T:C_{60} is synonymous to a vanishingly small or no Coulombic barrier at the interface between the mixed of pure 6T phases.

5.2 How the energy landscape controls charge separation at the donor-acceptor interface?

As discussed in Chapter 2, interfacial CT excitons remain coulombically bound because of the low dielectric constant of organic semiconductors. This binding energy effectively represents an energy barrier that the charges in the CT exciton should overcome as they attempt to form free carriers. Factors that affect the probability of

bound CT excitons to separate such as the CT state lifetime, the mobility of carriers right at the D-A interface and the presence of a three-phase morphology are critical in determining the efficiency of the charge separation process. While long-lived CT states mean that carriers in the CT states undergo many attempts to split, thus a high probability to overcome the Coulomb well, high carriers mobility and a three-phase morphology that creates and downhill energy landscape achieve the same goal. In fact, a downhill energy landscape would mean vanishing of the Coulomb well and necessarily a high local mobility for charges (Figure 5.1). In the following section, we assess the energy landscape in materials blends and implications for charge separation. We probe the energy landscape by performing accurate measurements of ionizations potentials and charge transfer state energies of a series of materials systems.

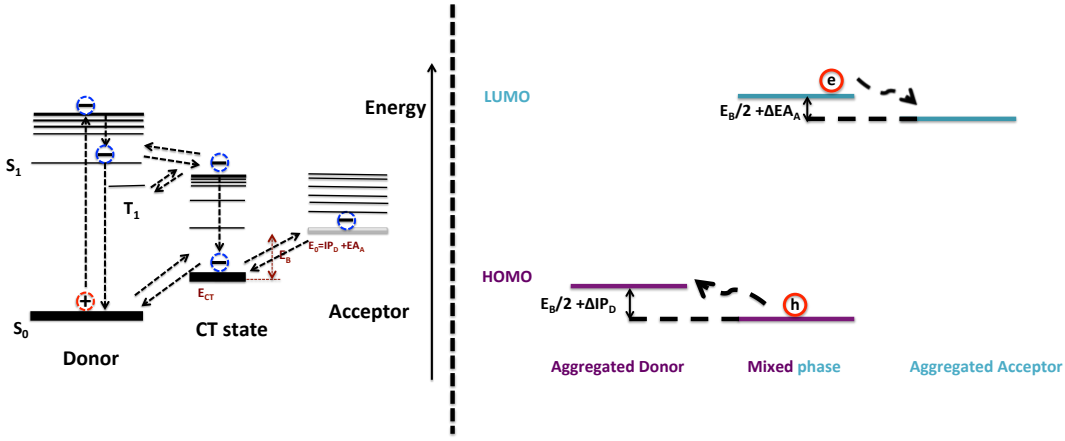

Figure 5.1: Left: Excitons occupying CT states are bound (The Binding energy, E_B, is often in the range 0.25 to 0.5 eV assuming an isolated charge-transfer (CT) complex, where the hole is localized on a donor molecule and an electron on the acceptor molecule) because of the high dielectric constant of organic semiconductors. An energy landscape that provides a driving force to overcome the CT binding energy would enable and efficient separations of the bound CT excitons into free carriers. Right: Schematic showing how shifts in donor ionization potential ($\triangle IP_D$) and acceptor electron affinity ($\triangle EA_A$)in the mixed phase, through destabilization of both electrons and holes, would provide the driving force necessary to overcome the CT binding and facilitate the formation of free carriers.

5.3 Ionization potentials of materials in pure films and blends

We first measure the IEs of the pure materials evaporated as thin films on Au foil (Figure 5.2). The spectra of the donor materials show an onset of the highest energy levels clearly distinct from that of the acceptor C_{60}. For this reason, the IEs of the donors molecules were extracted from spectra without further processing of the spectra. To extract the feature of the blends spectra corresponding to the ionization of the highest occupied orbitals (often loosely referred to as the HOMO peak) of C_{60} in the blends with $\geq$50% 6T, the pure 6T component (Figure 5.4) was subtracted by initially shifting the 100 % 6T (pure film in Figure 5.2) to match the 6T feature in the blend spectrum (92% 6T in Figure 5.3), giving the 100% 6T adjust spectrum. The 100% 6T adjusted spectrum was then subtracted from the 92% 6T spectrum to yield the pure C_{60} contribution to the original the spectrum.

In Figure 5.3a, are shown UPS spectra featuring the onset of the highest occupied orbitals in reference to the vacuum level at 0 eV, as a function of 6T composition in 6T:C_{60} blends. As the 6T content is increased in the blends, the IE of the 6T film increases. A significant shift of 0.6 eV between the IE of 6T in films with $\geq$75% (by vol.) 6T composition and that of 6T in films with $\leq$25% 6T. This shift implies that the hole is significantly more stabilized in blends with a high content of 6T (more pure 6T, $\geq$75%) than in blends containing predominantly C_{60}. That is to say that if phases of increasingly pure 6T appear next to each other ($\leq$25% 6T to $\geq$75% 6T), there will be a 0.6 eV driving force that will funnel the holes appearing in the mixed phases into the pure 6T. Equally important and often overlooked is the evolution of the ionization potential of C_{60} in the blends with varying donor content. A comparison of the C_{60} spectra with varying 6T content show equally (Figure 5.3b) large shifts to those observed for 6T. The C_{60} IE increases from 6.06 to 6.45 eV as the 6T content is decreased from 92 to 0%. These shifts in both the IE of 6T and C_{60} as a function of blend composition are remarkably large and notwithstanding, they are often ignored

in the organic photovoltaic literature, and the IE of the donor is frequently assumed to be invariant with blend composition.[168, 205, 206]

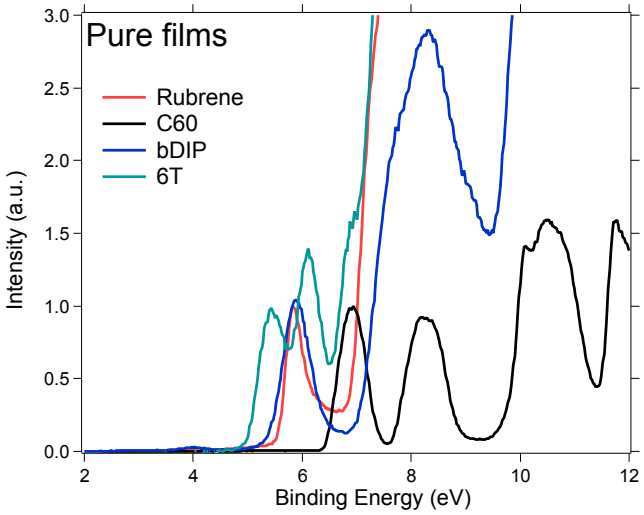

Figure 5.2: UPS spectra of pure films on Au foil for rubrene, C_{60}, bDIP and 6T. The binding energies were adjusted to $E_{vac} = 0$ (i.e. all as obtained spectra with $E_{Fermi} = 0$ were shifted by the work function). The IEs were extracted from the intercept of a linear fit to the onset of the first ionization with the background.

5.4 Origin of the shifts in ionizations energies

We would like to explain how the shift in IEs arises. They are several factors that may explain the origin of such shifts including changes in polarization energy and degree of structural order. We first investigate the changes in the structural order of 6T and fullerene 6T in the blends. As can be seen in Figure 5.5, the degree of structural order of 6T in the blend changes with blend composition. In the pure 6T film and at low C_{60} content (9:1 6T:C_{60}) exhibit clear diffraction peaks indicating the presence of large 6T aggregates. However, at a 1:9 6T:C_{60} no 6T diffraction peaks can be identified. These results suggest that the shifts in IEs of 6T can be attributed to changes in the degree of order of 6T molecules. In the ordered or aggregated form, the 6T film is denser and closely surrounded by other 6T molecules. In the pure or 9:1 6T:C_{60} film, the aggregates provide, through polarization, maximal stabilization to the positive charge

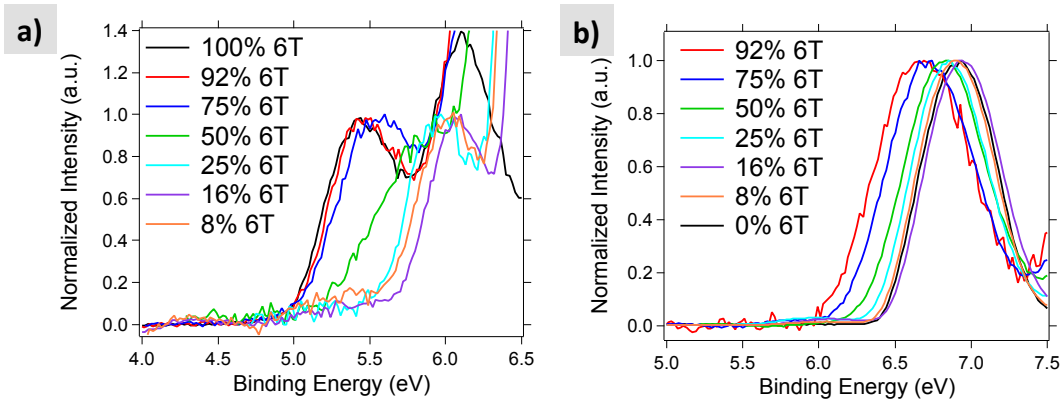

Figure 5.3: UPS spectra of the HOMO region for 6T (a) and C_{60} (b) in films of varying 6T:C_{60} blend composition (listed as volume % 6T) with the binding energy adjusted to Evac=0 (i.e. all as obtained spectra with $E_{Fermi} = 0$ were shifted by the work function). In b) the pure 6T contribution for 6T concentrations of $\geq$50% was subtracted from the blend spectra to leave only the C_{60} contribution.

left behind upon ionization of a 6T molecule while in the 1:9 6T:C_{60}, 6T molecules are mostly surrounded by C_{60} which does not stabilize the 6T cation as effectively as pure 6T aggregates. However, UV-Vis absorbance measurements revealed that polarization is not the only factor that explains the shifts in 6T IEs. Absorbance measurements would be less sensitive to polarization effects than UPS (Figure 5.6), and can be used to revealed effects such as the role of molecular conformation. The absorbance onset for pure 6T films is determined to be 2.25 eV (Figure 5.6a), which is consistent with previously reported values in the literature,[207] whereas in solution 6T displays a 0.22 eV blue-shifted absorbance onset of 2.47 eV.[208] This red-shift in absorbance onset in moving from solution to the film is in part due to the increased molecular planarity, as supported by red-shifts in oligothiophene absorbance in solution as the temperature is decreased from 298 K to 77 K.[208] Coupled with the absorbance measurements, the scattering data support that the shifts in IEs of 6T are due to a combination of two effects: degree of long-range order and molecular conformation. Thus of 0.6 eV shift in ionization energy in pure 6T vs. 1:9 6T:C_{60} films 0.38 eV, representing the shift observed in the absorbance edge between film

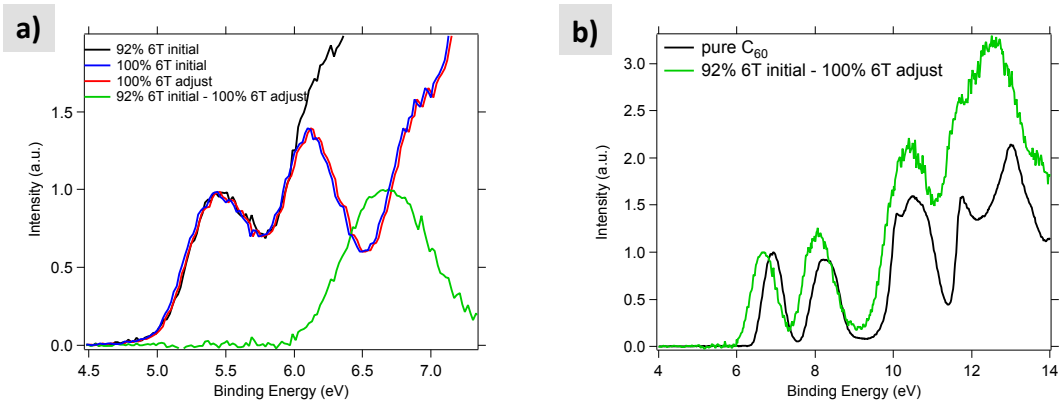

Figure 5.4: Spectral series showing the subtraction of the 6T contribution from a blend film to extract the spectra of C_{60} (a) and a comparison of the C_{60} contribution in the 92% 6T film to pure C_{60} (b). Note that the same features are present in the spectrum of pure C_{60} and the C_{60} component in the 92% 6T blend.

and solution spectra is attributable to polarization effects. This conclusion is further supported based on the differing polarization energies of C_{60} and 6T. Here, the polarization energy of C_{60} is 1.2 eV, while the polarization energy of 6T is 2.0 eV.[209, 210] These polarization energies are determined based on the difference between the previously reported gas phase IE and the solid state IE measured in this work. The nature of these interactions are a subject of active investigation, and with a couple of exceptions,[152, 211] most work suggests that these energy level shifts do not arise from ground state charge transfer but mainly from electrostatic interactions as discussed in Chapter 2. [146, 148–150] Another compelling evidence that polarizations effects contribute significantly to IEs shifts for both donor and acceptor in blends comes from the investigation of the rubrene:C_{60} system.

In Figure 5.7 the UPS spectra focusing on the feature corresponding to the ionization of the highly occupied orbitals of rubrene and C_{60} in blends films are shown. The IE of rubrene and C_{60} changes by $\leq$0.11 eV as the blend composition varies. This low magnitude of these shifts is however in opposition to the dramatic shifts of 0.6 eV observed in the case of the 6T:C_{60} blends. One may be tempted to assign the

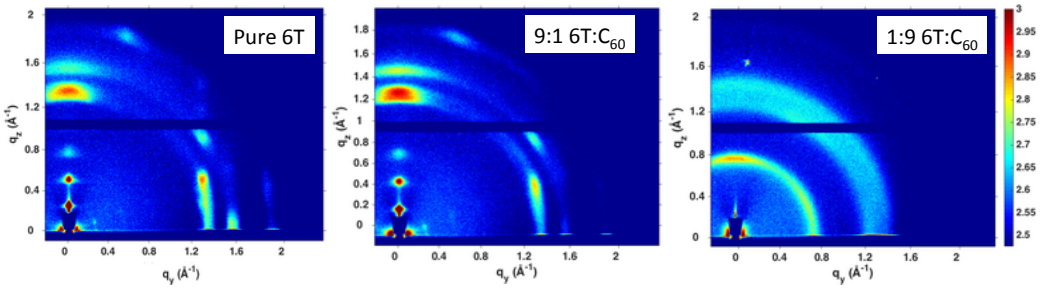

Figure 5.5: Grazing incidence wide-angle X-ray scattering spectra for pure films of 6T and 6T:C_{60} blends. As the ratio of C_{60} is increased in the blends, from 9:1 6T:C_{60} to 1:9 6T:C_{60}, 6T scattering peaks evolve to broad rings indicating that 6T crystallization disrupted by the presence of C_{60} becomes less aggregated.

almost insignificant shifts in IE in the case of rubrene:C_{60} to the amorphous nature of rubrene. Although this may be true, literature reports for ZnPc:C_{60} and CuPc:C_{60} blends IE shifts of $\leq$0.25 eV and no change at all, respectively, were observed based on blend composition.[212, 213] Given that both ZnPC and CuPc are both crystalline as deposited, it appears it is not the ability to crystallize per se that brings about the shifts in the materials ionization potential, but the polarization energy, i.e. the ability of the molecular environment within the blend to stabilize cations that by and large that gives rises to the shifts in IEs. This observation is in agreement with similar polarization energies of 1.1 eV for rubrene and 1.2 eV for C_{60}.[82, 214]

An important point to elucidate is whether the trends observed for 6T:$_{60}$ and rubrene:C_{60} is shared by analogous materials systems. We thus investigate blends of bDIP or NPD with C_{60}. bDIP form polycrystalline films as deposited (Figure 5.9) while NPD forms and amorphous film (Figure 5.8). bDIP is more polar than NPD because of it fluorine atoms (Figure 3.1 Chapter 3) and we thus expect its polarization energy to be higher. Taking the case of pentacene, the introduction of fluorine has been shown to induce a shift in the film IE as large as 2eV.[215] As shown in Figure 5.10a, a significant shift in the IE of bDIP (likewise for C_{60}) of 0.34 eV is measured as the blend concentration is varied from 100% to 8% bDIP:C_{60} while in the NPD:C_{60} system, neither NPD nor

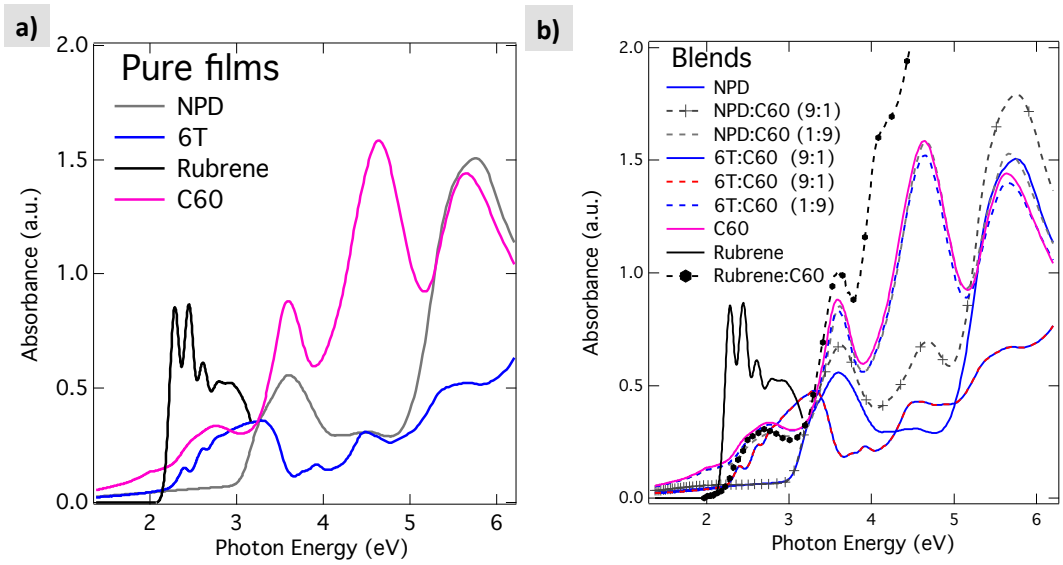

Figure 5.6: UV-Vis absorbance spectra of C_{60} and pure donor films (a) and blends (b). Vibronic features and spectra onsets for blends spectra show little to no shifts in comparison to pure materials spectra. Thus polarization effects are much less pronounced in optical absorbance spectroscopy as compared to UPS essentially because excitons are neutral species and therefore less polarizable.

C_{60} shows a significant change in IE as a function of composition.

We again attribute this shift in the IEs in the bDIP:C_{60} primarily to differences in polarization energy. However, neither calculated nor experimentally measured polarization energies for bDIP are available for comparison. In the NPD:C_{60} system, the lack of change is in agreement with the similar polarization energy of NPD (1.4 eV) with C_{60} (1.2 eV), where the polarization of NPD is based on the calculated gas-phase IE and the IE measured in this work. The summary of both donor and C_{60} IEs in the different blends, as shown in Figure 5.10, highlights how drastically IEs are affected by the particular donor molecules and blend composition. As discussed earlier, these differing energy landscapes are expected to influence PV device processes and performance significantly.

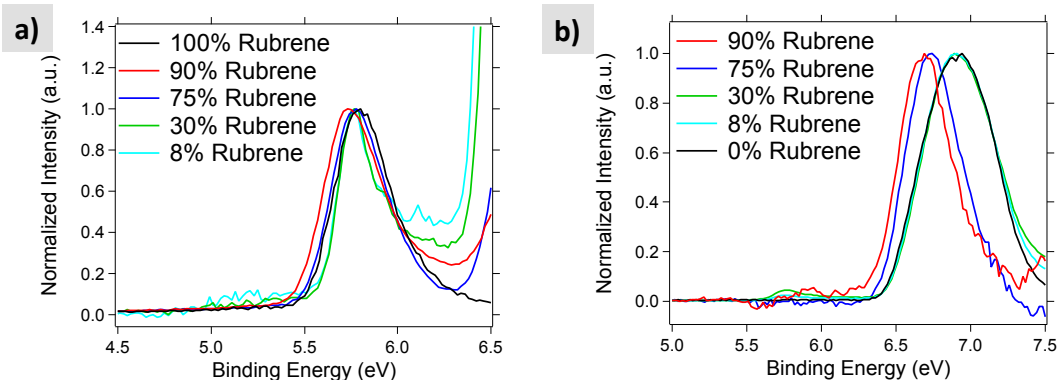

Figure 5.7: UPS spectra of the HOMO region for rubrene (a) and C_{60} (b) in films of varying rubrene:C_{60} blend composition with the binding energy adjusted to Evac=0. In b) the pure rubrene contribution for rubrene concentrations of $\geq$75% was subtracted from the blend.

5.5 Ground state bleaching at rubrene/C_{60} interface

Besides the shifts in the frontier orbitals of the donor and acceptor, interfacial molecular interactions may also alter their ground states. Through absorption measurements, evidence for such ground state bleaching can be obtained using carefully designed absorption measurements.[216] We would like to investigate how the absorption features for rubrene and C_{60} are influenced by the electronic interaction between a donor and an acceptor due the formation of the ground state charge transfer complex.

Based on the work of Schwarz et al.,[216] we have used bilayers of rubrene and fullerene made in two configurations to probe the dependence of the absorption of the rubrene/C_{60} bilayer. We compare the absorption of a bilayer film consisting of a 100nm rubrene layer on top of a 100nm fullerene layer on a quartz substrate, i.e. forming an interface (configuration I) and the absorption of the same layers now coated on both side of the substrate such that there is no physical contact between the two layers (configuration II) (Figure 5.11). In Figure 5.11 and 5.12, we show the absorption spectra of the pure rubrene and C_{60} films and the bilayers in configuration I and II respectively.

We compare the absorbance of rubrene/C_{60} bilayer prepared in configuration I with

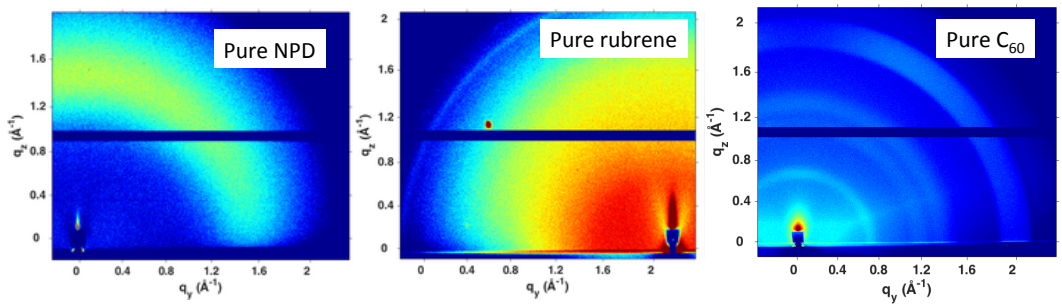

Figure 5.8: UPS spectra of the HOMO region for rubrene (a) and C_{60} (b) in films of varying rubrene:C_{60} blend composition with the binding energy adjusted to Evac=0. In b) the pure rubrene contribution for rubrene concentrations of $\geq$75% was subtracted from the blend.

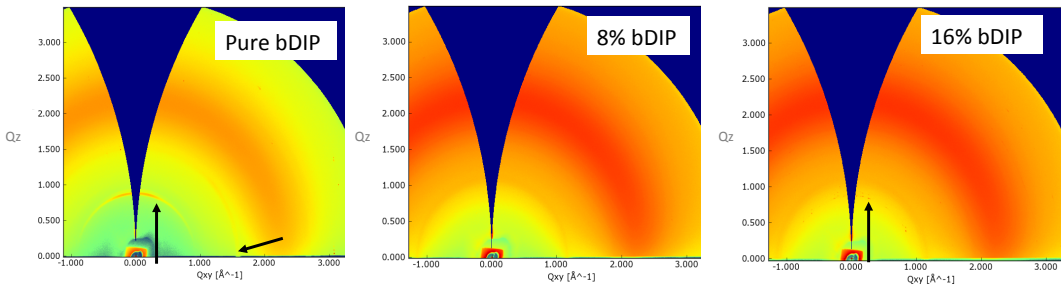

Figure 5.9: Grazing incidence wide-angle X-ray scattering spectra for pure films of bDIP:C_{60} blends. Black arrows in the bDIP spectra are included to show the diffraction peaks arising from bDIP.

that of the calculated absorbance of rubrene and C_{60} pure films absorbances. Rubrene/C_{60} bilayer based on algebraic sum of the absorbance. It appears that the sum of the absorbances differs from the absorbance of the bilayer in configuration I. Moreover, most of the difference can be assigned to the vibronic features of rubrene. This indicates that rubrene ground state is bleached when the bilayer is fabricated in configuration I. We repeat the same experiment with bilayers made in configuration II to verify whether the ground state bleach is absent when the rubrene and C_{60} layer are physically separated by the substrate and not interacting. In this case unfortunately (5.12), C_{60} absorption completes overwhelms absorbance from the rubrene layer which we attribute to a significant amount of scattering at high wavelengths in the C_{60} layer which

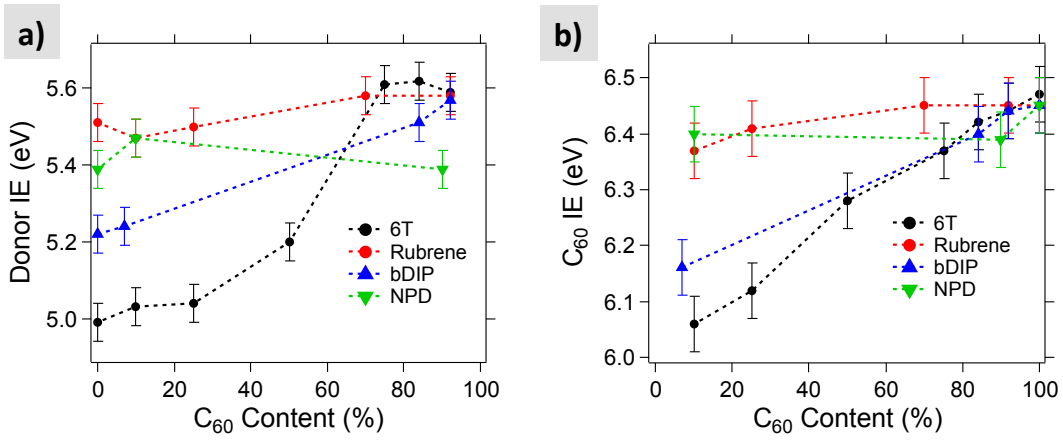

Figure 5.10: UPS measured IEs for the donor materials (a) and C_{60} (b) at varying compositions.

thus depletes the amount of light available for the C_{60} layer to be absorbed. Nevertheless, the results obtain from configuration I allow us to conclude of the ground state beaching of rubrene due to intermolecular interactions at the rubrene/C_{60} interface.

5.6 Impact of the energy landscape on PV device processes and performance

In addition to the IE, the CT state energy is critical in determining the operation of PV devices. The CT states can be thought of as the free carriers generation center in organic solar cells. As discussed in Chapter 2 CT states are the locus carriers recombination and exciton splitting and their energy and distribution primarily control the mechanistic of these two processes. Here, EQE measurements of the sub-bandgap region of PV devices provide further insight into the energy landscapes present in these material systems. The EQE measurements are shown in Figure 5.14 for 6T:C_{60} and Figure 5.15 for rubrene:C_{60} devices along with fits of the CT state absorbance bands and the extracted E_{CT} values for varying active layer architectures (bilayer vs. blend) and blend compositions of 6T:C_{60} (a,d) and rubrene:C_{60} (b). The CT states were fit, and the E_{CT} values extracted following the procedure presented in Chapter

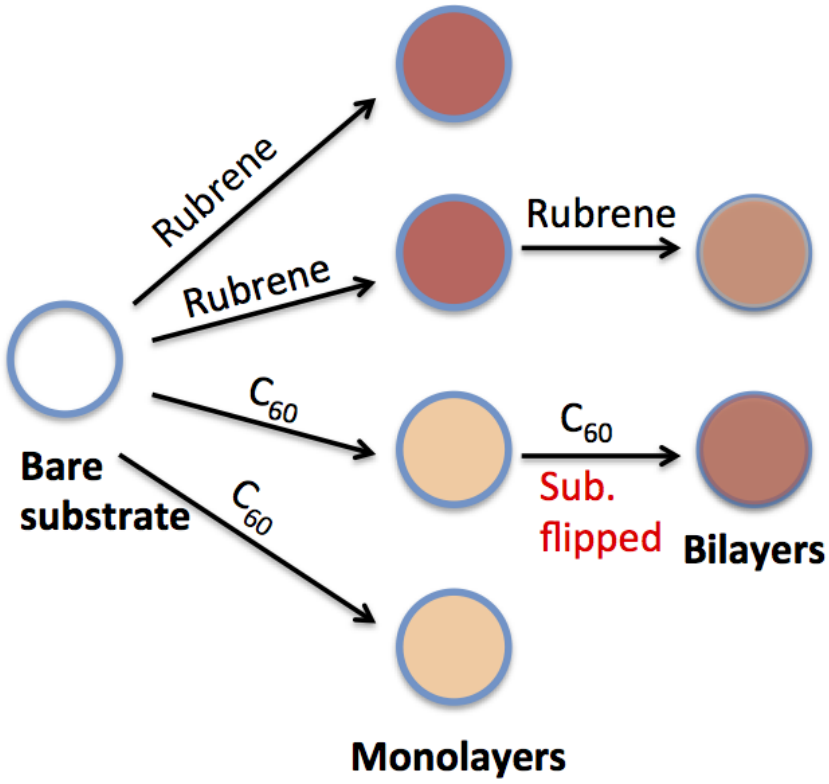

Figure 5.11: Scheme of the ground state bleaching at rubrene/C_{60} interface experiment: In configuration I the acceptor is evaporated on top of the polymer donor, in configuration II on the backside of the quartz substrate.

3. Figure 5.15b shows a comparison between the E_{CT} values and the transport gap (E_{TG}), where E_{TG} is the difference between the donor IE and acceptor EA. The acceptor EA is estimated based on the reported transport gap (IE-EA) of C_{60} (2.35 eV) and the UPS measured IEs,[217] though we note that it is entirely possible that the transport gap of C_{60} also changes as the IE changes. Figure 5.14a shows that E_{CT} of the 6T:C_{60} blends and bilayers differ by 0.50 eV. This variation is in agreement with the measured IEs, where the IE of 6T varies by 0.6 eV depending on composition. By contrast, the CT state energies for rubrene:C_{60} blends and bilayers differ by only 0.04 eV. Focusing on the shifts in E_{CT} displayed for 6T:C_{60}, E_{CT} increases by 0.17 eV in going from the bilayer device to the 9:1 6T:C_{60} blend. This shift is primarily

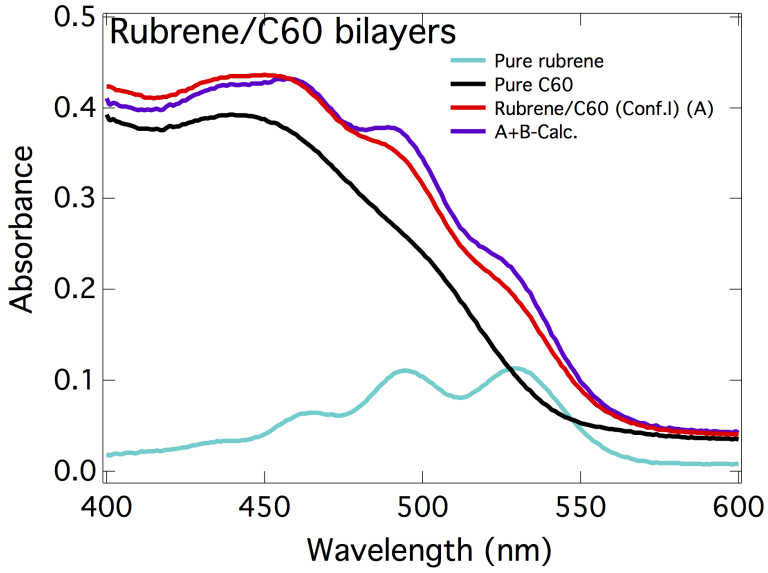

Figure 5.12: Absorption spectra of 100nm pure rubrene, 100nm pure C_{60} and rubrene/C_{60} bilayer prepared in configuration I. The sum of the 100 nm pure rubrene and 100nm pure C_{60} absorbance is also shown.

attributed to the change in the EA of C_{60}, as the IE of 6T only changes by 0.04 eV (Figure 5.14a) between pure 6T and 9:1 6T:C_{60} blends. Moving from the 9:1 to 1:3 and 1:9 6T:C_{60} blends gives rise to further E_{CT} increases of 0.30 and 0.33 eV, respectively, which are primarily attributed to the change in the IE of 6T. Figure 5.15b shows that ETG agrees reasonably well with E_{CT} values for 6T:C_{60} and rubrene:C_{60} at varying blend ratios, which would be predicted based on the assumption that E_{CT} is related to the difference between the donor IE and fullerene EA.

Interestingly, Figure 5.14b shows that EQE measurements on the 1:1 6T:C_{60} blend clearly show the presence of more than one CT band. Here, the CT region of the EQE spectrum is best fit with a combination of the bilayer, 9:1, and 1:9 CT bands. The contributions of these individual CT bands and the total fit is shown in Figure 5.14b by the dashed lines. What this indicates is that in the 1:1 blend there are interfaces between pure 6T and pure C_{60} regions, regions that are C_{60} rich, and regions that are 6T rich. This complex morphology is comparable to that of bulk-heterojunction

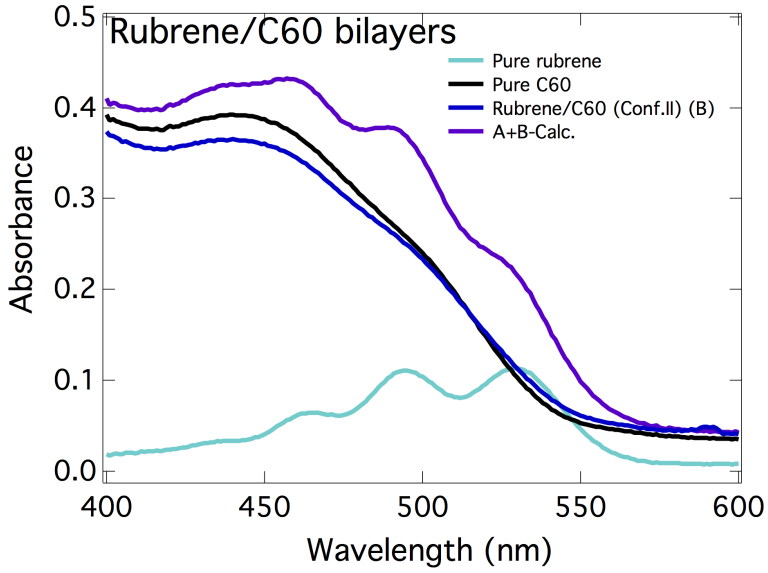

Figure 5.13: Absorption spectra of 100nm pure rubrene, 100nm pure C_{60} and rubrene/C_{60} bilayer prepared in configuration II. The sum of the 100 nm pure rubrene and 100nm pure C_{60} absorbance is also shown.

(BHJ) PV material systems and has important implications for determining the PV performance. The energy diagrams constructed from the UPS measurements and from the measurements of E_{CT} for the 6T:C_{60} material systems are presented in Figure 5.16. In the case of 6T, which is likely a good model for many crystalline and semi-crystalline small molecules and polymers, there is an energy landscape that is favorable for charge separation in nearly every aspect. For example, as shown in Figure 5.16, an electron in a region with a low fullerene concentration will be energetically driven towards regions of increasing fullerene concentration, and vice versa for a hole in a low 6T region. This is an ideal energy landscape, as opposite charge-carriers are driven away from each other towards regions where there are successively less of the opposite charge-carrier, and thus non-geminate recombination rates should be reduced.

Another way of looking at the energy landscape is through examination of the energy levels of the CT states. Here, the CT state energy is lowest for a pure C_{60}-pure 6T

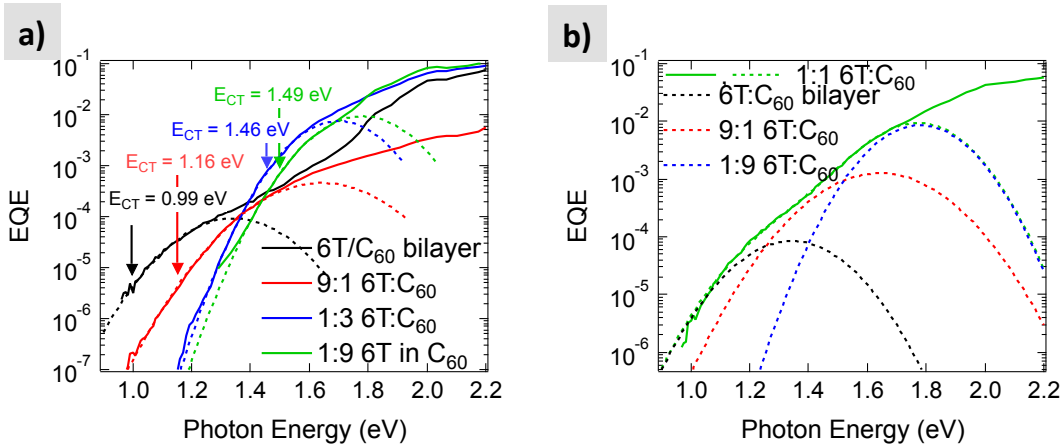

Figure 5.14: EQE of the CT region for 6T:C_{60} (a) PV devices of varying architecture and blend composition. Fits to the CT region are shown with dashed lines and E_{CT} values indicated on the plots. (b) CT state region of the EQE spectra for a 1:1 6T:C_{60} blend and the fit to a sum of the bilayer, 9:1, and 1:9 6T:C_{60} CT states (dashed lines).

interface and higher for the mixed regions. In a BHJ PV device with all 3 phases present, CT excitons will preferentially migrate to the pure interfaces as depicted in Figure 5.17 and this will have strong implications regarding device performance. Recent work, [20] has shown that for conditions that are close to actual device operation, CT states are in equilibrium with free carriers. Thus, the CT states have the same temperature with the free carriers and consequently free carriers are likely to populate the lower energy CT states more than, the higher energy CT states. At these interfaces between the pure donor and pure acceptor, it is likely that charge-separation is more efficient. This more efficient separation is predicted on the basis of both increased local mobility in these aggregated regions and increased charge delocalization that will result in lower CT state binding energies.[47, 214, 218, 219] Therefore, the energy landscapes in 6T:C_{60} blends appear ideal for enhancing the driving force for charge separation and decreasing the probability for bimolecular recombination. However as discussed in chapter 1 the low energy of aggregate-aggregate CT state would lead to low V_{OC}. A potentially more promising alternative is to create a system where there is never a clean interface between the aggregates, i.e. the

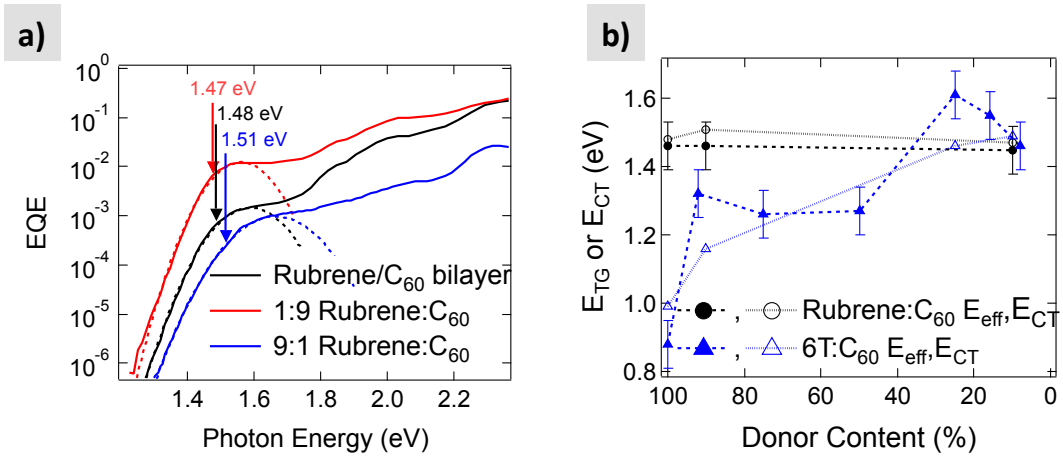

Figure 5.15: EQE of the CT region for rubrene:C_{60} (a) PV devices of varying architecture and blend composition. Fits to the CT region are shown with dashed lines and E_{CT} values indicated on the plots. (b) E_{TG} calculated from the donor IE C_{60} EA difference and measured E_{CT} values for varying donor content.

aggregate regions are always separated by a disordered or mixed phase. If the energy of a free hole and free electron in aggregate donor and acceptor regions, respectively, is lower than when an electron and hole are in a CT state in the mixed region, then the CT state binding energy is non-existent (i.e. the combined energy of the free carriers is lower than that of the bound pair). In this scenario charge separation rates will be high while the V_{OC} can also be high, as the V_{OC} is largely limited by the lowest energy CT states present. A system with such an energy landscape appears to be that of bDIP:C_{60}.[220] The pure film of bDIP shows an IE of 5.22 eV, whereas bDIP displays an IE of 5.50 and 5.56 eV in the mixed films with 16 and 8% bDIP, respectively. Furthermore, C_{60} has an IE of 6.16 eV in 90% bDIP vs. 6.45 eV for pure C_{60}. From these measurements we would expect that E_{CT} would increase by ca. 0.3 eV in going from a bilayer to a 1:9 bDIP:C_{60} film. Instead, Figure 5.18 shows that E_{CT} changes by only 0.04 eV between the bilayer and the 1:9 blend. Furthermore, E_{CT} ranges from 1.4 to 1.44 eV, which is closer to the range for a donor material with an IE of 5.5 eV than to a donor with a 5.2 eV IE (e.g. rubrene has

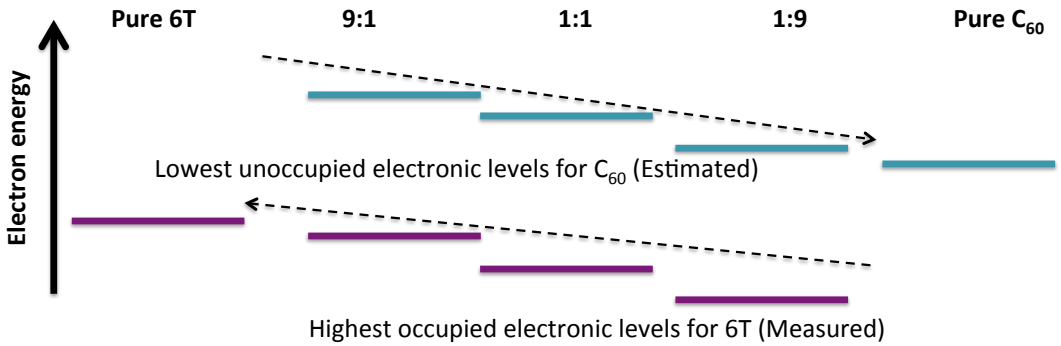

Figure 5.16: Simplified energy level schematic for 6T:C_{60} blends as a function of composition showing the relative C_{60} lowest unoccupied electronic levels and 6T highest occupied electronic levels. The cascade structure of the energy levels between the mixed and pure phases creates a driving force for exciton separation.

an IE of 5.51 and E_{CT} in a rubrene/C_{60} bilayer device is 1.48 eV). This combination suggests that the low energy bDIP aggregate-C_{60} aggregate CT state is not formed. If this aggregate-aggregate CT state is not formed, it would mean that significant intermixing is occurring at the bDIP-C_{60} interface. Formation of a mixed interface is supported by recently published neutron scattering experiments that show indeed a mixed interface is formed.[220] We further investigated the formation of this mixed interface and observed that spontaneous mixing between C_{60} and bDIP occurs at temperatures of >0 °C. To probe this interfacial mixing we deposited a 10 nm layer of C_{60} on top of a bDIP layer at -100 °C and continually monitored the presence of the F 1s peak using X-ray photoelectron spectroscopy (XPS) as the stage was left to heat up to room temperature. As Figure 5.19 shows, initially a pure C_{60} layer is present on top of the bDIP layer and thus no F 1s signal is observed (-100 °C spectrum). As the film warms to 0 °C, the F 1s peak from bDIP begins to appear. This peak increases in intensity as the film warms further to 20 °C. This data indicates that there is a significant driving force for mixing between C_{60} and bDIP to occur, and as such it is reasonable that there would not exist any clean interfaces between pure bDIP and pure C_{60} phases.

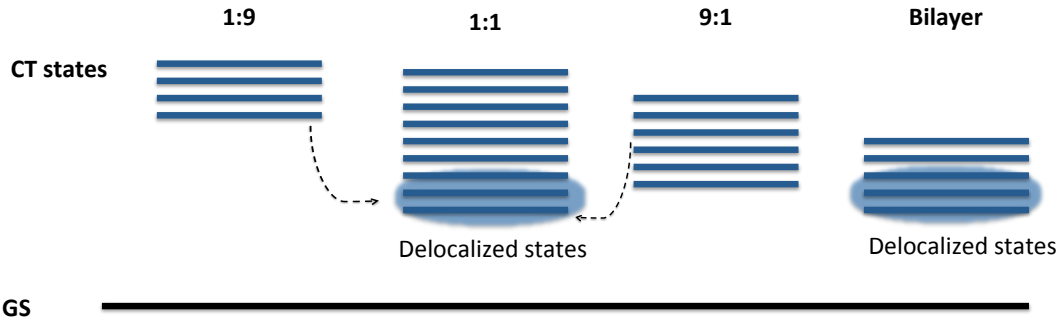

Figure 5.17: Relative CT state energies for 6T:C_{60} blends as a function of composition. GS is the ground state. Delocalized CT states arising at the interface formed by pure donor and C_{60} are the lowest in energy and therefore more likely to be occupied by the CT excitons. They are expected to lead to efficient exciton separation, but their low energy would impede a high V_{OC}.

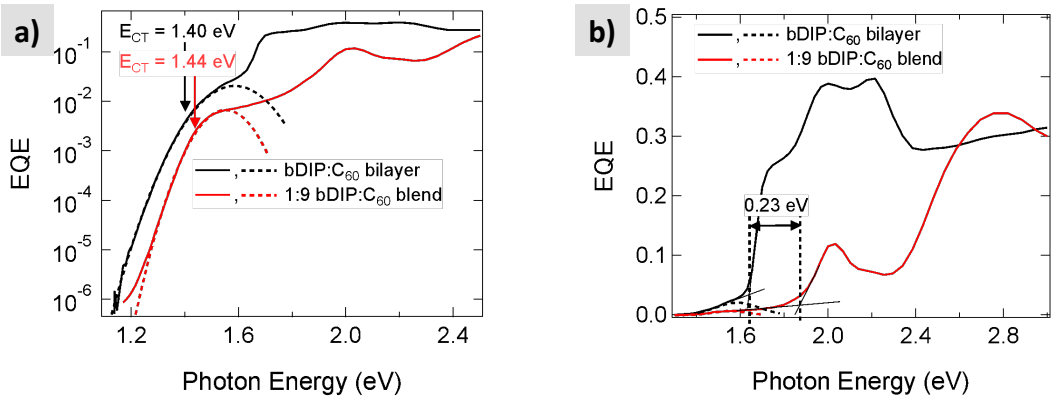

Figure 5.18: EQE of the CT region for bDIP:C_{60} PV devices of varying composition on a logarithmic (a) and linear (b) scale.

The above gap region of the EQE spectra for the bDIP:C_{60} bilayer and blend, as shown in Figure 5.18b, does show a significant shift in the bDIP absorbance edge of 0.23 eV. Most likely this shift arises due to the lack of crystallinity of bDIP in the 1:9 blend, as supported by the X-ray diffraction data shown in Figure 5.9. Despite this shift in the above gap absorbance, there is only a 0.04 eV shift in the CT state energy. Thus, the bilayer system is extending the primary absorbance of the material over that of the blend system with minimal sacrifices in E_{CT}. Controlling the interfacial morphology may therefore provide a general means to extend the absorbance range of

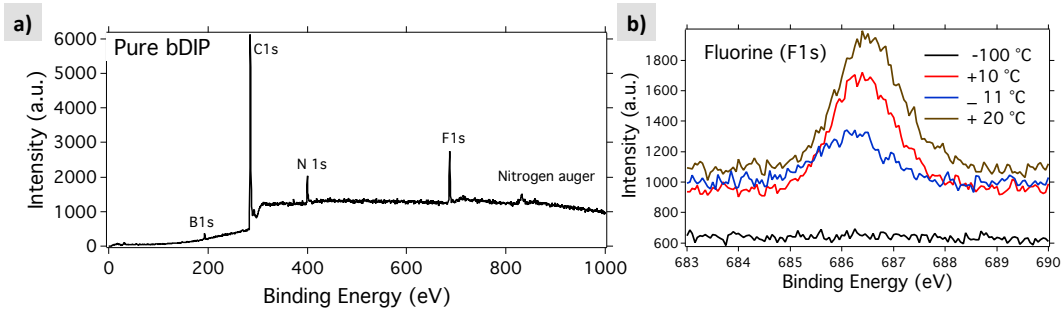

Figure 5.19: XPS data of the F 1s region for a bDIP/C_{60} bilayer with a 10 nm C_{60} layer that was deposited at -100 °C. As the film is warmed to room temperature the F 1s signal from bDIP becomes apparent, indicating that bDIP is diffusing into the C_{60} layer.

PV material systems without sacrificing the V_{OC}. This formation of mixed interfaces is likely a common factor influencing device performance, as supported by both experimental and computational studies on a range of PV materials,[50, 188, 221] and the energy offsets in these PV systems may significantly increase the probability of charge separation.

5.7 Comparing intermixing in bDIP and other materials systems

We have performed a comparative study of the degree of interfacial mixing in several bilayer systems using UPS. As with XPS, we looked at the attenuation the HOMO feature from a pure donor film (20nm) as the thickness of C_{60} overlayer was increased. Comparing the attenuation trends as shown on a logscale in Figure 5.20 we find that face-on ZnPc and bDIP have the strongest tendency to mix with C_{60}. Tetracene and both amorphous and crystalline rubrene tendency to intermix are significantly low compared to bDIP and face-on ZnPc. We have also performed the experiment whereby the ZnPc underlayer is deposited on HOPG and its thickness limited to only 4nm. The limited thickness of the underlayer sets a limit on the extent of the mixed layer. The attenuation of C_{60}, in this case, exhibits the slowest decay with

C_{60}. This suggests that it is likely that for most of the systems, intermixing with C_{60} occurs within a thickness that exceeds several donor monolayers. However, we note that without the exact knowledge of the electron mean free path in these materials it is hard to conclude on the exact thickness of the mixed layer. Nevertheless, the data show that such studies could serve to effectively probe interfacial mixing at least qualitatively.

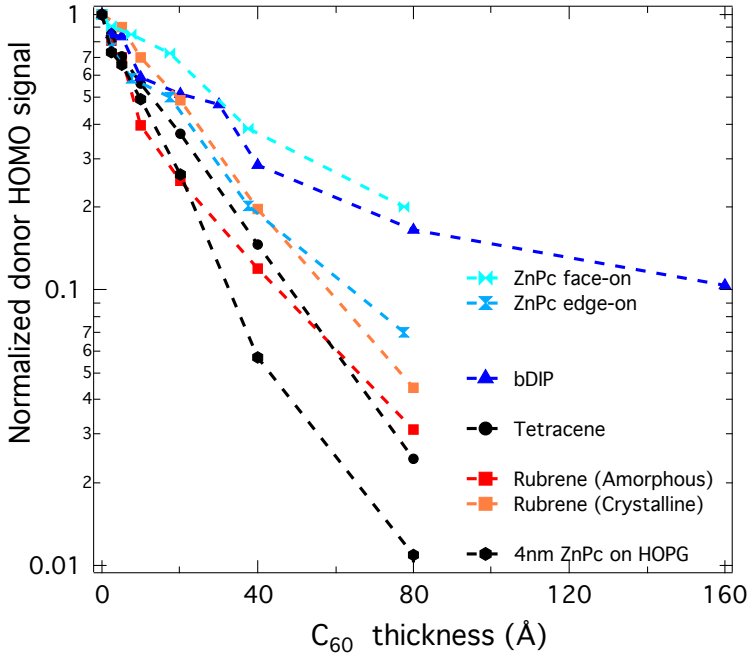

Figure 5.20: Attenuation of the HOMO signal with C_{60} thickness for small molecules studied in this work.

5.8 Conclusions

To sum up, the energy landscape in organic donor-acceptor blends is intricately related to the molecular structure and composition of the blends. Both the energy levels of the donor and the acceptor varies significantly with the extent of order and the composition for some materials combinations, while for others materials blends, the energy levels only shift marginally with both the degree of order and composition.

The observed energy levels shifts as a function of the composition are found to arise from materials polarization. In specifics, for the 6T:C_{60} blends, the significant shifts in IE of 6T is large enough to overcome the CT binding energy and would provide a strong driving force for bound charges to separate into free carriers. Measurements of the charge transfer state energy E_{CT}, reveals that E_{CT} and by extension Voc is highly dependent on the extent of intermolecular interactions, and on whether mixed interfaces or clean interfaces, were present between aggregated regions. Altogether, the study shows the significance of molecular interactions and conformation for interfacial PV processes and how materials properties primarily control their efficiency. It appears that the formation of mixed phases at all donor-acceptor interfaces is effective to minimize or vanish CT state binding energies without limiting Voc.

Chapter 6

The Impacts of Donor Semi-Crystallinity and Coexistence of Multiple Interfacial Charge Transfer Bands

6.1 Introduction

In Chapter 5 we discussed the crucial role of molecular conformation and interactions in determining materials energy states in organic photovoltaics. We arrived at the conclusion that in a bulk heterojunction, material phases with different degree of order in the donor or the acceptor coexist. We found that the presence of this various materials phases gave rise to various CT state energies and we discussed how among these CT states the low energy CT states were primarily the limiting factor for Voc. In this chapter, we conduct an in-depth study on the impact of structural heterogeneities, such as the coexistence of crystalline and amorphous phases, on the distribution of CT states and the Voc. We assess the impact of semicrystallinity of the donor material on the CT manifold and the resulting Voc by recreating model donor-acceptor interfaces with a donor molecule exhibiting different degrees of crystallinity and packing structures. To do so, we utilize vacuum-sublimed rubrene films, deposited amorphous and subsequently crystallized prior to deposition of C_{60}. We find that the microstructures present in the rubrene film yield a commensurate distribution of CT state bands instead of just one CT state band. These microstructures control the population of the CT states at the planar D-A interface and correspondingly change the Voc. The observed Voc loss is attributed to the presence of the lower CT state associated to the presence of crystalline rubrene/C_{60} at the D-A interface.

We find that the E_{CT} present at the interface between crystalline rubrene and C_{60} can be as much as ca. 400 meV lower relative to E_{CT} at the amorphous rubrene and C_{60} interface. Such low-lying CT states are shown to be responsible for Voc loss by as much as 0.3 V in solar cells.

It appears imperative to prevent such Voc loss. One effective strategy to prevent such Voc loss is to implement interfacial structural control that inhibits the formation of low energy materials phases, for instance by favoring an invariable formation of an interfacial mixed phase as means of raising E_{CT} and thus Voc in organic solar cells.

6.2 Structural order in rubrene thin films

Rubrene (chemical structure shown in Figure 6.1a) is selected as the donor and C_{60} was chosen as the acceptor (chemical structure shown in Figure 6.1b) as it has been shown to form rather abrupt interfaces with rubrene thanks to the low tendency of the latter to intermix with C_{60}.[46] We have fabricated rubrene thin films with a wide range of structural order and textures. We exploit the fact that crystalline rubrene thin films form several polymorphs in the monoclinic, triclinic and orthorhombic crystal structures, which can be easily accessed by thermal annealing of the as-deposited amorphous film. In addition, the extent of crystallinity of the film can be tuned by varying the duration of thermal annealing. Three types of rubrene samples, namely amorphous rubrene (a-rubrene), triclinic rubrene (t-rubrene), and orthorhombic rubrene (o-rubrene) were fabricated. The a-rubrene was obtained as deposited. The t-rubrene was obtained by annealing the a-rubrene film at 150 °C for 120s while the o-rubrene was obtained by annealing the a-rubrene at 170 °C for 300s.

We verify the structure of these rubrene films using grazing-incidence wide-angle x-ray scattering (GIWAXS). The scattering patterns for 50 nm-thick films are shown in Figure 6.2. The as-deposited rubrene film exhibits no diffraction peak (Figure 6.2a) confirming its amorphous nature. The film annealed at 150 °C (Figure 6.2b) exhibits

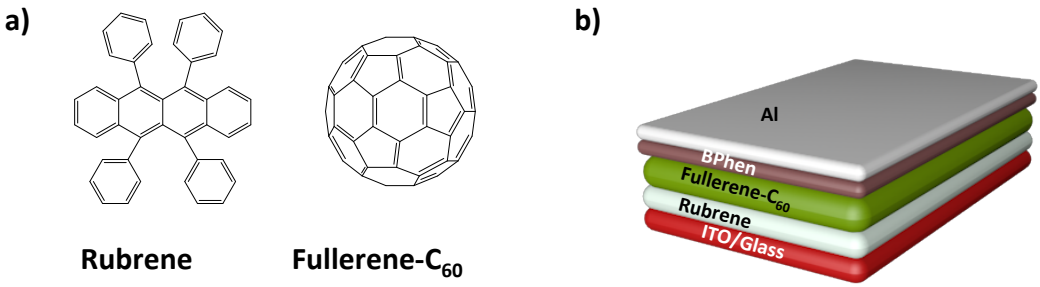

Figure 6.1: (a) Chemical structures of rubrene and fullerene-C_{60}. (b) Schematic illustration of the bilayer device structure.

a diffraction pattern featuring two overlapping peaks, (100) & $(10\bar{1})$, in the out-of-plane direction (q_z direction) with a scattering vector amplitude of ~0.870 $Å^{-1}$ which is consistent with a triclinic phase of rubrene (P-1), lattice parameters of a = 7.01 Å, b = 8.54 Å, c = 11.95 Å, $\alpha = 97.5°$, $\beta = 104.7°$, and $\gamma = 98.8°$.[222] The pattern also suggests that the film is textured with the oriented crystalline domains having their a-axis perpendicular to the substrate. In contrast, for the film annealed at 170 °C, the pattern appears to exhibit very sharp diffraction peaks in all crystallographic directions indicative of extended long range order in the film. The (002) diffraction peak with a q value of 0.474 $Å^{-1}$ appearing in the out-of-plane direction shows that the highly oriented crystallites are formed in the orthorhombic phase (Cmca), with lattice parameters of a = 14.21 Å, b = 7.17 Åand c = 26.78 Å, $\alpha = \beta = \gamma = 90°$,[222] with their c-axis oriented normal to the substrate. We also note the presence of relatively weak peaks associated with the triclinic rubrene phase in the film annealed at 170 °C. These results show that the rubrene films annealed at 150 °C or 170 °C exhibit differences in the crystalline phase (polymorphism) and the degree of order in agreement with other findings in the literature.[223, 224] In addition, their surface termination differs markedly as indicated by their texture. In the absence of surface rearrangements, the film with the triclinic phase terminates with the tilted molecule with its aromatic core exposed (Figure 6.2e) whereas for the film in the orthorhombic

phase, the rubrene molecules are oriented side-on with only their phenyl rings exposed (Figure 6.2f). It is worth noting that other studies have found, through NEXFAS experiments, that the orientation of rubrene molecules at the surface of amorphous films is not completely random but instead exhibits a dominant conformation with the aromatic core exposed on average at the surface of the film (Figure 6.2d).[46, 105] These differences in crystallinity, polymorphism, texture and conformation are thus expected to translate into significantly different surface terminations with which the rubrene-C_{60} buried interface will form.

The evolution of the molecular structure of the rubrene thin films with annealing temperature was also investigated by comparing a larger series of samples annealed at various temperatures and times as shown in Figure 6.3. The comparison of the GIWAXS patterns further confirms that the rubrene film crystallinity increases with annealing temperature and time.

6.3 Influence of structural order in rubrene thin films on the distribution of CT states

The successful fabrication of structurally distinct thin films of rubrene ranging from amorphous to polycrystalline with two different polymorphs and textures, has made it possible to investigate how the structural differences in the donor influence the operation of organic solar cells, their Voc and the energetics of the D-A interface. We have fabricated bilayer solar cells using a-rubrene, t-rubrene and o-rubrene as the donors, and C_{60} as the acceptor (Glass/ITO-150nm/rubrene-50nm/C_{60}-50nm/Bphen-12nm/Al-100nm, Figure 6.1b). As rubrene layers can exhibit pinholes and cracks upon annealing, which can impede device operation,[122, 224] we deposited a partial monolayer (0.5 nm) of copper iodide (CuI) on ITO. The CuI layer, which has been shown to act as an effective seed layer for the growth of several organic donors,[225–227] had the benefit of maintaining the continuity of the rubrene films even after

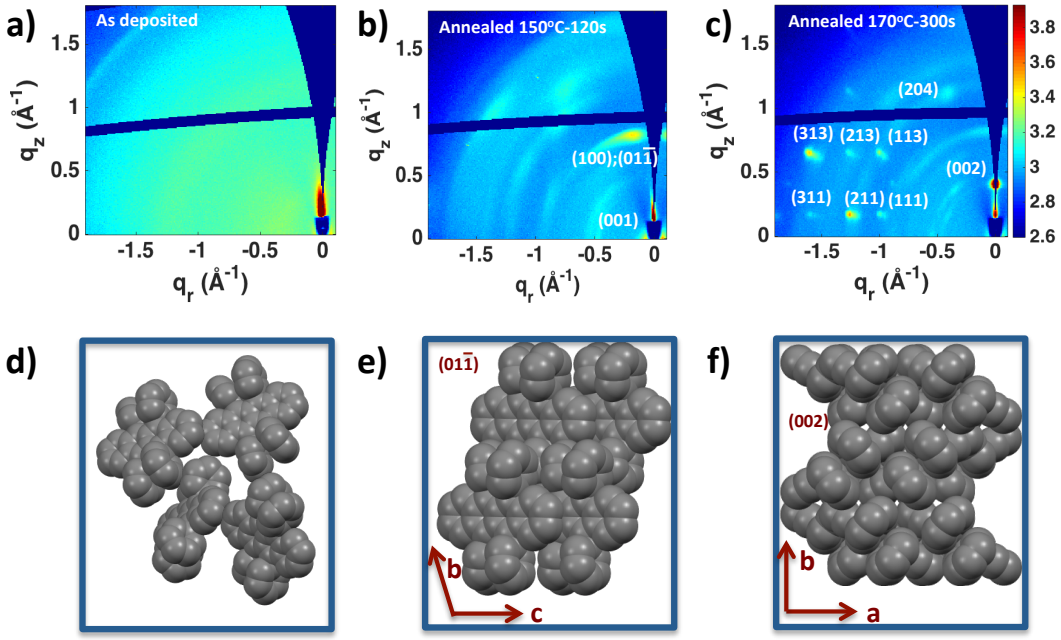

Figure 6.2: Top: Two-dimensional GIWAXS patterns of 50 nm-thick rubrene films on ITO/glass substrates for the as-deposited a-rubrene film (a), t-rubrene film annealed at 150 °C for 120 s (b), and o-rubrene film annealed at 170 °C for 300 s (c). Bottom: Illustrations of the molecular structure near the surface of thin films of a-rubrene (d), t-rubrene (e), and o-rubrene (f). The molecular packing in a-rubrene films is shown to have an average orientation exposing the acene core of the molecules, in agreement with previous measurements.[33,38] The textured t-rubrene film exposes the (01$\bar{1}$) plane of the triclinic system, placing the acene cores at the film surface. The textured o-rubrene film exposes the (002) plane, placing the side phenyl rings of rubrene at the surface while the acene core is less accessible.

crystallization. In Figures 6.4c, 6.1d and Table 6.1, we summarize the current-voltage (J-V) characteristics and associated figures of merit of the rubrene/C_{60} bilayer devices. The open circuit voltage (Voc), as extracted from current-voltage characteristics of the bilayer devices (Table 6.1), drops substantially by 170 mV in going from the BL device with a-rubrene to that with t-rubrene. A further drop of 140 mV is observed in going from the device with t-rubrene to that with o-rubrene. The fill factor (FF) and the short circuit current density (Jsc) vary marginally. The decrease in Voc with annealing the donor is consistent with previous reports [122] using thicker films.

As the BHJ solar cell represents the most common architecture of organic solar cells,

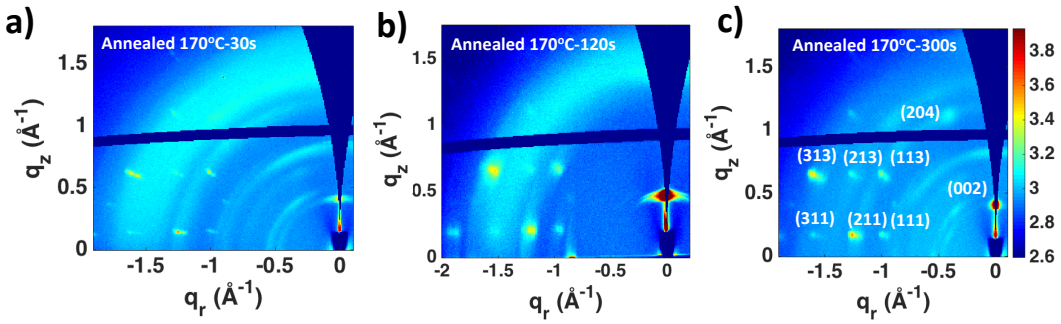

Figure 6.3: 2D GIWAXS patterns of 50 nm-thick annealed rubrene films on ITO (a) 170 °C for 30s (b) 170 °C for 120s and (c) 170 °C for 300s. The patterns indicate that the rubrene films become more textured as the annealing temperature is increased and when they are annealed for longer times. At 170 °C, mainly larger and uniaxially oriented crystals are formed.

we have also fabricated a bulk heterojunction (BHJ) device (glass/ITO-150nm/rubrene-50nm:C_{60}(1:1)-60nm/ C60-10nm /Bphen-12nm/Al-100nm) through co-deposition of rubrene and C_{60} without additional annealing. As expected, the BHJ layer exhibits lower FF and Jsc than the BL devices (Table 6.1), as a result of lack of aggregation and phase separation of the blend, but it exhibits an identical Voc to that of BL devices using a-rubrene. This strongly indicates that the a-rubrene/ C_{60} interface in BL devices can successfully emulate the nature of the D-A interface in BHJ devices of the same material. On the other hand, our efforts to anneal the BHJ layer to crystallize the rubrene phase have failed to yield working devices, preventing further direct comparisons between BL and BHJ devices at this time. The significant drop in Voc in BL devices exhibiting different structures of rubrene points to changes in energetics at the rubrene/C_{60} interface. Voc is specifically related to the energy of the charge transfer states, E_{CT}, at the donor acceptor interface.[45, 46, 166] A very effective means of measuring the densities and the energies of charge transfer states is to perform sensitive external quantum efficiency (EQE) measurements to detect the sub-gap photovoltaic response of the solar cells. These measurements rely on the excitation of interfacial CT complexes by direct optical transition with a spectrally

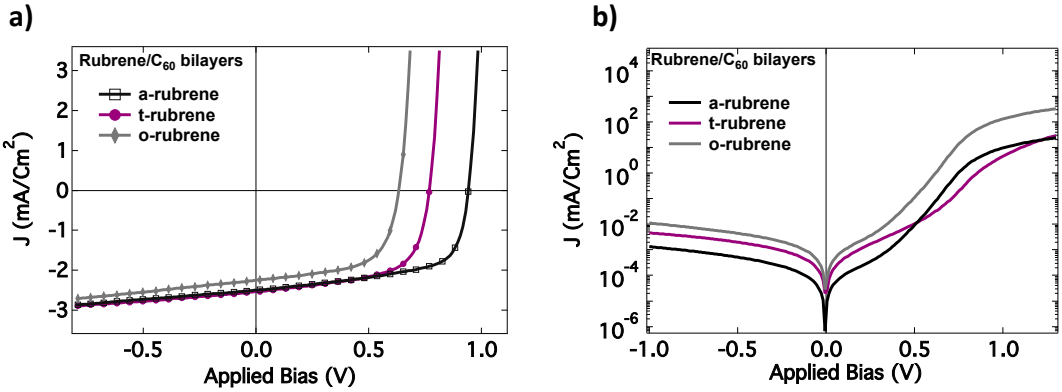

Figure 6.4: (a) Illuminated and (b) dark J-V characteristics of rubrene/ C_{60} bilayer devices made with amorphous (a-rubrene) and partially crystallized rubrene films (t/o-rubrene).

resolved light source. Utilizing Marcus theory to model the absorbance of these D-A complexes, the subgap portion of the EQE spectrum of the device can be modelled as in Equation 4.1,[45] and E_{CT}, λ and f can be obtained by fitting Equation 4.1 to the subgap region of the EQE spectrum.

Table 6.1: Annealing time, open-circuit voltage (Voc), fill factor (FF), short-circuit current density (Jsc), integrated external quantum efficiency (EQE) signal and power conversion efficiency (PCE) for rubrene/C_{60} BL and BHJ devices tested under 100 mW/cm2 simulated AM1.5 irradiation.

Description	**a-rubrene (BL)**	**t-rubrene (BL)**	**o-rubrene (BL)**	**a-rubrene (BHJ)**
Annealing time (s)	0	120	300	0
Voc [V]	0.94 ± 0.03	0.77 ± 0.06	0.63 ± 0.02	0.92 ± 0.05
FF [%]	62.7 ± 0.3	62 ± 0.15	61.20 ± 0.05	22.7 ± 0.5
Jsc [mA/cm2]	2.50 ± 0.03	2.54 ± 0.05	2.25 ± 0.03	1.050 ± 0.02
Integrated EQE	2.55	2.50	2.10	0.95
PCE [%]	1.47 ± 0.02	1.21 ± 0.01	0.90 ± 0.03	0.2 ± 0.02

In Figures 6.6a and 6.6b, we show the measured EQE spectra of the rubrene/C_{60} BL and BHJ devices with corresponding fits, plotted on a logarithmic scale to highlight

absorption features in the subgap region of the spectra (1 to 2 eV). The subgap absorption features are associated with interfacial charge-transfer states.[228] In the case of the BL and BHJ devices with an a-rubrene film, a single CT band is visible at 1.48 eV. As the rubrene film crystallizes, a clear and distinct CT band emerges at a spectral position lower in energy (1.23 eV for t-rubrene and 1.1 eV for o-rubrene) while the CT band at the spectral position of the purely amorphous case remains, decreasing in prominence. This indicates that annealing the rubrene films at 150°C or 170°C to produce the triclinic and orthorhombic phases, respectively, has the effect of modifying part of the D-A interface, making it energetically distinct from the starting interface with a-rubrene.

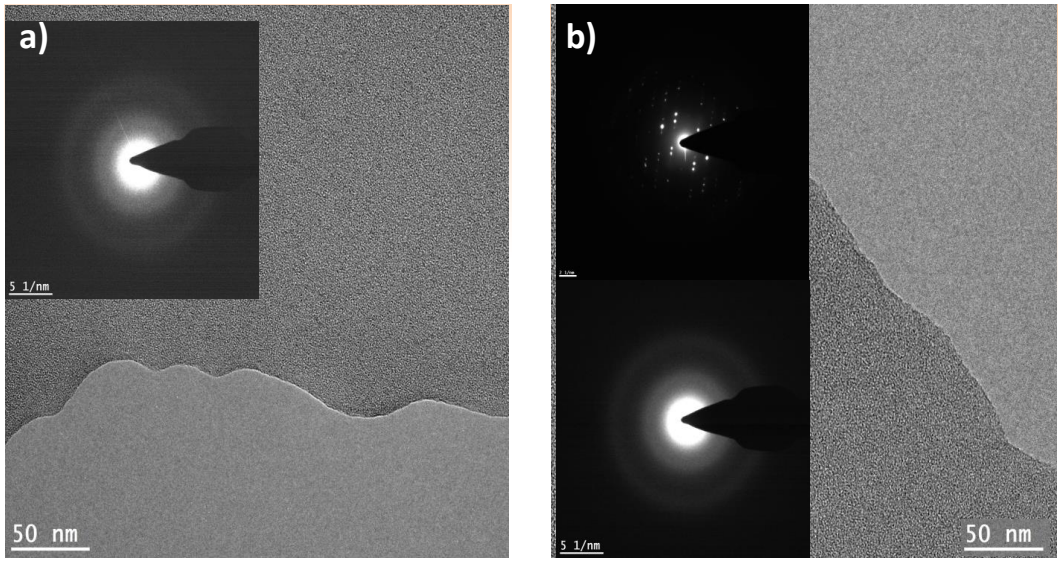

Figure 6.5: TEM micrographs and selected area diffraction patterns for 50-nm amorphous and annealed rubrene thin films. (a) Amorphous rubrene exhibiting domains with short range order. (b) Annealed ruberne exhibiting domains with both short and long range order.

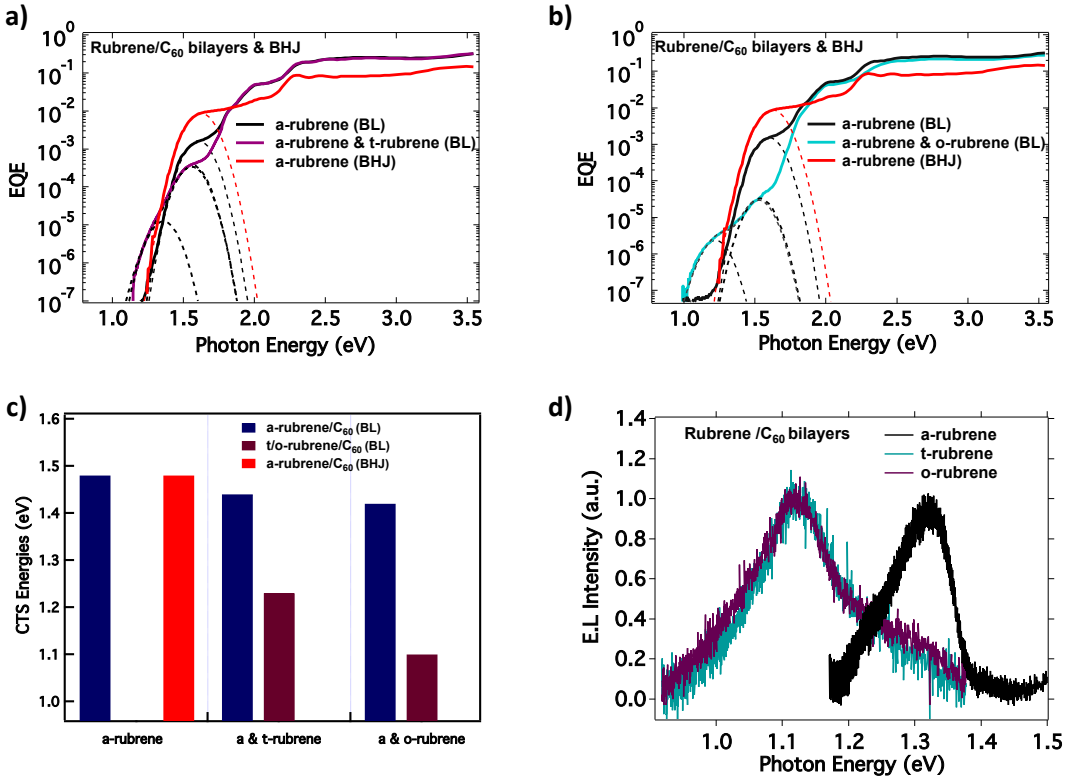

Figure 6.6: (a, b) Sub-gap EQE spectra collected on bilayer devices fabricated with as-deposited and annealed rubrene layers. The spectra are shown on a logarithmic scale, to highlight the CT bands in the sub-gap region. In the case of as-deposited rubrene only a single CT band is visible. In the cases of annealed rubrene (t/o-rubrene), a second band clearly appears at significantly lower energy in addition to the CT band at high energy. The dotted lines indicate fits of equation 1 to the CT bands. c) CT energies extracted from a) and b) for the high and low energy bands. d) Electroluminescence spectra of rubrene/ C_{60} bilayers. The spectral position of the emission peak of the CT state of the devices with annealed rubrene appears to be independent of the annealing temperature of rubrene but red shifted by 0.22 eV with respect to the CT peak in the device with amorphous rubrene, confirming that predominantly low-lying CT states with energy 1.1 eV are present in the bilayers with annealed rubrene.

In Figure 6.6c, we show the values of E_{CT} extracted from the fits of the CT bands in the form of a bar graph. The spectral positions of all the CT bands in the spectra remain roughly invariant, with the CT bands associated to the t-rubrene/C_{60} and the o-rubrene/C_{60} interfaces appearing only in samples annealed at 150 °C and 170 °C, respectively. It is reasonable to attribute these low energy CT peaks to the t-

rubrene/C_{60} and o-rubrene/C_{60} interfaces since a significant portion of the rubrene film surface is expected to be made of the ordered rubrene phases present in the bulk of the film (Figure 6.5).[122, 229] The presence of the prominent CT band at high energy indicates a substantial fraction of rubrene remains amorphous especially near the D-A interface. This interpretation is further supported by the decrease in the strength of the same CT bands with increased annealing time of the t-rubrene and o-rubrene layers (Figure 6.7).

An independent approach to gain insight into the interfacial energy landscape is through electroluminescence (EL) measurements. EL has been used as a thermodynamic indicator of the available open circuit voltage in organic solar cells.[228, 230] The EL spectra of all rubrene/C_{60} bilayers were measured in order to independently determine the energy of the CT states. As shown in Figure 6.6d, for all devices, a CT state emission was detected in the near infrared region. For the device made with amorphous rubrene, the CT state emission appears at $\sim$1.32 eV. Upon annealing of the rubrene layer, we observe an invariable redshift of all CT emissions to $\sim$1.1 eV. In the devices with annealed rubrene, the amorphous rubrene phase present at the interface has no CT emission due in part to preferential population of the lower energy CT states. It has been observed in single crystal rubrene that although such low volume fraction amorphous inclusions play an important role in photophysical processes such as bulk photoluminescence, they have little influence on hole transport.[133] If we make the plausible assumption that holes are only transported through the low energy crystalline phase, their energy in this phase would thus determine where CT emission occurs at the interface. CT emission at $\sim$1.1 eV is therefore in agreement with EQE data and further substantiates the presence of low-lying CT states in the crystalline films.

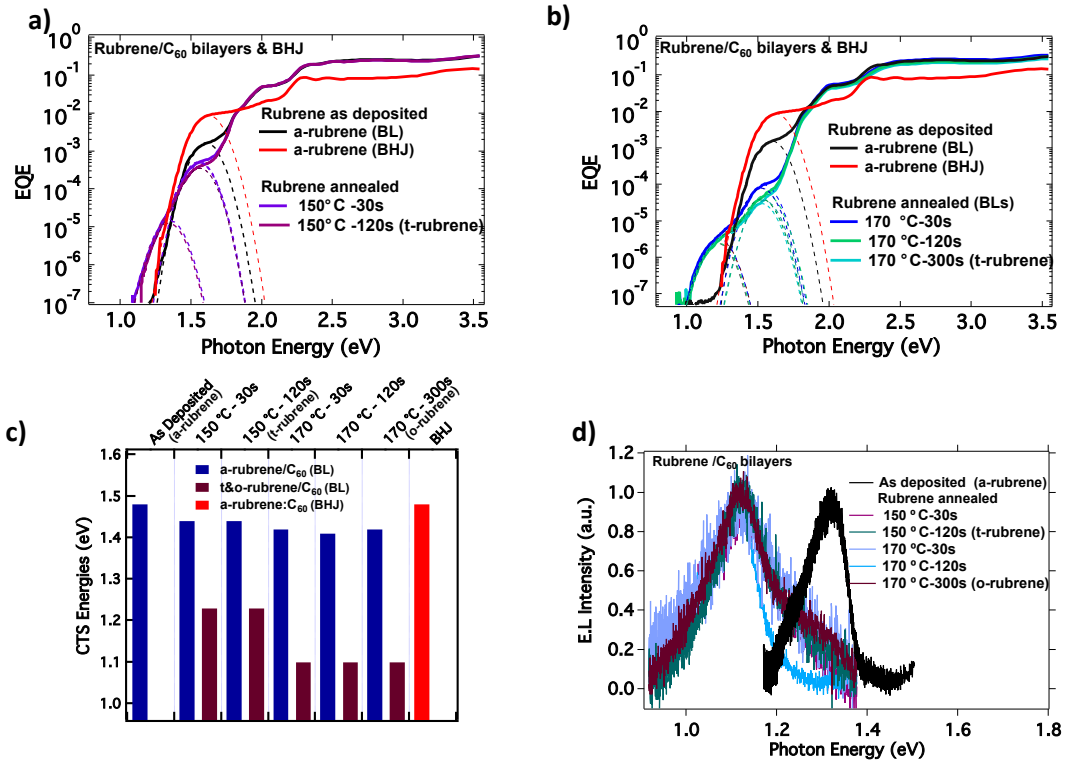

Figure 6.7: (a, b) Evolution of sub gap EQE spectra collected on bilayer and BHJ devices fabricated with as-deposited and annealed rubrene layers. In the case of as-deposited rubrene only a single CT band is visible. In the cases of annealed rubrene (t/o-rubrene), the CT band associated to amorphous rubrene at 1.48 eV decreases in strength with annealing temperature and time. (c) CT energies extracted from (a) and (b) for the high and low energy bands. (d) Electroluminescence spectra of all the corresponding rubrene/C_{60} bilayers.

6.4 First principle calculations to understand the origin of CT energy dependence on interfacial conformation of rubrene

To gain more insight into why E_{CT} should vary depending on the structure of rubrene, we have performed density functional theory calculations following the methods described in the experimental section. As mentioned above, to a good approximation, E_{CT} can be expressed as in Equation 6.1.

$$E_{CT} = IP_D - EA_A + E_{int} \tag{6.1}$$

Where IP_D is the ionization potential of the isolated donor phase, EA_A is the electron affinity of the isolated acceptor phase and E_int is the interaction energy that results when D and A are brought together to form an interface. IP_D has been found to be strongly dependent on the degree of structural order and molecular orientation.[130, 146, 173, 231–233] When C_{60} is used as the acceptor, the effect of acceptor orientation is minimal thanks to its spherical symmetry.

We have measured the IP of amorphous and crystalline rubrene layers by photoelectron spectroscopy (Figure 6.8). We find that the IP of crystalline rubrene (t-rubrene & o-rubrene), independently of the annealing condition, decreases by ∼0.4 eV compared with a-rubrene. This drastic decrease in ionization potential with increased crystalline order will most likely play a role into lowering the CT state energy at the crystalline rubrene/C_{60} interface. However, as suggested by Equation 6.1, interactions owing to polarization and the relative orientation of the D and A molecules at the rubrene/C_{60} interface also factor into E_{CT}. In Figure 6.9, we show the calculated dependence of CT state energy on rubrene/C_{60} conformation. Face-on conformation results in CT states with the lowest energy while end-on and edge-on conformations result in slightly higher CT state energies. These calculations suggest that in the case of rubrene/C_{60}, out of the three main interfacial molecular conformations, two conformations result in high CT state energies. Based on this observation, we expect that in the case of a-rubrene, whereby rubrene molecules are randomly oriented, it will be more probable to encounter high-energy CT state conformations than the low energy conformation. However, a-rubrene films may have a preferential surface termination.[46] To test whether this might impact interfacial energetics, we have measured the CT state energy of the BHJ device described above and found it to be identical to that of the BL using a-rubrene (Figure 6.6a). This shows that surface tex-

ture effects are negligible in BL devices and confirms that the model BL system can well mimic the interfacial properties of the BHJ, as previously indicated by comparing the Voc of BL and BHJ devices.

While the absolute values of the calculated E_{CT} are expected to be somewhat different from the experimentally determined values, their relative shifts should carry meaning. The fact that for all the three conformations assessed in the calculations carried out on complexes made of a single rubrene and a single C_{60} molecule, the maximal CT energy shifts by only ∼100 meV, compared with an experimental shift of 380 meV, points to other factors contributing to lowering the CT energy at the crystalline rubrene/C_{60} interface. As discussed above, the annealed rubrene films are textured differently and exhibit different crystalline structures (Figure 6.2, 6.3). The resulting surface terminations (Figure 6.2e, 6.2f) lead to two very different molecular conformations of the donor, yet the corresponding E_{CT} (1.23 eV vs. 1.1 eV) differs by only ∼130 meV, in agreement with the simplified theoretical calculations. Comparing with the case of a-rubrene for which the disordered film surface exhibits a preferential molecular conformation gives rise to the highest E_{CT} (1.48 eV), points to the potential importance of packing order within the donor film. Thus, the question arises whether the extent of aggregation and crystalline order of the donor can be playing a much more important role than conformational differences at the D-A interface.

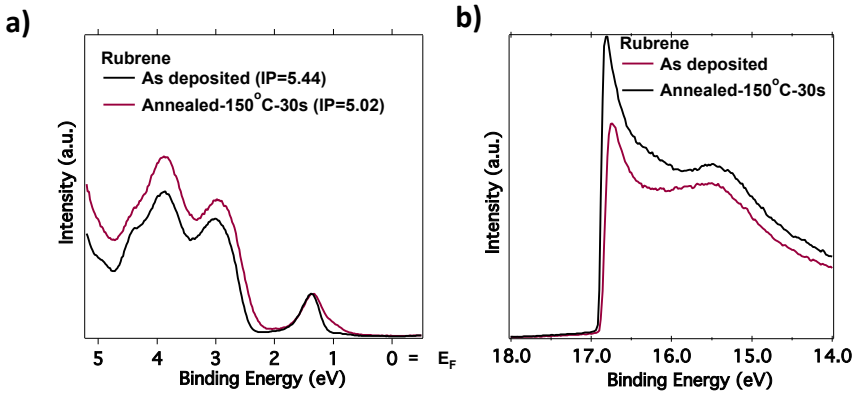

Figure 6.8: UPS spectra showing the valence region of 50 nm amorphous and crystalline rubrene films on gold foil (a) and the secondary-electron cutoff (b) both used to determine the ionization potential of the sample. The x-axis shows the binding energy relative to the gold substrate Fermi level (E_F). The work function was found to be 4.32 eV. For amorphous rubrene, the valence band maximum appears at 1.12 eV below the Fermi level corresponding to an ionization potential of 5.44.0 eV. Upon annealing at 150 °C for 30s, the ionization potential is decreased to 5.02 eV.

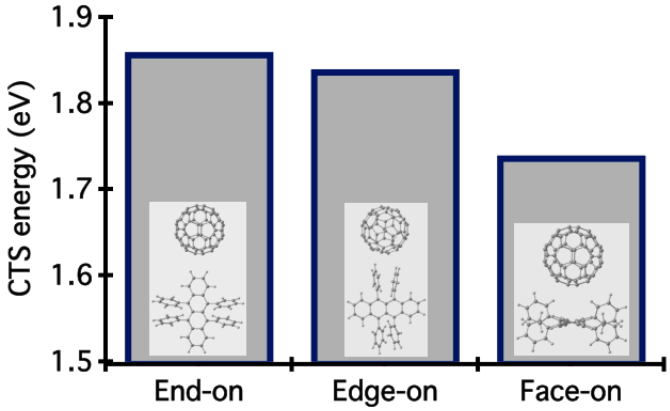

Figure 6.9: Whether the D and A molecules touch end-on, edge-on or face-on would influence the energy of the CT state. In a bilayer configuration with amorphous rubrene, the rubrene molecules are expected to be isotropically distributed and to present a homogeneous interface that would form in the presence of C_{60} a distribution of CT states that is centered around a certain mean value. Edge-on, side-on and face-on conformations correspond to CT energies of 1.86 eV, 1,84 eV and 1.74 eV respectively meaning a decrease of 0.1 eV between face-on, edge-on, and side-on conformations.

It is well known that crystalline rubrene can exhibit band-like transport, which is

a manifestation of the high degree of electronic delocalization. Likewise, previous theoretical work [47] on tetracene/C_{60} bilayers show that face-on conformation and tetracene packing, through delocalization effects, lower the E_{CT}. Furthermore, the low ionization potential of the annealed rubrene films is indicative that the hole is more stabilized in the crystalline phase, i.e. effectively more delocalized. In situ UPS measurements performed at different stages of C_{60} deposition on amorphous and crystalline phases of rubrene indicate there is little or no intermixing, therefore resulting in a nominally abrupt D/A interface in BL systems (Figure 6.10).[166] Thus, it can be it can be reasonably concluded that crystalline rubrene/ C_{60} interfaces will form predominantly low energy CT states and that hole delocalization [234] within the aggregated rubrene phase will in fact account for most of the measured 0.38 eV difference in E_{CT} between a-rubrene/C_{60} and t-,o-rubrene/C_{60} interfaces.

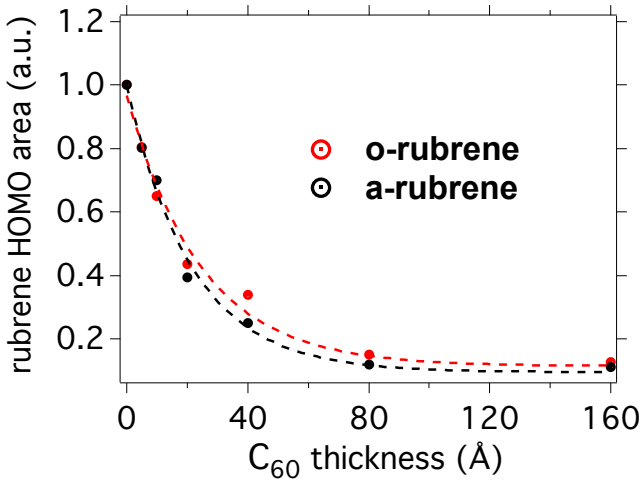

Figure 6.10: Attenuation of the HOMO peaks from a-rubrene and o-rubrene with increasing thickness of C_{60}. The dashed lines are fits showing the exponential decay of the HOMO signal. The exponential trend indicates there is no appreciable mixing of rubrene with C_{60}.

6.5 Exciton dissociation at interfaces containing both amorphous and crystalline rubrene phases

Although the spectral position of the subgap features in our EQE data (Figure 6.6a and Figure 6.6b) are in qualitative agreement with theoretical calculations, it is rather unexpected that the strength of the CT band associated to the interfaces with t-rubrene and o-rubrene is about two orders of magnitude lower than that of the CT band associated with a-rubrene in the annealed devices. Two factors control the strength of the CT band. The CT state oscillator strength, related to the square of the transition dipole moment of the CT complex, and the density of interfacial CT states. It is possible to experimentally measure the product of these two factors by performing photothermal deflection spectroscopy (PDS) measurements. We have carried out such experiments on both bilayers made with a- and o-rubrene (Figure 6.11) and we found that CT state extinction coefficients for the BL system with a-rubrene is about one order of magnitude lower than for the BL system with the crystalline rubrene films. This suggests that the effective interfacial area may be changing upon annealing the rubrene film, possibly due to roughening, as rubrene becomes polycrystalline. We have confirmed this to be the case via an atomic force microscopy (AFM) analysis of the surface topography of rubrene films before and after annealing (Figure 6.12). While the PDS data would suggest that subgap absorption remains fairly constant in the BL system with o-rubrene, and thus, a comparable product of oscillator strength and number of interfacial CT states in the entire spectral range probed below the bandgap, we note that the expected difference in the sub-bandgap noise level in PDS for amorphous and crystalline rubrene limits our ability to definitively decouple the role of the CT oscillator strength and the number of interfacial CT states.

However it is plausible that CT state photocurrent generation may influence the relative CT bands strengths. Still, exciton dynamics in rubrene/C_{60} is very complex. Several groups have elucidated the triplet character of CT states as well as CT triplet

back transfer to the rubrene triplet T1 state at the rubrene/C_{60} interface.[80, 235, 236] Although in a-rubrene this process does not represent a terminal loss,[80] a recent study suggests that in crystalline rubrene CT triplet back transfer to the rubrene T1 would be inefficient.[237]

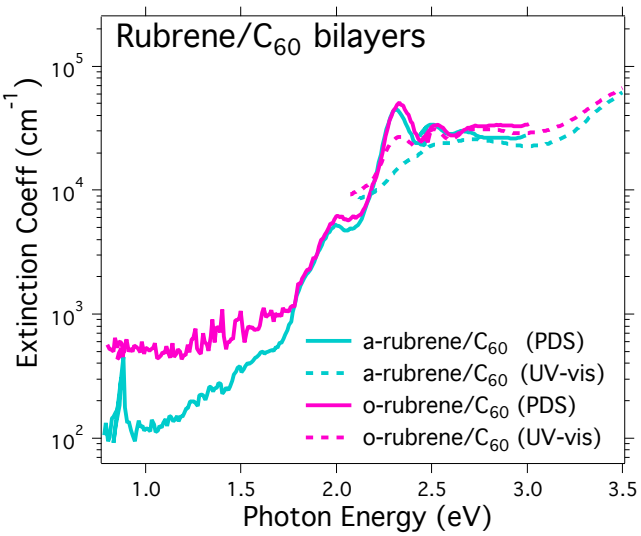

Figure 6.11: CT state extinction coefficient measured by photothermal defection spectroscopy (PDS) on layers of amorphous rubrene/C_{60} and crystalline rubrene/C_{60}. The spectra are matched to UV-Vis absorption spectra of the same bilayers. However, we note the discrepancy between the UV-Vis spectra and the portion of the PDS spectra above the band edge, which we attribute to scattering near the band-edge that would artificially increase absorption in UV-Vis. We also note that the expected difference in the sub-bandgap noise level in PDS for amorphous and crystalline rubrene limits our ability to compare subgap absorption accurately.

Photoluminescence studies have shown that triplet fusion is more efficient in the a-rubrene than in crystalline rubrene and the possibility of triplet transfer from the crystalline phase to the amorphous phase.[133] If such processes lead to increased non-radiative recombination at the interfaces with crystalline rubrene, it becomes difficult to assign Voc loss solely to the presence of low energy CT states. We compare the difference E_{CT} - qVoc for bilayers in which rubrene is the most disordered (a-rubrene/C_{60}) and exhibits the most order (o-rubrene/C_{60}; annealed for 300 s). In the latter case, we make the provisional assumption that the lowest CT energy de-

termines the Voc. As we found that E_{CT} - qVoc only differs by 70 meV (540 meV vs. 470 meV) for the amorphous and annealed cases, respectively, we do not expect differences in the amount of non-radiative recombination to influence Voc significantly. Similarly, Jsc and FF are comparable for all devices. Thus, it is very likely that there are intricate photophysical processes involving rubrene triplet states that enable the apparent current losses at the crystalline rubrene/C_{60} interface to be recycled.

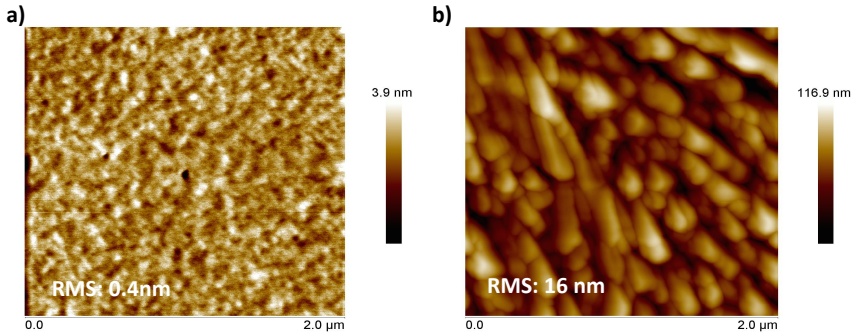

Figure 6.12: Atomic force microscopy topographic images of 50 nm rubrene thin films on ITO. (a) Amorphous rubrene layer, (b) Rubrene layer annealed at 150 °C for 30s.

6.6 Estimating the Voc in the presence of multiple interfacial CT bands

To evaluate the relative influence of the two CT bands on Voc, we have used a recently developed model [20] that expresses Voc exclusively in terms of CT states characteristics. According to this model, Voc is equated to the chemical potential of CT states. As such, it is expressed in term of the energy of the CT state, its population and its lifetime. One of the attractive features of the model is that it is easily generalizable to systems exhibiting more than one CT band. Considering contributions from CT states at the interfaces with both amorphous and crystalline rubrene, the photocurrent density generated by the device can be expressed as in Equation (3).[20]

$$J_{sc} = J_{rec} = qN_{ct}/\tau_{ct} = q/\tau_{ct}(\underbrace{N_{oa}e^{\frac{qVoc-E_{cta}}{kT}}}_{amorphous} + \underbrace{N_{oc}e^{\frac{qVoc-E_{ctc}}{kT}}}_{crystalline}) \tag{6.2}$$

Here, N_{oa} and N_{oc} are the total numbers of interfacial CT states formed at the interface between C_{60} and the amorphous and crystalline phases of rubrene, respectively; μ_{ct} is the CT state lifetime and E_{cta} and E_{ctc} are the CT state energies associated to the amorphous and crystalline (triclinic or orthorhombic) phases and J_{rec} is the recombination current at Voc. We make the simplifying assumption that the CT lifetime, τ_{ct}, is identical for the CT states at all three interface types. Solving Equation 6.2 for Voc we arrive at Equation 6.3, which allows us to calculate the Voc based on the data extracted from EQE measurements and using a value for τ_{ct} comparable to literature values.[20]

$$V_{oc} = \frac{-kT}{q}ln(\frac{q}{\tau_{ct} * Jsc}) - \frac{-kT}{q}ln(\underbrace{N_{oa}e^{\frac{qVoc-E_{cta}}{kT}}}_{amorphous} + \underbrace{N_{oc}e^{\frac{qVoc-E_{ctc}}{kT}}}_{crystalline}) \tag{6.3}$$

In Figure 6.13, we compare the predicted and experimental Voc values for all bilayer devices assuming a single lifetime of τ_{ct} =5 ns.

Following work in reference [20] in main text, Voc can be expressed following Equation 6.4.

$$qV_{oc} = E_{CT}^{exp} - ln(\frac{qfN_0L}{\tau_{ct}J_sc}) \tag{6.4}$$

Where E_{CT}^{exp} is the temperature-dependent experimental charge transfer state energy, τ_{ct} is the CT state lifetime, f is the fraction of the film forming the interface, N_0 is the molecular density, and L is the thickness of the active layer. Equation 6.4 suggests that the loss term can be understood in terms of the CT state lifetime τ_{ct} and the fraction of the interface that is mixed fN_0L. We make the assumption that τ_{ct} is invariant with rubrene extent of order. The reason we make this assumption

is that experimental values of CT state lifetimes remain across a relatively narrow range considering the diversity of molecular systems in the solid state for which they correspond. A plausible value for τ_{ct} is obtained by solving Equation 6.4 for τ_{ct} in the case of the bilayer with amorphous rubrene. Assuming a molecular density of 1.0×10^{21} cm^{-3} and 1nm of mixed layer ($f * L = 1$) (limiting case of no intermixing), results in a CT state lifetime of 5ns, a value, which we adopt for our predictions. Although Equation 6.4 is appropriate to describe V in the amorphous case, the EQE data in Figure 6.6 in the main text suggest that we need to account for both the interface with amorphous and crystalline rubrene as they both generate photocurrent.

We first express the total number of CT states which is obtained by adding contribution from CT states at the amorphous rubrene/C_{60} and crystalline rubrene/C_{60} interfaces according to the approach in reference [20].

Assuming $f * L = 1$, we express N_{ct} as in Equation 6.5.

$$N_{ct} = (\underbrace{N_{oa}e^{\frac{qVoc-E_{cta}}{kT}}}_{amorphous} + \underbrace{N_{oc}e^{\frac{qVoc-E_{ctc}}{kT}}}_{crystalline}) \tag{6.5}$$

Where N_{oa} and N_{oc} are respectively the number of interfacial CT states, form with fullerene at the interface where rubrene is amorphous and crystalline. By constraining the sum of these two numbers is to the assumed film molecular density, their values are estimated from intensities ratios of the CT bands in the EQE spectra.

While the quantitative agreement appears to be good, we caution that this is subject to change if a different value of τ_{ct} were selected (Additional comparisons based on $0.5 < \tau_{ct} < 10\ ns$ in Figure 6.14). However, importantly, we find the predicted Voc perfectly tracks the trend in the experimental Voc, which further emphasizes that Voc very much reflects the composition of the CT manifold and underlines the significant role of low-lying CT states in pinning the Voc. Such low-lying CT states are due to the presence of ordered donor and/or acceptor domains at the D/A interface.

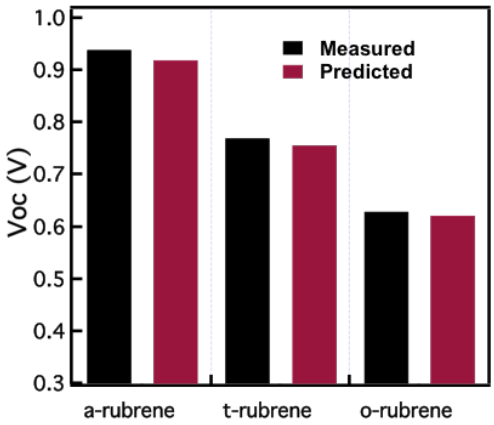

Figure 6.13: Experimental and predicted values of Voc for rubrene/C_{60} bilayer solar cells using Equation (6.3 along with quantitative analysis of the CT state manifold. In the case of BHJ solar cells where interfacial structural order is conceivably much harder to realize, and for which interfacial area is significantly larger, we expect a much larger number of interfacial molecular configurations to become accessible and the interfacial energetic landscape to be characterized by a much broader distribution of CT states.[238] The findings of this work suggest that the relative number of the lowest lying CT states is orders of magnitude smaller but that their low energy has a dramatic effect on Voc.

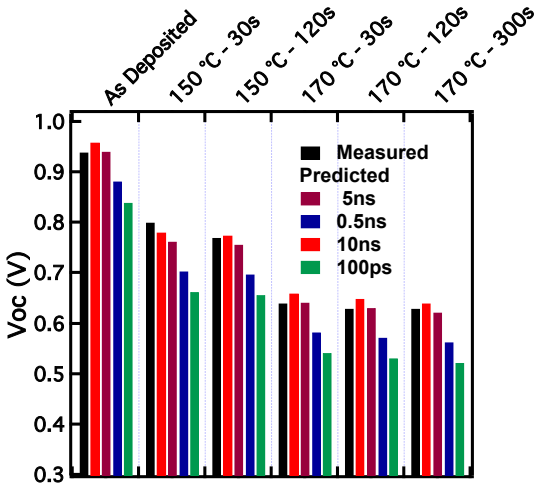

Figure 6.14: Modeled and experimental values of Voc for rubrene/C_{60} bilayer solar cells annealed at various temperatures and CT states lifetime.

6.7 Conclusions

In this work, we have shown that the coexistence of ordered and disordered phases and polymorphs exhibiting different CT energetics constitute important limiting factors for the Voc in organic solar cells. In the rubrene- C_{60} system, the rubrene phase that is ordered enables the formation of charge transfer states that are as much as 380 meV lower in energy than CT states formed by the disordered phase. The presence of such energetically low-lying CT states primarily controls the amount of voltage that the cell can produce. For the rubrene- C_{60} system, the presence of such states with low E_{CT} translates into Voc loss amounting to up to 310 meV in rubrene- C_{60} devices made with partially ordered rubrene. Our results underline once again the compromise that has to be reached in terms of formation of delocalized states, which favor charge separation but lower E_{CT} and increase nonradiative recombination to the ground state.[47, 234] Considering BHJ devices for which the interfacial area is substantially greater and where the development of structural order of the donor and acceptor phases can be easily inhibited, the coexistence of different phases poses an important challenge to maximizing the Voc. Yet, semi-crystallinity and polymorphism are staples of conjugated materials commonly used in organic photovoltaics. Semicrystallinity of certain conjugated polymers, such as P3HT, stems from the permanent coexistence of ordered and disordered phases.[104, 239] In order to prevent Voc loss it is therefore crucial to realize interfacial structural control that results in high CT states and eliminates the presence of low-lying CT states. This requires that the design of new conjugated donors and acceptors incorporates the need for realizing interfaces with locally disordered donor and acceptor so as to maximize the CT state energy, while nearby donor and acceptor domains are kept pure and exhibit the required degree of aggregation and crystallinity to assure sufficiently rapid charge transport and minimize the opportunity for charge recombination. In this respect, the existence of a thin interfacial mixed phase throughout the BHJ would be crucial. Such systems

would be based on donors that can spontaneously mix with acceptors.[220, 231]

Chapter 7

Concluding Remarks

7.1 Summary

In this thesis, we have investigated the impact of molecular conformation and materials structure on interfacial energetics, charge transfer and performance of organic solar cells. To achieve that we used representative model systems to recreate a series of microstructures that emulate those found in typical BHJ solar cells. We have shown, using these model systems, the connection between microstructure and materials energy states. We have equally linked materials energy states to the photovoltaic performance in organic photovoltaics (OPVs). In this final chapter, we retrace the main conclusions and implications of the work and suggest opportunities for future research. We do so by presenting our views on how our findings relate to lingering challenges in OPVs and how they motivate new research directions.

Essentially, the strength of intermolecular interactions determines how materials organize in pure phases and mixtures. Likewise, the extent to which the donor (D) and the acceptor (A) mix depends on how strongly they interact. In organic solar cells based on crystalline small molecules, the impact of such interactions on the local order is intricate and not always readily predictable. Although theoretical calculations make powerful tools for predicting intermixing at the D-A interface, the lack of a universal trend suggests that in-depth structural characterizations are critical in confirming the precise morphology at the interface. Bilayers as model systems, although simple, have proven incredibly useful platforms in probing interfacial order.

In Chapter 4, looking at the impact of donor molecular packing on the spontaneous interfacial mixing and using ZnPc/C_{60} bilayers as model systems, we found that at the D-A interface, donor molecular packing modulate the extent of intermolecular interactions with C_{60} and in turn controls the degree of local structural order. We have shown how controlled deposition of thin films, x-ray scattering and photoelectron spectroscopies used in combination allowed us to successfully probe local order in organic thin film stacks. π-conjugated materials constitute fundamentally anisotropic systems. Their molecular backbone is rich in delocalized π-electrons, which tends to interact more strongly with neighboring molecules than the other parts of the molecule. We found that this anisotropy leads to an intriguing morphological paradigm having implications not only in terms of the orientation dependence of electronic properties of the conjugated molecules but also in terms of how materials interact especially at interfaces. More precisely, we have shown that C_{60} interacts more strongly with the portion of the ZnPc molecule that is rich in electrons increasing its tendency to strongly intermix with fullerene when it orients, with respect to fullerene, in the face-on conformation. This tendency to mix is less pronounced when the ZnPc molecule adopts an edge-on conformation in which the π-electron cloud is less accessible to C_{60}. This morphological paradigm challenges the view of an invariably discrete interface between aggregated donor and C_{60}. It strongly suggests that in the case of a BHJ, in which the ability to precisely control the texture at the interface is limited, the interfacial microstructure will be incredibly complex because many molecular conformations are expected to be present, making it likely that mixed and discrete interfaces will form simultaneously. As we showed in Chapter 5, for some donor systems such as bDIP, the tendency to mix with fullerene is significantly pronounced to the point that it mixes spontaneously with C_{60} even at cold temperatures.

Our work thus suggests that it will be important to probe the interfacial microstructure in BHJ systems systematically, starting with simple model systems as a means

to dissect the more structurally complex heterojunction. Intermixing significantly alters interfacial energetics and requires that device modeling be revised correspondingly. As we found, in ZnPc/C_{60}, spontaneous mixing is responsible for the increase in photocurrent.

In Chapter 5 we discussed the roles of structural order, intermolecular interactions and conformation in D-A blends and the implications for exciton dissociation. We have found that the molecular environment, to a large extent, shapes the interfacial energy landscape. The bare knowledge of the energy levels of materials in their pure state is insufficient to predict the energy landscape right at the donor interface. Such predictions require careful measurements of materials energy levels in the state they assume in actual devices. The D-A contacts will exist in the mixed phase, and at the boundaries between pure D and A phases. For a given molecule (D or A) each of these environments is energetically distinct. In addition, D and A may adopt different conformations for each of these environments to further minimize energy. Through investigation of the energy landscape in both amorphous and crystalline donors differing in polarity and polarization energies, we have found that the determining factor that primarily controls the energy landscape is the materials polarization energy. When the polarization energy is large, we will expect significant shifts in the energy of the frontier orbitals in these various environments. We have shown using ultraviolet photoelectron spectroscopy (UPS) measurements that in going from the pure phase to the mixed phase in small molecules BHJs, the ionization potential of the materials (both D and A) could shift by more than 0.4 eV. For instance, in the sexithiophene:C_{60} system, the polarization energy difference between sexithiophene (6T) and C_{60} is $\sim$0.8 eV which primarily explains the large shift of $\sim$0.6 eV between the IE of 6T in films with $\geq$75% (by vol.) 6T composition and that of 6T in films with $\leq$25% 6T. As we found, this dramatic shift also originates, but to a lesser degree, from differences in molecular conformation in pure and mixed

phases. Overall, these findings have huge implications in terms of charge separation and bimolecular recombination in OPVs. Such large shifts in material's energy levels means that the interfacial Coulomb barrier, due to the charge transfer (CT) state binding energy (∼0.4 eV), could be overcome by the driving force originating from the shift in energy levels that follows from variations in materials conformation and phase composition in BHJs. Thus, such structurally driven shifts in materials energy states could be exploited to achieve vanishingly small interfacial Coulomb binding energies. An area of active research in the OPV field is raising the dielectric constant as a means to reduce the CT Coulomb binding energy and by the same token raising both E_{CT} and Voc. Our findings suggest that future research may exploit both approaches, i.e. large differences in donor and acceptor polarizations and materials high dielectric constant, to effectively minimize CT state binding energies. Materials polarization would have to be considered as a good indicator of the magnitude of energy levels shifts in the process of predictive device modelling.

At the device level, the energy landscape is crucial since it governs the thermodynamic of photovoltaic processes, which in turn determine the device performance. Owing to its three-dimensional nature, the BHJ leads to a highly structurally complex manifold. This means that materials phases with a wide distribution of energy states are likely to coexist. But thermodynamics will favor the occupation, by bound charge pairs or free carriers, of the low-energy states over that of the high-energy states. This implies that the chemical potential of the CT excitons and free carriers will be determined by the energy of these low-lying states.

In Chapter 6 we showed how semi-crystallinity leads to the coexistence of multiple interfacial charge transfer (CT) bands using rubrene/C_{60} system. We found that low-energy states arose mainly from delocalization in the crystalline phase of rubrene and that these states pin Voc very effectively. This finding implies that even if materials chemistry could be altered such that very high-energy states are predominantly

formed, the low energy states that are present even in minority will compromise PV performance. It is thus important, to ensure that in BHJs, only high-energy states are formed exclusively. Our findings also suggest that an effective approach to achieving low Voc loss would be to design donor materials that are highly miscible with fullerene, in agreement with the current three-phase model widely popular in the OPV field. As such, the mixed phase, which is often a high-energy phase, will form at all D-A interfaces across the blend yielding narrow CT band with a high CT energy and thus devices with high Voc.

Beyond high Voc, the mixed phase is also essential in enabling efficient charge separation in OPVs as was shown mainly in Chapter 5. A consistent three-phase morphology, i.e. the mixed phase sandwiched between pure D and A phases, would create an energy level offset, that would help prevent bimolecular recombination, because carriers will separate in the mixed phase but be prevented from meeting once they are parted and in the pure phases. To put it another way, most of the interface would form in the mixed phase, but more often the CT states in the mixed phase will not be occupied, for thermodynamic reasons, therefore minimizing the chances for free charges to encounter after they have separated.

7.2 Future Research Work

While our research points to how one of the main challenges in the OPV field, that of understanding the influence of molecular structure and materials energy states on the photovoltaic performance, may be tackled, there remain however several areas of improvement. The studies in this work relied on vacuum processed bilayers and small molecules BHJs systems. Although our conclusions could easily be translated to some BHJs based on polymeric materials processed from solution, the scope of our studies is limited in that, beyond molecular interactions, kinetic factors involved in the film formation process by solution processing to a great extent control the microstructure.

The mechanism by which pure and mixed phases form in solution processed OPVs and vacuum processing can differ markedly. Other factors that significantly influence the final microstructure of the BHJ such as materials solubility and the rate of solvent evaporation would introduce variations in the final microstructure. Our research also does not address what appear to be important exceptions. Recently reported trends in the interfacial energetics in some modern polymer systems, such as PIPCP whose backbone comprises CPDT-PT-IDT-PT repeat units (CPDT = cyclopentadithiophene, PT = pyridyl[2,1,3]thiadiazole, IDT = indacenodithiophene) exhibit a rather intriguing energetics whereby energy level shifts in the blend tend to suggest more stabilized frontiers orbitals of the donor in the blend compared to the pure film. Interestingly solar cells based on PIPCP:PCBM blends have a high CT state energy and exhibit one of the lowest voltage loss.[240] Therefore, future research should revisit current understanding of energetics in OPV materials, especially when investigating state-of-the-art high performing polymers and oligomers systems. Numbers of these material systems, although high performing still suffer important voltage losses. Since most of these materials are processed from solution, there will be need for developing sensitive in-situ probes adapted for solution-processed devices. These probes should be able to detect energy states that are very low density. Yet polymers may remain hard to study because of their complex structure. Theoretical work will be needed to provide sound conceptual framework to support experimental research.

REFERENCES

[1] S. E. Braslavsky, Pure Appl. Chem. **79**, 293 (2007).

[2] U. S. E. I. Administration, Annual Energy Outlook **AEO2015**, 154 (2015).

[3] Heliatek, Press Release , March 24 (2014).

[4] R. R. Søndergaard, M. Hösel, and F. C. Krebs, J. Polym. Sci. Part B Polym. Phys. **51**, 16 (2013).

[5] R. Søndergaard, M. Hösel, D. Angmo, T. T. Larsen-Olsen, and F. C. Krebs, Mater. Today **15**, 36 (2012).

[6] A. Gambhir, P. Sandwell, and J. Nelson, Sol. Energy Mater. Sol. Cells **156**, 49 (2016).

[7] B. Azzopardi, C. J. M. Emmott, A. Urbina, F. C. Krebs, J. Mutale, and J. Nelson, Energy Environ. Sci. **4**, 3741 (2011).

[8] F. C. Krebs, Sol. Energy Mater. Sol. Cells **93**, 394 (2009).

[9] A. Polman, M. Knight, E. C. Garnett, B. Ehrler, and W. C. Sinke, Science (80-.). **352**, 307 (2016).

[10] J. Zhao, Y. Li, G. Yang, K. Jiang, H. Lin, H. Ade, W. Ma, and H. Yan, Nat. Energy **1**, 15027 (2016).

[11] Y. Liu, J. Zhao, Z. Li, C. Mu, W. Ma, H. Hu, K. Jiang, H. Lin, H. Ade, and H. Yan, Nat. Commun. **5**, 5293 (2014).

[12] H. Zhou, Y. Zhang, C. K. Mai, S. D. Collins, G. C. Bazan, T. Q. Nguyen, and A. J. Heeger, Adv. Mater. **27**, 1767 (2015).

[13] F. C. S. P. Thanks and M. Pfeiffer, press release , 2 (2016).

[14] M. A. Green, K. Emery, Y. Hishikawa, W. Warta, and E. D. Dunlop, Wiley Online Libr. , 827 (2013).

[15] NREL, "National Renewable Energy Laboratory, Best Research-Cell Efficiencies," (2016).

[16] D. Neher, J. Kniepert, A. Elimelech, L. J. A. Koster, Y. Liu, J. Zhao, S. Albrecht, C. M. Proctor, M. Kuik, T.-Q. Nguyen, G. Lakhwani, A. Rao, R. H. Friend, S. M. Arnab, M. Z. Kabir, Y. T. Set, T. Zhang, E. Birgersson, J. Luther, M. L. I. Ibrahim, Z. Ahmad, K. Sulaiman, D. Bartesaghi, U. Würfel, D. Neher, A. Spies, S. Albrecht, T. Kirchartz, J. Bisquert, I. Mora-Sero, G. Garcia-Belmonte, W. Li, T. Müller, U. Rau, T. Kirchartz, S. Schiefer, B. Zimmermann, U. Würfel, I. Lange, M. Oehzelt, N. Koch, G. Heimel, U. Würfel, A. Cuevas, P. Würfel, A. M. Goodman, A. Rose, M. Riede, R. Meerheim, C. Körner, K. Leo, T. L. Nguyen, W. Li, T. Kirchartz, T. Agostinelli, M. Campoy-Quiles, W. Gong, J. Nelson, G. F. A. Dibb, V. D. Mihailetchi, J. Wildeman, P. W. M. Blom, N. Rappaport, O. Solomesch, N. Tessler, M. A. Green, M. Stolterfoht, F. Deledalle, P. S. Tuladhar, J. Nelson, J. R. Durrant, T. Kirchartz, J. Kniepert, S. Foster, S. Albrecht, S. Albrecht, J. Kniepert, I. Lange, N. J. van der Kaap, L. J. A. Koster, D. Neher, J. A. Bartelt, D. Lam, T. M. Burke, S. M. Sweetnam, M. D. McGehee, A. J. Moulé, J. B. Bonekamp, and K. Meerholz, Sci. Rep. **6**, 24861 (2016).

[17] T. M. Clarke and J. R. Durrant, Chem. Rev. **110**, 6736 (2010).

[18] J.-L. Bredas, J. E. Norton, J. Cornil, and V. Coropceanu, Acc. Chem. Res. **42**, 1691 (2009).

[19] T. M. Burke and M. D. McGehee, Adv. Mater. **26**, 1923 (2014).

[20] T. M. Burke, S. Sweetnam, K. Vandewal, and M. D. McGehee, Adv. Energy Mater. **5**, 1500123 (2015).

[21] S. A. Mollinger, K. Vandewal, and A. Salleo, Adv. Energy Mater. **5**, 1 (2015).

[22] K. Vandewal, S. Albrecht, E. T. Hoke, K. R. Graham, J. Widmer, J. D. Douglas, M. Schubert, W. R. Mateker, J. T. Bloking, G. F. Burkhard, A. Sellinger, J. M. J. Fréchet, A. Amassian, M. K. Riede, M. D. Mcgehee, D. Neher, and A. Salleo, Nat. Mater. **13**, 63 (2013).

[23] H. Hu, K. Jiang, J.-H. Kim, G. Yang, Z. Li, T. Ma, G. Lu, Y. Qu, H. Ade, and H. Yan, J. Mater. Chem. A , 5039 (2016).

[24] H.-L. Yip and A. K. Jen, Energy Environ. Sci. **5**, 5994 (2012).

[25] S. P. Singh, G. C. Bazan, L. F. Lai, V. Gupta, R. Datt, S. Chand, and A. J. Heeger, Chem. Commun. , 8596 (2016).

[26] H. C. Liao, C. C. Ho, C. Y. Chang, M. H. Jao, S. B. Darling, and W. F. Su, Mater. Today **16**, 326 (2013).

[27] T. Ameri, N. Li, and C. J. Brabec, Energy Environ. Sci. **6**, 2390 (2013).

[28] S. E. Shaheen, C. J. Brabec, N. S. Sariciftci, F. Padinger, T. Fromherz, and J. C. Hummelen, Appl. Phys. Lett. **78**, 841 (2001).

[29] N. S. Sariciftci, L. Smilowitz, a. J. Heeger, and F. Wudl, Science **258**, 1474 (1992).

[30] M. Knupfer, Appl. Phys. A Mater. Sci. Process. **77**, 623 (2003).

[31] M. A. Green, AIP Adv. **3**, 0 (2013).

[32] S. Torabi, F. Jahani, I. Van Severen, C. Kanimozhi, S. Patil, R. W. A. Havenith, R. C. Chiechi, L. Lutsen, D. J. M. Vanderzande, T. J. Cleij, J. C. Hummelen, and L. J. A. Koster, Adv. Funct. Mater. **25**, 150 (2015).

[33] W. C. Dunlap and R. L. Watters, Phys. Rev. **92**, 1396 (1953).

[34] J. Bredas and G. Street, Acc. Chem. Res. **1305**, 309 (1985).

[35] B. C. Thompson and J. M. J. Fréchet, Angew. Chem. Int. Ed. Engl. **47**, 58 (2008).

[36] C. W. Tang, Appl. Phys. Lett. **48**, 183 (1986).

[37] N. S. Sariciftci, L. Smilowitz, A. J. Heeger, and F. Wudl, Science (80-.). **258**, 1474 (1992), arXiv:arXiv:1011.1669v3 .

[38] O. V. Mikhnenko, P. W. M. Blom, and T.-Q. Nguyen, Energy Environ. Sci. Energy Environ. Sci **8**, 1867 (2015).

[39] G. Yu, J. Gao, J. C. Hummelen, F. Wudl, and a. J. Heeger, Science (80-.). **270**, 1789 (1995).

[40] J. J. M. Halls, C. A. Walsh, N. C. Greenham, E. A. Marseglia, R. H. Friend, S. C. Moratti, and A. B. Holmes, Nature **376**, 498 (1995).

[41] G. Lakhwani, A. Rao, and R. H. Friend, Annual Review of Physical Chemistry **65**, 557 (2014).

[42] D. Credgington and J. R. Durrant, J. Phys. Chem. Lett. **3**, 1465 (2012).

[43] L. Goris, A. Poruba, L. Hod'kova, M. Van??ek, K. Haenen, M. Nesldek, P. Wagner, D. Vanderzande, L. De Schepper, and J. V. Manca, Appl. Phys. Lett. **88**, 052113 (2006).

[44] L. Goris, K. Haenen, M. Nes, A. Dek, P. Wagner, D. Vanderzande, L. De Schepper, J. D 'haen, L. Lutsen, and J. V. Manca, J Mater Sci **40**, 1413 (2005).

[45] K. Vandewal, K. Tvingstedt, A. Gadisa, O. Inganäs, and J. V. Manca, Phys. Rev. B **81**, 125204 (2010).

[46] K. R. Graham, P. Erwin, D. Nordlund, K. Vandewal, R. Li, G. O. Ngongang Ndjawa, E. T. Hoke, A. Salleo, M. E. Thompson, M. D. McGehee, and A. Amassian, Adv. Mater. **25**, 6076 (2013).

[47] B. Yang, Y. Yi, C.-R. Zhang, S. G. Aziz, V. Coropceanu, and J.-L. Brédas, J. Phys. Chem. C **118**, 27648 (2014).

[48] S. M. Ryno, C. Risko, and J.-L. Brédas, ACS Appl. Mater. Interfaces **8**, 14053 (2016).

[49] S. M. Ryno, M. K. Ravva, X. Chen, H. Li, and J.-L. Brédas, Adv. Energy Mater. , 1601370 (2016).

[50] Y. T. Fu, C. Risko, and J. L. Brédas, Adv. Mater. **25**, 878 (2013).

[51] a. C. Mayer, M. F. Toney, S. R. Scully, J. Rivnay, C. J. Brabec, M. Scharber, M. Koppe, M. Heeney, I. McCulloch, and M. D. McGehee, Adv. Funct. Mater. **19**, 1173 (2009).

[52] N. D. Treat, A. Varotto, C. J. Takacs, N. Batara, M. Al-Hashimi, M. J. Heeney, A. J. Heeger, F. Wudl, C. J. Hawker, and M. L. Chabinyc, J. Am. Chem. Soc. **134**, 15869 (2012).

[53] W. Ma, C. Yang, X. Gong, K. Lee, and A. J. Heeger, Adv. Funct. Mater. **15**, 1617 (2005).

[54] H. Hoppe and N. S. Sariciftci, J. Mat. Chem. **16**, 45 (2005).

[55] S. R. Scully and M. D. McGehee, J. Appl. Phys. **100**, 034907 (2006).

[56] A. J. Heeger, Adv. Mater. **26**, 10 (2014).

[57] Z. Xu, L.-M. Chen, G. Yang, C.-H. Huang, J. Hou, Y. Wu, G. Li, C.-S. Hsu, and Y. Yang, Advanced Functional Materials **19**, 1227 (2009).

[58] L. Dou, Y. Liu, Z. Hong, G. Li, and Y. Yang, Chem. Rev. **115**, 12633 (2015).

[59] P.-L. T. Boudreault, A. Najari, and M. Leclerc, Chem. Mater **23**, 456 (2011).

[60] V. I. Klimov, Annu. Rev. Phys. Chem. **58**, 635 (2007).

[61] G. F. Burkhard, E. T. Hoke, and M. D. McGehee, Adv. Mater. **22**, 3293 (2010).

[62] C. J. Bardeen, Annu. Rev. Phys. Chem. **65**, 127 (2014).

[63] E. T. Hoke, K. Vandewal, J. a. Bartelt, W. R. Mateker, J. D. Douglas, R. Noriega, K. R. Graham, J. M. J. Fréchet, A. Salleo, and M. D. McGehee, Adv. Energy Mater. **3**, 220 (2013).

[64] N. A. Ran, J. A. Love, C. J. Takacs, A. Sadhanala, J. K. Beavers, S. D. Collins, Y. Huang, M. Wang, R. H. Friend, G. C. Bazan, and T. Q. Nguyen, Adv. Mater. **28**, 1482 (2016).

[65] S. Gélinas, O. Paré-Labrosse, C. N. Brosseau, S. Albert-Seifried, C. R. McNeill, K. R. Kirov, I. A. Howard, R. Leonelli, R. H. Friend, and C. Silva, J. Phys. Chem. C **115**, 7114 (2011).

[66] C. J. Brabec, A. Cravino, D. Meissner, N. S. Sariciftci, T. Fromherz, M. T. Rispens, L. Sanchez, and J. C. Hummelen, Advanced Functional Materials **11**, 374 (2001).

[67] R. A. Marcus, J. Chem. Phys. **24**, 966 (1956).

[68] P. F. Barbara, T. J. Meyer, and M. A. Ratner, J. Phys. Chem. **3654**, 13148 (1996).

[69] A. E. Jailaubekov, A. P. Willard, J. R. Tritsch, W.-L. Chan, N. Sai, R. Gearba, L. G. Kaake, K. J. Williams, K. Leung, P. J. Rossky, and X.-Y. Zhu, Nat. Mater. **12**, 66 (2013).

[70] R. D. Pensack and J. B. Asbury, J. Phys. Chem. Lett. **1**, 2255 (2010).

[71] X. Shen, G. Han, D. Fan, Y. Xie, and Y. Yi, J. Phys. Chem. C **119**, 11320 (2015).

[72] D. Fazzi, M. Barbatti, and W. Thiel, J. Am. Chem. Soc. **138**, 4502 (2016).

[73] G. Grancini, M. Maiuri, D. Fazzi, A. Petrozza, H.-J. Egelhaaf, D. Brida, G. Cerullo, and G. Lanzani, Nat. Mater. **12**, 29 (2012).

[74] N. R. Monahan, K. W. Williams, B. Kumar, C. Nuckolls, and X.-Y. Zhu, Phys. Rev. Lett. **114**, 247003 (2015).

[75] A. E. Jailaubekov, A. P. Willard, J. R. Tritsch, W.-L. Chan, N. Sai, R. Gearba, L. G. Kaake, K. J. Williams, K. Leung, P. J. Rossky, and X.-Y. Zhu, Nat. Mater. **12**, 66 (2012).

[76] A. A. Bakulin, A. Rao, V. G. Pavelyev, P. H. M. van Loosdrecht, M. S. Pshenichnikov, D. Niedzialek, J. Cornil, D. Beljonne, and R. H. Friend, Science **335**, 1340 (2012).

[77] F. C. Jamieson, E. B. Domingo, T. McCarthy-Ward, M. Heeney, N. Stingelin, and J. R. Durrant, Chem. Sci. **3**, 485 (2012).

[78] H. Bä and A. Kö Hler Ab, Phys. Chem. Chem. Phys. Phys. Chem. Chem. Phys **17**, 28451 (2015).

[79] D. Graves, V. Jankus, F. B. Dias, and A. Monkman, Adv. Funct. Mater. **201303389**, 2343 (2014).

[80] A. K. Pandey, Sci. Rep. **5**, 7787 (2015).

[81] P. C. Y. Chow, S. Ge, A. Rao, and R. H. Friend, J. Am. Chem. Soc. **136**, 3424 (2014).

[82] N. Sato, K. Seki, and H. Inokuchi, J. Chem. Soc. Faraday Trans. 2 **77**, 1621 (1981).

[83] S. M. Ryno, C. Risko, and J.-L. Brédas, J. Am. Chem. Soc. **136**, 6421 (2014).

[84] S. Dimitrov, B. Schroeder, C. Nielsen, H. Bronstein, Z. Fei, I. McCulloch, M. Heeney, and J. Durrant, Polymers (Basel). **8**, 14 (2016).

[85] P. E. Burrows, S. R. Forrest, E. Haskal, U. Hirose, P. Fenter, and P. Eisenberger, IEEE LEOS Annu. Meet. - Proc. **2**, p 213 (1994).

[86] R. R. Lunt, J. B. Benziger, and S. R. Forrest, Adv. Mater. **22**, 1233 (2010).

[87] S. Graham, D. Bradley, R. Friend, and C. Spangler, Synth. Met. **41**, 1277 (1991).

[88] R. sterbacka, M. Wohlgenannt, M. Shkunov, D. Chinn, and Z. V. Vardeny, J. Chem. Phys. **118**, 8905 (2003).

[89] U. Lemmer, S. Heun, R. F. Mahrt, U. Scherf, M. Hopmeier, U. Siegner, . Sbel, K. Miillen, and H. B˜issler, Chem. Phys. Lett. **240**, 373 (1995).

[90] J. L. Bredas, J. Cornil, D. Beljonne, D. A. Dos Santos, and Z. Shuai, *Acc. Chem. Res.*, **32**, 267 (1999).

[91] D. Jarzab, F. Cordella, M. Lenes, F. B. Kooistra, P. W. M. Blom, J. C. Hummelen, and M. a. Loi, J. Phys. Chem. B **113**, 16513 (2009).

[92] B. A. Collins, Z. Li, J. R. Tumbleston, E. Gann, C. R. Mcneill, and H. Ade, Adv. Energy Mater. **3**, 65 (2013).

[93] A. Mishra and P. Bäuerle, Angewandte Chemie International Edition **51**, 2020 (2012).

[94] T. Ameri, P. Khoram, J. Min, C. J. Brabec, and M. O. E. L. U. Mo, Adv. Mater. **25**, 4245 (2013).

[95] N. Koch, Phys. Status Solidi - Rapid Res. Lett. **6**, 277 (2012).

[96] Y. Lin, Y. Li, and X. Zhan, Chem. Soc. Rev. Chem. Soc. Rev **41**, 4089 (2012).

[97] C. B. Nielsen, S. Holliday, H.-Y. Chen, S. J. Cryer, and I. Mcculloch, Accounts of Chemical Research **48**, 2803 (2015).

[98] X. Liu, H. Chen, and S. Tan, Renew. Sustain. Energy Rev. **52**, 1527 (2015).

[99] B. Hemavathi, T. Ahipa, and R. K. Pai, Eur. Polym. J. **72**, 309 (2015).

[100] W. Ni, X. Wan, M. Li, Y. Wang, Y. Chen, and W. Ni, Chem. Commun. **51**, 4936 (2015).

[101] J. E. Coughlin, Z. B. Henson, G. C. Welch, and G. C. Bazan, Acc. Chem. Res. **47**, 257 (2014).

[102] Y. Huang, E. J. Kramer, A. J. Heeger, and G. C. Bazan, Chemical Reviews **114**, 7006 (2014).

[103] A. P. Kulkarni, C. J. Tonzola, A. Babel, and S. A. Jenekhe, Chemistry of Materials **16**, 4556 (2004).

[104] P. Pingel, A. Zen, R. D. Abellón, F. C. Grozema, L. D. A. Siebbeles, and D. Neher, Adv. Funct. Mater. **20**, 2286 (2010).

[105] C. H. Wang, A. K. M. M. Islam, Y. W. Yang, T. Y. Wu, J. W. Lue, C. H. Hsu, S. Sinha, and M. Mukherjee, Langmuir **29**, 3957 (2013).

[106] C. Scharsich, R. H. Lohwasser, M. Sommer, U. Asawapirom, U. Scherf, M. Thelakkat, D. Neher, and A. Kö Hler, (2011), 10.1002/polb.23022.

[107] H. Hu, K. Zhao, N. Fernandes, P. Boufflet, J. H. Bannock, L. Yu, J. C. De Mello, N. Stingelin, M. Heeney, E. P. Giannelis, and A. Amassian, J. Mater. Chem. C **3**, 7394 (2015).

[108] K. Zhao, H. U. Khan, R. Li, Y. Su, and A. Amassian, Adv. Funct. Mater. **23**, 6024 (2013).

[109] K. R. Graham, C. Cabanetos, J. P. Jahnke, M. N. Idso, A. El Labban, G. O. Ngongang Ndjawa, T. Heumueller, K. Vandewal, A. Salleo, B. F. Chmelka, A. Amassian, P. M. Beaujuge, and M. D. McGehee, J. Am. Chem. Soc. **136**, 9608 (2014).

[110] H. Yang, S. W. Lefevre, C. Y. Ryu, and Z. Bao, Appl. Phys. Lett. J. Appl. Phys **90** (2007), 10.1063/1.2734387?

[111] H. Sirringhaus, P. J. Brown, R. H. Friend, M. M. Nielsen, K. Bechgaard, B. M. W. Langeveld-Voss, A. J. H. Spiering, R. A. J. Janssen, E. W. Meijer, P. Herwig, and D. M. de Leeuw, Nature **401**, 685 (1999).

[112] J. R. Tumbleston, B. a. Collins, L. Yang, A. C. Stuart, E. Gann, W. Ma, W. You, and H. Ade, Nat. Photonics **8**, 385 (2014).

[113] L. Yang, J. Tumbleston, H. Zhou, H. Ade, and W. You, Energy Environ. Sci. **6**, 316 (2013).

[114] Y. Zhou, T. Taima, T. Miyadera, T. Yamanari, M. Kitamura, K. Nakatsu, and Y. Yoshida, Nano Lett. **12**, 4146 (2012).

[115] M. El-Nahass, H. Zeyada, M. Aziz, and N. El-Ghamaz, Opt. Mater. (Amst). **27**, 491 (2004).

[116] S. Senthilarasu, S. Velumani, R. Sathyamoorthy, G. Canizal, P. Sebastian, J. Chavez, R. Perez, a. Subbarayan, and J. Ascencio, Appl. Phys. A Mater. Sci. Process. **77**, 383 (2003).

[117] R. Collins and A. Belghachi, Mater. Lett. **8**, 349 (1989).

[118] A. Miyamoto, K. Nichogi, A. Taomoto, T. Nambu, and M. Murakami, Thin Solid Films **256**, 64 (1995).

[119] M. M. El-Nahass, F. S. Bahabri, A. A. Al Ghamdi, and S. R. Al-Harbi, Egypt. J. Sol **25** (2002).

[120] K. Vasseur, K. Broch, A. L. Ayzner, B. P. Rand, D. Cheyns, C. Frank, F. Schreiber, M. F. Toney, L. Froyen, and P. Heremans, ACS Appl. Mater. Interfaces **5**, 8505 (2013).

[121] B. P. Rand, D. Cheyns, K. Vasseur, N. C. Giebink, S. Mothy, Y. Yi, V. Coropceanu, D. Beljonne, J. Cornil, J.-L. Brédas, and J. Genoe, Adv. Funct. Mater. **22**, 2987 (2012).

[122] B. Verreet, P. Heremans, A. Stesmans, and B. P. Rand, Adv. Mater. **25**, 5504 (2013).

[123] S. Westenhoff, W. J. D. Beenken, A. Yartsev, and N. C. Greenham, J. Chem. Phys. **125**, 154903 (2006).

[124] B. Mcculloch, V. Ho, M. Hoarfrost, C. Stanley, C. Do, W. T. Heller, and R. A. Segalman, Macromolecules **46**, 1899 (2013).

[125] G. W. Heffner and D. S. Pearson ', Macromolecules **24**, 6295 (1991).

[126] P. Brown, D. Thomas, A. Köhler, J. Wilson, J.-S. Kim, C. Ramsdale, H. Sirringhaus, and R. Friend, Phys. Rev. B **67**, 1 (2003).

[127] F. C. Spano and C. Silva, Annual Review of Physical Chemistry **65**, 477 (2014).

[128] M. Böckmann, T. Schemme, D. H. de Jong, C. Denz, A. Heuer, and N. L. Doltsinis, Phys. Chem. Chem. Phys. **17**, 28616 (2015).

[129] K. Rahimi, I. Botiz, J. O. Agumba, S. Motamen, N. Stingelin, G. Reiter, G. Yu, J. Gao, J. C. Hummelen, F. Wudl, A. J. Heeger, J. H. Burroughes, D. D. C. Bradley, A. R. Brown, R. N. Marks, K. Mackay, R. H. Friend, P. L. Burns, A. B. Holmes, F. Padinger, R. S. Rittberger, N. S. Sariciftci, C. Tanase, E. J. Meijer, P. W. M. Blom, D. M. d. Leeuw, R. J. Kline, M. D. McGehee, E. N. Kadnikova, J. Liu, J. M. J. Fréchet, F. C. Grozema, L. D. A. Siebbeles, I. Botiz, S. B. Darling, K. Rahimi, I. Botiz, N. Stingelin, N. Kayunkid, M. Sommer, F. P. V. Koch, H. Nguyen, O. Coulembier, P. Dubois, M. Brinkmann, G. Reiter, G. W. Heffner, D. S. Pearson, M. Baghgar, J. Labastide, F. Bokel, I. Dujovne, A. McKenna, A. M. Barnes, E. Pentzer, T. Emrick, R. Hayward, M. D. Barnes, F. C. Spano, P. Kohn, S. Huettner, H. Komber, V. Senkovskyy, R. Tkachov, A. Kiriy, R. H. Friend, U. Steiner, W. T. S. Huck, J. Sommer, M. Sommer, J. Clark, C. Silva, R. H. Friend, F. C. Spano, C. Hellmann, F. Paquin, N. D. Treat, A. Bruno, L. X. Reynolds, S. A. Haque, P. N. Stavrinou, C. Silva, N. Stingelin, J. Clark, J.-F. Chang, F. C. Spano, R. H. Friend, C. Silva, E. T. Niles, J. D. Roehling, H. Yamagata, A. J. Wise, F. C. Spano, A. J. Moule, J. K. Grey, J. D. Roehling, I. Arslan, A. J. Moule, F. C. Spano, F. C. Spano, M. D. Barnes, and M. Baghar, RSC Adv. **4**, 11121 (2014).

[130] S. Sweetnam, K. R. Graham, G. O. Ngongang Ndjawa, T. Heumuller, J. A. Bartelt, T. M. Burke, W. Li, W. You, A. Amassian, and M. D. McGehee, J. Am. Chem. Soc. **136**, 14078 (2014).

[131] D. R. Kozub, K. Vakhshouri, L. M. Orme, C. Wang, A. Hexemer, and E. D. Gomez, Macromolecules **44**, 5722 (2011).

[132] N. D. Treat, M. A. Brady, G. Smith, M. F. Toney, E. J. Kramer, C. J. Hawker, and M. L. Chabinyc, Adv. Energy Mater. **1**, 82 (2011).

[133] D. Chen, A. Nakahara, D. Wei, D. Nordlund, and T. P. Russell, Nano Lett. **11**, 561 (2011).

[134] J. Y. Kim and D. Frisbie, J. Phys. Chem. C **112**, 17726 (2008).

[135] M. A. Ruderer, R. Meier, L. Porcar, R. Cubitt, and P. M Ller-Buschbaum, J. Phys. Chem. Lett. **3**, 683 (2012).

[136] A. J. Wise, M. R. Precit, A. M. Papp, and J. K. Grey, ACS Appl. Mater. Interfaces **3**, 3011 (2011).

[137] a. C. Mayer, M. F. Toney, S. R. Scully, J. Rivnay, C. J. Brabec, M. Scharber, M. Koppe, M. Heeney, I. McCulloch, and M. D. McGehee, Adv. Funct. Mater. **19**, 1173 (2009).

[138] M. Koppe, M. Scharber, C. Brabec, W. Duffy, M. Heeney, and I. McCulloch, Adv. Funct. Mater. **17**, 1371 (2007).

[139] N. C. Miller, E. Cho, R. Gysel, C. Risko, V. Coropceanu, C. E. Miller, S. Sweetnam, A. Sellinger, M. Heeney, I. Mcculloch, J.-l. Brédas, M. F. Toney, and M. D. Mcgehee, Advanced Energy Materials **2**, 1208 (2012).

[140] J. J. Chen, S. M. Conron, P. Erwin, M. Dimitriou, K. McAlahney, and M. E. Thompson, ACS Appl. Mater. Interfaces **7**, 662 (2015).

[141] V. S. Gevaerts, L. J. A. Koster, M. M. Wienk, and R. a. J. Janssen, ACS Appl. Mater. Interfaces **3**, 3252 (2011).

[142] Y.-T. Fu, D. a. da Silva Filho, G. Sini, A. M. Asiri, S. G. Aziz, C. Risko, and J.-L. Brédas, Adv. Funct. Mater. **24**, 3790 (2014).

[143] P.-f. B. Crystal, N. C. Miller, E. Cho, M. J. N. Junk, R. Gysel, C. Risko, D. Kim, S. Sweetnam, C. E. Miller, L. J. Richter, R. J. Kline, M. Heeney, I. Mcculloch, A. Amassian, D. Acevedo-feliz, C. Knox, M. R. Hansen, D. Dudenko, B. F. Chmelka, M. F. Toney, J.-l. Brédas, and M. D. Mcgehee, Adv. Mater. **24**, 1 (2012).

[144] S. H. Park, A. Roy, S. Beaupre, S. Cho, N. Coates, J. S. Moon, D. Moses, M. Leclerc, K. Lee, and A. J. Heeger, Nat. Photonics **3**, 297 (2009).

[145] W. C. Tsoi, S. J. Spencer, L. Yang, A. M. Ballantyne, P. G. Nicholson, A. Turnbull, A. G. Shard, C. E. Murphy, D. D. C. Bradley, J. Nelson, and J. S. Kim, Macromolecules **44**, 2944 (2011).

[146] S. Sweetnam, R. Prasanna, T. M. Burke, J. A. Bartelt, and M. D. McGehee, J. Phys. Chem. C **120**, 6427 (2016).

[147] J. a. Bartelt, Z. M. Beiley, E. T. Hoke, W. R. Mateker, J. D. Douglas, B. a. Collins, J. R. Tumbleston, K. R. Graham, A. Amassian, H. Ade, J. M. J. Fréchet, M. F. Toney, and M. D. McGehee, Adv. Energy Mater. **3**, 364 (2013).

[148] M. Linares, D. Beljonne, J. Cornil, K. Lancaster, J. L. Bredas, S. Verlaak, A. Mityashin, P. Heremans, A. Fuchs, C. Lennartz, J. Ide, R. Mereau, P. Aurel, L. Ducasse, and F. Castet, J. Phys. Chem. C **114**, 3215 (2010).

[149] S. Verlaak, D. Beljonne, D. Cheyns, C. Rolin, M. Linares, F. Castet, J. Cornil, and P. Heremans, Adv. Funct. Mater. **19**, 3809 (2009).

[150] A. Maillard and A. Rochefort, Org. Electron. physics, Mater. Appl. **15**, 2091 (2014).

[151] G. Chen, H. Sasabe, X. F. Wang, Z. Hong, and J. Kido, Synth. Met. **192**, 10 (2014).

[152] C. F. N. Marchiori and M. Koehler, J. Phys. D. Appl. Phys. **47**, 215104 (2014).

[153] S. Sweetnam, K. R. Graham, G. O. Ngongang Ndjawa, T. Heumuller, J. A. Bartelt, T. M. Burke, W. Li, W. You, A. Amassian, and M. D. McGehee, J. Am. Chem. Soc. **136**, 14078 (2014).

[154] T. W. Holcombe, J. E. Norton, J. Rivnay, C. H. Woo, L. Goris, C. Piliego, G. Gri, O. A. Sellinger, J.-l. Br, A. Salleo, and J. M. J. Fr, J. Am. Chem. Soc. **133**, 12106 (2011).

[155] J. H. Choi, K.-I. Son, T. Kim, K. Kim, K. Ohkubo, and S. Fukuzumi, J. Mater. Chem. **20**, 475 (2009).

[156] D. Veldman, I. . Pek, S. C. J. Meskers, J. Rgen Sweelssen, M. M. Koetse, S. C. Veenstra, J. M. Kroon, S. S. Van Bavel, J. Loos, and R. A. J. Janssen, J. Am. Chem. Soc. **130**, 7721 (2008).

[157] B. Bernardo, D. Cheyns, B. Verreet, R. D. Schaller, B. P. Rand, and N. C. Giebink, Nat. Commun. **5**, 3245 (2014).

[158] F. Etzold, I. A. Howard, R. Mauer, M. Meister, T. D. Kim, K. S. Lee, N. S. Baek, and F. Laquai, J. Am. Chem. Soc. **133**, 9469 (2011).

[159] K. Vandewal, W. D. Oosterbaan, S. Bertho, V. Vrindts, A. Gadisa, L. Lutsen, D. Vanderzande, and J. V. Manca, Appl. Phys. Lett. **95**, 123303 (2009).

[160] K. Vandewal, K. Tvingstedt, J. V. Manca, and O. Inganäs, IEEE J. Sel. Top. Quantum Electron. **16**, 1676 (2010).

[161] K. Vandewal, K. Tvingstedt, A. Gadisa, O. Inganäs, and J. V. Manca, Nat. Mater. **8**, 904 (2009).

[162] J. Lee, K. Vandewal, S. R. Yost, M. E. Bahlke, L. Goris, M. A. Baldo, J. V. Manca, and T. V. Voorhis, J. Am. Chem. Soc. **132**, 11878 (2010).

[163] K. Vandewal, K. Tvingstedt, A. Gadisa, O. Inganäs, and J. V. Manca, Nat. Mater. **8**, 904 (2009).

[164] M. A. Loi, S. Toffanin, M. Muccini, M. Forster, U. Scherf, and M. Scharber, Adv. Funct. Mater. **17**, 2111 (2007).

[165] M. Hallermann, S. Haneder, and E. Da Como, Appl. Phys. Lett. **93**, 053307 (2008).

[166] K. Vandewal, A. Gadisa, W. D. Oosterbaan, S. Bertho, F. Banishoeib, I. Van Severen, L. Lutsen, T. J. Cleij, D. Vanderzande, and J. V. Manca, Adv. Funct. Mater. **18**, 2064 (2008).

[167] K. Vandewal, J. Widmer, T. Heumueller, C. J. Brabec, M. D. McGehee, K. Leo, M. Riede, and A. Salleo, Adv. Mater. **26**, 3839 (2014).

[168] M. C. Scharber, D. Mühlbacher, M. Koppe, P. Denk, C. Waldauf, A. J. Heeger, and C. J. Brabec, Adv. Mater. **18**, 789 (2006).

[169] W. J. Potscavage, S. Yoo, and B. Kippelen, Appl. Phys. Lett. **93**, 193308 (2008).

[170] W. J. Potscavage, A. Sharma, and B. Kippelen, Acc. Chem. Res. **42**, 1758 (2009).

[171] S. R. Cowan, a. Roy, and a. J. Heeger, Phys. Rev. B **82**, 245207 (2010), arXiv:1010.5021 .

[172] L. J. a. Koster, V. D. Mihailetchi, R. Ramaker, and P. W. M. Blom, Appl. Phys. Lett. **86**, 123509 (2005).

[173] L. Zhang, S. S. Roy, R. J. Hamers, M. S. Arnold, and T. L. Andrew, J. Phys. Chem. C **119**, 45 (2015).

[174] C. G. Shuttle, A. Maurano, R. Hamilton, B. O'Regan, J. C. de Mello, and J. R. Durrant, Appl. Phys. Lett. **93**, 183501 (2008).

[175] K. Vandewal, Z. Ma, J. Bergqvist, Z. Tang, E. Wang, P. Henriksson, K. Tvingstedt, M. R. Andersson, F. Zhang, and O. Inganäs, Adv. Funct. Mater. **22**, 3480 (2012).

[176] G. Ren, C. W. Schlenker, E. Ahmed, S. Subramaniyan, S. Olthof, A. Kahn, D. S. Ginger, and S. A. Jenekhe, Adv. Funct. Mater. **23**, 1238 (2013).

[177] D. D. Nuzzo, G. J. A. H. Wetzelaer, R. K. M. Bouwer, V. S. Gevaerts, S. C. J. Meskers, J. C. Hummelen, P. W. M. Blom, and R. A. J. Janssen, Adv. Energy Mater. **3**, 85 (2013).

[178] H. Chen, J. Chen, W. Yin, X. Yu, M. Shao, K. Xiao, K. Hong, D. L. Pickel, W. M. Kochemba, S. Michael, K. Ii Ab, and M. Dadmun, J. Mater. Chem. A **1**, 5309 (2013).

[179] M. Seah and W. Dench, Surf. Interface Anal. **1**, 2 (1979).

[180] K. Vandewal, K. Tvingstedt, A. Gadisa, O. Inganäs, and J. V. Manca, Phys. Rev. B **81**, 125204 (2010).

[181] W. B. Jackson, N. M. Amer, A. C. Boccara, and D. Fournier, Appl. Opt. **20**, 1333 (1981).

[182] E. Buchaca-Domingo, K. Vandewal, Z. Fei, S. E. Watkins, F. H. Scholes, J. H. Bannock, J. C. De Mello, L. J. Richter, D. M. DeLongchamp, A. Amassian, M. Heeney, A. Salleo, and N. Stingelin, J. Am. Chem. Soc. **137**, 5256 (2015).

[183] P. Muller-Buschbaum, Adv. Mater. **26**, 7692 (2014).

[184] D. Hammersley, A.P.; Svensson, S.O.; Hanfland, M.; Fitch, A.N.; Hausermann, "hammersley_hpr_96-Fit_2d.pdf," (1996).

[185] J. M. Zuo and J. C. Mabon, Microsc. Microanal. **10**, 1000 (2004).

[186] D. a. da Silva Filho, V. Coropceanu, N. E. Gruhn, P. H. de Oliveira Neto, and J.-L. Brédas, Chem. Commun. (Camb). **49**, 6069 (2013).

[187] Z. Shen, H. Röhr, K. Rurack, H. Uno, M. Spieles, B. Schulz, G. Reck, and N. Ono, Chem. - A Eur. J. **10**, 4853 (2004).

[188] L. Muccioli, G. D'Avino, and C. Zannoni, Adv. Mater. **23**, 4532 (2011).

[189] B. P. Rand, D. Cheyns, K. Vasseur, N. C. Giebink, S. Mothy, Y. Yi, V. Coropceanu, D. Beljonne, J. Cornil, J.-L. Brédas, and J. Genoe, Adv. Funct. Mater. **22**, 2987 (2012).

[190] T. Sakurai, T. Ohashi, H. Kitazume, M. Kubota, T. Suemasu, and K. Akimoto, Org. Electron. **12**, 966 (2011).

[191] K. S. Yook, B. D. Chin, J. Y. Lee, B. E. Lassiter, and S. R. Forrest, Appl. Phys. Lett. **99** (2011), 10.1063/1.3621837.

[192] C. H. Cheng, J. Wang, G. T. Du, S. H. Shi, Z. J. Du, Z. Q. Fan, J. M. Bian, and M. S. Wang, Appl. Phys. Lett. **97**, 2010 (2010).

[193] T. Kadish, Karl M., K. M. Smith, and R. Guilard, " The PorphyrinHandbook PhthalocyaninesPropertiesand Materials ," (2003).

[194] P. E. Laibinis, C. D. Bain, and G. M. Whitesides, J. Phys. Chem. **95**, 7017 (1991).

[195] H. Monjushiro and I. Watanabe, Anal. Sci. **11**, 797 (1995).

[196] G. B. Sushko, A. V. Verkhovtsev, A. V. Yakubovich, S. Schramm, and A. V. Solov'Yov, J. Phys. Chem. A **118**, 6685 (2014).

[197] L. Zhu, C. W. Brian, S. F. Swallen, P. T. Straus, M. D. Ediger, and L. Yu, Phys. Rev. Lett. **106**, 1 (2011).

[198] S. Capaccioli, K. L. Ngai, M. Paluch, and D. Prevosto, Phys. Rev. E - Stat. Nonlinear, Soft Matter Phys. **86**, 051503 (2012).

[199] C. Groves, Energy Environ. Sci. **6**, 1546 (2013).

[200] R. Hoofman, M. P. DeHaas, L. D. A. Siebbeles, and J. M. Warman, Nature **392**, 54 (1998).

[201] H. R. Tseng, H. Phan, C. Luo, M. Wang, L. A. Perez, S. N. Patel, L. Ying, E. J. Kramer, T. Q. Nguyen, G. C. Bazan, and A. J. Heeger, Adv. Mater. **26**, 2993 (2014).

[202] G. J. Hedley, A. J. Ward, A. Alekseev, C. T. Howells, E. R. Martins, L. A. Serrano, G. Cooke, A. Ruseckas, and I. D. W. Samuel, Nat. Commun. **4**, 2867 (2013).

[203] D. Bartesaghi and L. J. A. Koster, Adv. Funct. Mater. **25**, 2013 (2015).

[204] T. Xiao, H. Xu, G. Grancini, J. Mai, A. Petrozza, U.-S. Jeng, Y. Wang, X. Xin, Y. Lu, N. S. Choon, H. Xiao, B. S. Ong, X. Lu, and N. Zhao, Sci. Rep. **4**, 17 (2014).

[205] M. Y. Jo, S. J. Park, T. Park, Y. S. Won, and J. H. Kim, Org. Electron. **13**, 2185 (2012).

[206] M. A. Stevens and A. C. Arango, Org. Electron. **37**, 80 (2016).

[207] D. Oeter, H.-J. Egelhaaf, C. Ziegler, D. Oelkrug, and W. Gopel, J. Chem. Phys. **101**, 6344 (1994).

[208] R. S. Becker, J. S. Demelo, a. L. Macanita, and F. Elisei, J. Phys. Chem. **100**, 18683 (1996).

[209] H. Yoshida, J. Phys. Chem. C **118**, 24377 (2014).

[210] R. Telesca, H. Bolink, S. Yunoki, G. Hadziioannou, P. Van Duijnen, J. Snijders, H. Jonkman, and G. Sawatzky, Phys. Rev. B **63**, 1 (2001).

[211] Y. Kanai and J. C. Grossman, Nano Lett. **7**, 1967 (2007).

[212] A. Opitz, M. Bronner, W. Brütting, M. Himmerlich, J. A. Schaefer, and S. Krischok, Appl. Phys. Lett. **90**, 2005 (2007).

[213] M. L. Tietze, W. Tress, S. Pfützner, C. Schünemann, L. Burtone, M. Riede, K. Leo, K. Vandewal, S. Olthof, P. Schulz, and A. Kahn, Phys. Rev. B **88**, 085119 (2013).

[214] D. L. Lichtenberger, K. W. Nebesny, C. D. Ray, D. R. Huffman, L. D. Lamb, I. The, and T. Ceo, Chem. Phys. Lett. **176**, 203 (1991).

[215] I. Salzmann, S. Duhm, G. Heimel, M. Oehzelt, R. Kniprath, R. L. Johnson, J. P. Rabe, and N. Koch, J. Am. Chem. Soc. **130**, 12870 (2008).

[216] C. Schwarz, F. Milan, T. Hahn, M. Reichenberger, S. Kümmel, and A. Köhler, Adv. Funct. Mater. **24**, 6439 (2014).

[217] Z.-L. Guan, J. B. Kim, H. Wang, C. Jaye, D. a. Fischer, Y.-L. Loo, and A. Kahn, Org. Electron. **11**, 1779 (2010).

[218] C. Deibel, T. Strobel, and V. Dyakonov, Phys. Rev. Lett. **103**, 036402 (2009).

[219] T. M. Burke and M. D. McGehee, Adv. Mater. , 1923 (2013).

[220] J. J. Chen, S. M. Conron, P. Erwin, M. Dimitriou, K. McAlahney, and M. E. Thompson, ACS Appl. Mater. Interfaces **7**, 662 (2015).

[221] G. O. Ngongang Ndjawa, K. R. Graham, R. Li, S. M. Conron, P. Erwin, K. W. Chou, G. F. Burkhard, K. Zhao, E. T. Hoke, M. E. Thompson, M. D. McGehee, and A. Amassian, Chem. Mater. **27**, 5597 (2015).

[222] S. Obata, T. Miura, and Y. Shimoi, Jpn. J. Appl. Phys. **53**, 7 (2014).

[223] P. S. Jo, D. T. Duong, J. Park, R. Sinclair, and A. Salleo, Chem. Mater. **27**, 3979 (2015).

[224] H. M. Lee, H. Moon, H. S. Kim, Y. N. Kim, S. M. Choi, S. Yoo, and S. O. Cho, Org. Electron. physics, Mater. Appl. **12**, 1446 (2011).

[225] K. Zhao, G. O. Ngongang Ndjawa, L. K. Jagadamma, A. E. Labban, H. Hu, Q. Wang, R. Li, M. Abdelsamie, P. M. Beaujuge, and A. Amassian, Nano Energy **16**, 458 (2015).

[226] G. O. Ngongang Ndjawa, K. R. Graham, R. Li, S. M. Conron, P. Erwin, K. W. Chou, G. F. Burkhard, K. Zhao, E. T. Hoke, M. E. Thompson, M. D. McGehee, and A. Amassian, Chem. Mater. **27**, 5597 (2015).

[227] L. A. Rochford, A. J. Ramadan, D. S. Keeble, M. P. Ryan, S. Heutz, and T. S. Jones, Adv. Mater. Interfaces **2**, 2 (2015).

[228] K. Tvingstedt, K. Vandewal, A. Gadisa, F. Zhang, J. Manca, and O. Inganäs, J. Am. Chem. Soc. **131**, 11819 (2009).

[229] H. M. Lee, H. Moon, H. S. Kim, Y. N. Kim, S. M. Choi, S. Yoo, and S. O. Cho, Org. Electron. physics, Mater. Appl. **12**, 1446 (2011).

[230] U. Rau, Phys. Rev. B **76**, 085303 (2007).

[231] K. R. Graham, G. O. N. Ndjawa, S. M. Conron, R. Munir, K. Vandewal, J. J. Chen, S. Sweetnam, M. E. Thompson, A. Salleo, M. D. McGehee, and A. Amassian, Adv. Energy Mater. , 1601211 (2016).

[232] W. Chen, S. Chen, H. Huang, D. C. Qi, X. Y. Gao, and A. T. S. Wee, Appl. Phys. Lett. **92**, 063308 (2008).

[233] Y. Yi, V. Coropceanu, and J.-L. Brédas, J. Am. Chem. Soc. **131**, 15777 (2009).

[234] X.-K. Chen, M. K. Ravva, H. Li, S. M. Ryno, and J.-L. Brédas, Adv. Energy Mater. **In Press**, 1601325 (2016).

[235] A. Ryasnyanskiy and I. Biaggio, Phys. Rev. B **193203**, 2 (2011).

[236] H. Mattoussi, H. Murata, C. D. Merritt, and Z. H. Kafafi, in *Proc. SPIE - Int. Soc. Opt. Eng.*, Vol. 3476, edited by Z. H. Kafafi (1998) pp. 49–60.

[237] Y. L. Lin, M. A. Fusella, O. V. Kozlov, X. Lin, A. Kahn, M. S. Pshenichnikov, and B. P. Rand, Adv. Funct. Mater. (2016), 10.1002/adfm.201601125.

[238] D. B. Sulas, K. Yao, J. J. Intemann, S. T. Williams, C. Z. Li, C. C. Chueh, J. J. Richards, Y. Xi, L. D. Pozzo, C. W. Schlenker, A. K. Y. Jen, and D. S. Ginger, Chem. Mater. **27**, 6583 (2015), arXiv:arXiv:1408.1149 .

[239] J. Zhao, Y. Li, A. Hunt, J. Zhang, H. Yao, Z. Li, J. Zhang, F. Huang, H. Ade, and H. Yan, Adv. Mater. **28**, 1868 (2016).

[240] M. Wang, H. Wang, T. Yokoyama, X. Liu, Y. Huang, Y. Zhang, T.-Q. Nguyen, S. Aramaki, and G. C. Bazan, J. Am. Chem. Soc. **136**, 12576 (2014).

8 Papers Published, Submitted and Under Preparation

8.0.0.1 Papers in submission

1. Ngongang Ndjawa, G. O.; Graham, K. R.; Dey, S.; Yu, L.; Amassian, A. Influence of Donor Crystallinity on the Charge Transfer State Energy and the Open Circuit Voltage in Organic Solar Cells. Submitted to Advanced Energy Materials.

8.0.0.2 Published papers

1. Ngongang Ndjawa, G.O; Graham, K. R.; Conron, S.C.; Erwin, P.; Li, R.; Chou, K.W.; Burkhard, G.; Zhao, K.; Hoke, E.T; Thompson, M.E; McGehee, M.D.; Amassian, A. Chem. Mater., 2015, 27 (16), 5597. Impact of Molecular Orientation and Spontaneous Interfacial Mixing on the Performance of Organic Solar Cells.

2. Graham, K. R.; Ngongang Ndjawa, G. O.; Conron, S.; Vandewal, K.: Chen, J.; Sweetnam, S.; Thompson, M.E; Salleo, A.; McGehee, M.D.; Amassian, A. The role of crystallinity and intermolecular interactions in determining energy levels and the charge-transfer state energy in organic photovoltaic materials. Advanced Energy Materials (Just accepted). Equal contribution with leading author

3. Pattanasattayavong, P.; Ngongang Ndjawa, G. O.; Zhao, K.; Chou, K. W.; Yaacobi-Gross, N. ; O'Regan, B. C. ; Amassian, A.; Anthopoulos, T. D. Chem. Commun., 2013, 49, 4154. Electric field-induced hole transport in copper (I) thiocyanate thin-films processed from solution at room temperature.
Equal contribution with leading author.

4. Zhao, K.; Ngongang Ndjawa, G. O.; Jagadamma, L. K.; El-Labban, A.; Hu, H.; Wang, Q.; Li, R.; Abdelsamie, M.; Beaujuge, P. M.; Amassian, A. Nano Energ, 16, 2015, 458. Highly efficient organic solar cells based on a robust room-temperature solution-processed copper iodide hole transporter.

5. Sweetnam, S.; Graham, K. R.; Ngongang Ndjawa, G. O.; Heumueller, T.; Bartelt, J. A.; Burke, T. M.; You, W.; Amassian, A.; McGehee, M. D. J. Am. Chem. Soc. 2014, 136, 14078. Characterization of the Polymer Energy Landscape in Polymer:Fullerene Bulk Heterojunctions with Pure and Mixed Phases.

6. Graham, K. R.; Cabanetos, C.; Jahnke, J. P.; Idso, M. N.; Laban, A. E.; Ngongang
Ndjawa, G. O; Vandewal, K.; Heumueller, T.; Salleo, A.; Chmelka, B. F.;

Amassian, A.; Beaujuge, P. M.; McGehee, M. D. J. Am. Chem. Soc. 2014, 136, 9608. Importance of the Donor:Fullerene Intermolecular Arrangement for High-Efficiency Organic Photovoltaics.

7. Graham, K. R.; Erwin, P.; Nordlund, D.; Vandewal, K.; Li, R.; Ngongang Ndjawa, G. O; Hoke, E. T.; Salleo, A.; Thompson, M. E.; McGehee, M. D.; Amassian. A. Adv. Mater. 2014, 25, 6076. Reevaluating the Role of Sterics and Electronic Coupling in Determining the Open Circuit Voltage of Organic Solar Cells.

8. Jagadamma, L. K.; Abdelsamie, M.; Labban, A. E.; Aresu, E.; Ngongang Ndjawa, G. O; Anjum, D. H. ; Amassian, A. J. Mater. Chem. A, 2014, 2, 13321. Efficient inverted bulk-heterojunction solar cells from low-temperature processing of amorphous ZnO buffer layers.

9. Pattanasattayavong, P.; Yaacobi-Gross, N.; Zhao, K.; Ngongang Ndjawa, G. O.; Li, J. ; Yan, F.; O'Regan, A. Amassian, B. C. ; Anthopoulos, T. D. Adv. Mater., 2013, 25, 1504. Hole Transporting Transistors and Circuits Based on the Transparent Inorganic Semiconductor Copper (I) Thiocyanate (CuSCN) Processed from Solution at Room Temperature.

10. Jagadamma, L. K.; Al-Senani, M.; El-Labban, A.; Gereige, I.; Ngongang Ndjawa, G. O.; Faria, J. C. D.; Kim, T.; Zhao, K.; Cruciani, F.; Anjum, D. H.; McLachlan, M. A.; Beaujuge, P. M.; Amassian, A. Adv. Energy Mater., 2015, 5, 1500204. Polymer Solar Cells with Efficiency $>$ 10% Enabled via a Facile Solution−Processed Al−Doped ZnO Electron Transporting Layer.

8.0.0.3 Conference Talks and Selected poster Presentations

1. Ngongang Ndjawa, G.O; Graham, K. R.; Mollinger, S.; Wu D.; Hanifi, D.; Prasana, R.; Rose, B.; Dey, S.; Yu, L.; Brédas, J.L.; McGehee, M.D.; Salleo, A. and Amassian, A. Influence of Donor Aggregation on The Charge Transfer State Energy and The Open Circuit Voltage in Organic Solar Cells. MRS Spring 2016, Phoenix-Arizona. April 1, 2016. Award for best Oral Presentation.

2. Ngongang Ndjawa, G.O; Graham, K. R.; Conron, S.C.; Erwin, P.; Li, R.; Chou, K.W.; Burkhard, G.; Zhao, K.; Hoke, E.T; Thompson, M.E; McGehee, M.D.; Amassian, A. Impact of Molecular Orientation and Spontaneous Interfacial Mixing on the Performance of Organic Solar Cells. SPIE, San Diego. August 17, 2014. Oral Presentation.

3. Ngongang Ndjawa, G.O; Graham, K. R.; Conron, S.C.; Erwin, P.; Li, R.; Chou, K.W.; Burkhard, G.; Zhao, K.; Hoke, E.T; Thompson, M.E; McGehee, M.D.; Amassian, A. Mixing at the Donor-Acceptor Interface: Relationship to Molecular Orientation in Organic Photovoltaics. Tenth International Conference on Electroluminescence and Optoelectronic Devices" (ICEL-10), Cologne, Germany. August 31-September 03, 2014. Oral Presentation.

4. Ngongang Ndjawa, G. O.; Graham, K. R.; Dey, S.; Yu, L.; Amassian, A. Influence of Donor Crystallinity on The Charge Transfer State Energy and The Open Circuit Voltage in Organic Solar Cells. Solar Future 2015, KAUST. November 8, 2015. Poster Presentation.

5. Ngongang Ndjawa, G.O; Graham, K. R.; Conron, S.C.; Erwin, P.; Li, R.; Chou, K.W.; Burkhard, G.; Zhao, K.; Hoke, E.T; Thompson, M.E; McGehee, M.D.; Amassian, A. Impact of Molecular Orientation and Spontaneous Interfacial Mixing on the Performance of Organic Solar Cells. CAMP annual meeting, McCullough Auditorium, Stanford University. Stanford, August 13, 2013. Poster Presentation.

6. Ngongang Ndjawa, G.O; Graham, K. R.; Conron, S.C.; Erwin, P.; Li, R.; Chou, K.W.; Burkhard, G.; Zhao, K.; Hoke, E.T; Thompson, M.E; McGehee, M.D.; Amassian, A. Impact of Molecular Orientation and Spontaneous Interfacial Mixing on the Performance of Organic Solar Cells. SPIE, San Diego. August 21, 2013. Poster Presentation.

7. Ngongang Ndjawa, G.O; Graham, K. R.; McGehee, M.D.; Amassian, A. Investigation of intermixing in organic bilayer solar cells by X-ray photoelectron spectroscopy. International Colloquium on Flexible Electronic and Photovoltaics, Nov. 3-5 2013. Thuwal, Saudi Arabia. Poster Presentation.